



Towards the Optimization of a Fin-Based Hydropower Generator

April 24, 2017

Submitted by:

Casey Broslawski
Frank DeGiacomo
Keaton Goddard
Christopher Parisi

Project Advisor:

Professor Brian Savilonis

A Major Qualifying Project submitted to the faculty of Worcester
Polytechnic Institute in fulfillment of the requirements for the degree of
Bachelor of Science

Table of Contents

Table of Contents	1
Table of Figures	4
Table of Tables	7
Abstract	8
Introduction	9
1. Background	11
1.1 Non-Renewable Energy Sources	11
1.2 Renewable Energy Sources	11
1.3 Electricity Generation	12
1.4 Economics of Power Generation	13
2. Hydropower	14
2.1 Wave Resource and Environmental Impact	15
2.2 Tidal Resource and Environmental Impact	16
2.3 River Resource and Environmental Impact	18
3. Existing Technology	21
3.1 Horizontal Axis Turbine	22
3.2 Vertical Axis Turbines	24
3.3 Oscillating Hydrofoil	25
3.4 Enclosed Tips (Venturi) Devices	27
3.5 Archimedes Screw	28
3.6 Tidal Kite	30
3.7 Impoundment Tidal Devices	31
3.8 The VIVACE Generator	33
3.9 Mounting Techniques	34
4. Biomimicry	36
4.1 Humpback Whale Pectoral Fin	37
4.2 Black Ghost Knifefish	38
4.3 Ghostbot	39
4.4 Strandbeest	42
5. Previous Work	44
6. Device and Initial Testing	46
6.1 Initial Device	46
6.2 Eccentric Cam Timing	49
6.3 Fin Design and Eccentric Cam Kinematics	50

6.4 Testing Apparatus	54
6.5 Tow Tank	54
6.6 Flow Tank	55
7. Variables and Pre-testing Analysis	57
7.1 Independent Variables	57
7.2 Fin Stiffness	58
7.3 Fin Shape	58
7.4 Computational Fluid Dynamics	59
7.5 Finite Element Analysis (FEA)	60
8. Device Testing	62
8.1 Data Collection Apparatus	62
8.2 Prony Brake Dynamometer	63
8.3 DC Motor	71
8.4 Testing Methodology	73
8.5 Calculations	74
9. Results and Analysis	77
9.1 Flow Tank Results	77
9.2 Improvements to Testing Methodology and Apparatus	78
9.3 Fin Stiffness Testing Overall Results	84
9.4 RPM vs. Torque	86
9.5 Power vs. Torque Results	89
9.6 Efficiency vs. Speed Parameter	92
9.7 Sources of Error	95
9.8 Computational Fluid Dynamics (CFD) Results	97
9.9 Finite Element Analysis (FEA) Results	108
9.9.1 Mast Deflection	108
9.9.2 Analysis of Scaled Device	119
9.9.3 Main Shaft Deflection	120
10. Conclusion and Recommendations	126
11. References	129
12. Appendix	136
Appendix A: Acrylic-hybrid Fin (T1) Plots	136
Appendix B: Acrylic-hybrid Fin (T2) Plots	140
Appendix C: 1/16" Neoprene Fin Plots	143
Appendix D: 1/8" Neoprene Fin Plots	146
Appendix E: Overall Plots	149

Appendix F: COMSOL Cross Section Views for FEA
Appendix G: COMSOL Analysis of Test Fins

151
156

Table of Figures

Figure 1: Forces of Moon and Earth on Ocean 12	17
Figure 2: Sun and Moon Effects on Tide	17
Figure 3: A rudimentary model of a horizontal axis water turbine	22
Figure 4: A digital model of Bluewater's BlueTEC	23
Figure 5: A rudimentary model of a horizontal axis water turbine	24
Figure 6: Blue Energy Canada's vertical axis water turbine	25
Figure 7: A rudimentary model of an oscillating hydrofoil	26
Figure 8: A digital model of BioPower's BioSTREAM	26
Figure 9: A rudimentary model of shrouded horizontal axis water turbine	27
Figure 10: OpenHydro's shrouded horizontal axis water turbine	28
Figure 11: A rudimentary model of a possible Archimedes screw power plant	29
Figure 12: A model of Rehart Power's Archimedes screw for power generation	30
Figure 13: A model of Minesto's Deep Green	31
Figure 14: A diagram of a traditional hydroelectric plant	32
Figure 15: A visualization of VIV	33
Figure 16: A diagram of the Vortex Hydro Energy's VIVACE converter	34
Figure 17: Humpback whale pectoral fin	38
Figure 18: Black Ghost Knifefish	39
Figure 19: Ghostbot	40
Figure 20: Central, Primary and Secondary Propulsion Vortices	42
Figure 21: Strandbeest walking on the beach	43
Figure 22: Redesigned device	48
Figure 23: Triangular shaped fin	50
Figure 24: Smooth shaped fin	51
Figure 25: Acrylic-hybrid fin	53
Figure 26: Example neoprene fin	53
Figure 27: Flow tank speed conversion chart	56
Figure 28: A diagram of a Prony brake dynamometer	63
Figure 29: Dynamometer from first MQP team	64
Figure 30: Device and data collection apparatus, front view	65
Figure 31: Device and data collection apparatus, side view	66

Figure 32: Data collection electronic equipment	66
Figure 33: Angular velocity measurement apparatus, front view	67
Figure 34: Angular velocity measurement apparatus, top view	67
Figure 35: Prony brake	69
Figure 36: Device and data collection apparatus installed in flow tank	71
Figure 37: Acrylic-hybrid Fin RPM Tests 1 and 2	80
Figure 38: Comparison of acrylic-hybrid fin RPM vs. Torque plots	81
Figure 39: Comparison of acrylic-hybrid fin Power vs. Torque plots	82
Figure 40: Comparison of acrylic-hybrid fin Filtered Total Efficiency vs. Speed Parameter plots	83
Figure 41: Comparison of peak power trendlines	84
Figure 42: Comparison of filtered efficiency data	85
Figure 43: Acrylic-hybrid Fin RPM vs. Torque plot	87
Figure 44: 1/16" Neoprene Fin RPM vs. Torque plot	88
Figure 45: 1/8" Neoprene Fin RPM vs. Torque plot	88
Figure 46: Acrylic-hybrid Fin Power vs. Torque plot	89
Figure 47: 1/16" Neoprene Fin Power vs. Torque plot	90
Figure 48: 1/8" Neoprene Fin Power vs. Torque plot	91
Figure 49: Acrylic-hybrid Fin (T2) Efficiency vs. Speed Parameter plot	93
Figure 50: 1/16 " Neoprene Fin Efficiency vs. Speed Parameter plot	93
Figure 51: 1/8" Neoprene Fin Efficiency vs. Speed Parameter plot	94
Figure 52: Standing wave in flow tank (1200 speed)	96
Figure 53: Pressure distribution along Control Fin surface	98
Figure 54: Pressure distribution along Test Fin 1 surface	98
Figure 55: Pressure distribution along Test Fin 2 surface	99
Figure 56: Pressure distribution along Test Fin 3 surface	100
Figure 57: Grid layout of fin regions and pressure distribution scale (psi)	101
Figure 58: Left side of Control Fin	102
Figure 59: Right side of Control Fin	102
Figure 60: Left side of Test Fin 2	103
Figure 61: Right side of Test Fin 2	103
Figure 62: Cantilever beam deflection	109
Figure 63: Cross sectional area of fin with pressure changes from fluid flow (Section 9)	110
Figure 64: Mast positions	110

Figure 65: Perpendicular area of fin	112
Figure 66: Parallel area of fin	113
Figure 67: Deflection per mast	115
Figure 68: Mast position and angle from center of apparatus	116
Figure 69: Mast stress with no threads	118
Figure 70: Mast stress with threads	118
Figure 71: Detailed view of stress concentration at threads	118
Figure 72: Rocker force calculation diagram	121
Figure 73: Angle diagram calculations	122
Figure 74: Eccentric load on supported beam equation diagram	123
Figure 75: Cam placement on main shaft	124
Figure 76: Main shaft deflection diagram (with and without support)	125

Table of Tables

Table 1: Recoverable wave energy resource per United States region	16
Table 2: Original Fin results and analysis based on COMSOL Simulation	104
Table 3: Test Fin 1 Results and Analysis Based on COMSOL Simulation	104
Table 4: Test Fin 2 Results and Analysis Based on COMSOL Simulation	105
Table 5: Test Fin 3 Results and Analysis Based on COMSOL Simulation	105
Table 6: Surface pressure calculation for Mast 60	111
Table 7: Mast information for calculation	110
Table 8: Mast deflection calculation in x direction	112
Table 9: Mast deflection calculation in y direction	113
Table 10: Total deflection of masts in fin	114
Table 11: Scaled fin mast deflections	119
Table 12: Force on rocker calculations	121
Table 13: x and y components of rocker forces	123
Table 14: Moments about the x and y axes	124
Table 15: Main shaft deflection	124

Abstract

This report outlines an improved means to design, manufacture, and test the fin-based hydropower generators prototyped by previous WPI MQP teams. The current MQP team introduced CFD and FEA into the design process, allowing them to study alternate fin designs and the feasibility of scaling the device. The team produced a new iteration of the cam-driven fin generator which was more reliable and amenable to testing than the original device. This new prototype was compatible with a Prony brake dynamometer, which meant the team was able to collect power and efficiency data. The team used the enhanced prototype and testing methodology to study the effect of fin stiffness, as controlled by fin thickness, on the device's overall performance. The team found that thinner, more flexible fins outperformed thicker, more rigid fins. The device's peak power and efficiency were 3 Watts and 4.5%, respectively. Scaling and further optimization of the device's design and manufacturing will further improve fin-based hydropower generators.

Introduction

Hydropower has been used for many applications ranging from turning waterwheels to hydroelectric dams and turbines. According to the International Energy Agency, 16 percent of total world electricity production comes from hydropower [1]. This percentage has slowly declined due to a rise in harvesting solar and wind energy. However, according to the Energy Information Administration, only one-third of economically feasible hydropower is currently being utilized [1], showing a potential for expansion. In addition, new oil and natural gas discoveries in the United States have made non-renewable energy resources relatively cheap compared to infrastructure, development, and maintenance of hydroelectric power generating systems.

Hydropower can be organized into three categories: wave, tidal, and river. Waves are a dependable source of energy in some regions of the world. For example, wave energy at the West Coast of the United States has the potential to generate 250 terawatt hours (TWh) per year. As 1 TWh/yr of energy will supply 93,850 homes in United States with power annually, West Coast wave power could supply roughly 23.5 million homes with electricity [2]. Tides are a very dependable source of energy; they are very predictable and do not depend on rainfall or runoff. However, the proposed methods to harness tidal energy, such as tidal dams or barrages, tidal lagoons, tidal fences, and underwater tidal turbines, are mostly hypothetical and unproven systems. The first and largest tidal barrage in La Rance Station, France, has produced 260 MW and has been in operation since 1966 [3]. However, to put this into perspective, the tidal energy from the tidal barrage in La Rance Station produces 0.00026 TW, compared to the West Coast of

the United States which could produce 100,000 times more per year with wave energy. To harness river energy, dams and reservoirs are constructed to use the flow of water to turn turbines which power generators.

Previous Worcester Polytechnic Institute (WPI) major qualifying projects (MQPs) have researched, designed, and built a fin-driven hydroelectric generator. The goal of our project is to improve the fin design and the overall efficiency of the system, and to create a working prototype that can be tested and analyzed by current and future project groups. Investment in hydroelectric energy, and renewable energy sources as a whole, must be seen as a long-term, sustainable solution; recognizing the existing potential, followed by increased implementation, will lead to less reliability on non-renewable energy.

1. Background

1.1 Non-Renewable Energy Sources

A large portion of commercially produced electricity comes from heat energy. This heat energy is captured from a number of non-renewable sources. Some commonly used sources include the burning of coal, oil, other fossil fuels, and the heat byproduct of nuclear fission in nuclear power plants. In these cases, heat is used to produce steam and rotate a steam turbine. Alternatively, the exhaust gas of combustion of natural gas is used to directly drive gas turbines [4]. Turbines account for almost all of the world's electrical power; they operate by extracting energy from fluid flow.

1.2 Renewable Energy Sources

Sources of renewable energy include biomass, geothermal, hydroelectric, solar, and wind power. Biomass energy is either created directly from burning organic material or converting material to biogas, which is then burned. Some sources of biomass include burning of wood, crops, food and yard waste, and manure [5]. Geothermal energy systems recover energy from the heat of the earth to produce electricity or heat buildings [6]. Water power is crucial to powering the modern United States; 2.4 percent of the energy America consumed in 2015 came from flowing water [7]. Furthermore, water power dominates renewable energy generation: 46 percent of America's renewable energy in 2015 (13 percent of the nation's total net energy

production) came from various sources of water power [7]. In hydropower electricity generation, water rotates a turbine which drives a generator. The two methods of achieving this are either a *storage system* where water is built up behind a dam in a river, or a *run-of-the-river system*, where water is not stored but simply flows directly through hydroelectric generators [8]. Hydropower will be discussed in more detail later. Solar energy can be captured using different methods. Firstly, photovoltaic (PV) cells, commonly referred to as solar cells, can directly convert the sun's energy into electricity. Secondly, solar power plants use the sun's energy to heat a working fluid and power a turbine/generator system [8]. Finally, wind power utilizes wind to rotate wind turbines and generate electricity.

1.3 Electricity Generation

Generators convert mechanical energy to electrical energy; there are a wide variety of generators employed in modern society and industry. Rotational electrical generators are used in applications ranging from wind turbines and industrial power plants to automobiles and lawn mowers. Almost all generators operate on the principle of electromagnetic induction, or the creation of a voltage across a conductor in conjunction with movement of or through a magnetic field. This is generally embodied as coils of wires along with magnets or electromagnets. There are two basic types of generators, alternating current (AC) generators, or alternators, and direct current generators (DC), which produce either alternating current or direct current, respectively. AC generators are built using a moving magnet and fixed coil. In DC generators the coil is

moving in a fixed magnetic field [9]. AC generators are more commonly used than DC generators.

1.4 Economics of Power Generation

A large number of factors play into the economics of power generation and vary greatly between different methods of producing electricity. For example, geographic location, power requirements, and safety can all play into the cost and feasibility of different types of energy production in a particular area. Two notable cost factors of energy production are capital cost and fuel cost; each type of power generation has its own costs in each category. Capital costs include construction of the facility or device, and any indirect costs, such as engineering or labor [10]. These tend to be lower for fossil fuel power generation and higher for renewable energy power generation. Fuel costs are the costs of materials required to operate a facility. These costs are relatively high for fossil fuel and coal burning plants, relatively low for nuclear power plants, and non-existent for most renewable energy sources [10].

2. Hydropower

All of the water on Earth is part of the hydrologic cycle. The hydrologic cycle occurs when water evaporates from the oceans, forms clouds, and falls as rain or snow. This precipitation then gathers into streams and rivers and flows back into the sea, and the cycle repeats. There is a lot of untapped potential to harness energy from water. In 2011, the worldwide capacity for hydropower was 950 gigawatts (GW) [11]. The top producers of hydropower in the world, in 2011, were China, Brazil, and the United States. China accounted for 24 percent of the worldwide capacity of hydropower, Brazil for nine percent, and the United States for eight percent [11].

In the United States, hydropower electrical generation has grown from 56 GW in 1970, to more than 78 GW in 2011 [11]. Due to the rise of natural gas power plants and other renewable technologies, such as wind and solar, the percentage of the total electricity generated by hydropower has fallen from 12 percent in 1980 to seven percent in 2012 [11]. Hydropower varies across the country; the Pacific Northwest generates more than two-thirds of its electricity from hydroelectric dams. For example, the Grand Coulee Dam on the Columbia River in Washington generates 6,750 MW [11]. There are also many smaller hydropower plants throughout the United States. In 1940, there were 3,100 plants, but by 1980, only 1,425 remained [11]. As of 2013, however, an additional 247 hydropower plants (not including pumped storage) have been restored, bringing the total number in operation to 1,672 [11]. Hydropower continues to grow in three areas: waves, tides, and rivers.

2.1 Wave Resource and Environmental Impact

Waves are a dependable energy resource; they are more predictable than wind used for land-based wind power. Winds blowing over the ocean surface generate waves. There are many parts of the world where winds blow with enough consistency and force to provide continuous waves along the shoreline. Wave energy resources are best between 30 degrees and 60 degrees latitude in both the northern and southern hemispheres [3]. The west coasts of countries and continents have greater energy potential. Some examples include the western coasts of Scotland, northern Canada, southern Africa, Australia, and the northwestern coast of the US, specifically Alaska.

Harnessing wave energy produces electricity while having minimum pollution effects on the environment. Energy from ocean waves is harnessed either directly from surface waves or from pressure fluctuations below the surface. The Electric Power Research Institute (EPRI) estimates total wave energy resource along the outer continental shelf at 2,460 TWh per year [2]. To put that into perspective, 1 TWh/yr of energy will supply 93,850 average U.S homes with power annually [2]. However, water energy cannot be harnessed everywhere for a variety of reasons, such as competing uses of the ocean (shipping, commercial fishing, naval operations) or environmental concerns in sensitive areas [2]. EPRI estimates that the total recoverable energy along the United States' shelf edge is 1,170 TWh/yr (see Table 1), which is almost one-third of the 4,000 TWh of electricity used in the United States each year.

Table 1: Recoverable wave energy resource per United States region

Region	Energy (TWh/yr)
West Coast	250
East Coast	160
Gulf Of Mexico	60
Alaska	620
Hawaii	80

2.2 Tidal Resource and Environmental Impact

Tides are a dependable source of renewable energy caused by the gravitational pull of the moon and the centrifugal force of the Earth, see Figure 1 [4]. These forces cause the water of the Earth to bulge out from its center. As the Earth rotates on its axis, the bulging oval shape of the water stays the same while the continental crust moves through the different tidal levels. The position of the moon and the sun can affect the tidal displacement as seasons progress as shown in Figure 2 [12]. Over a period of time, one can predict the changes in the tides.

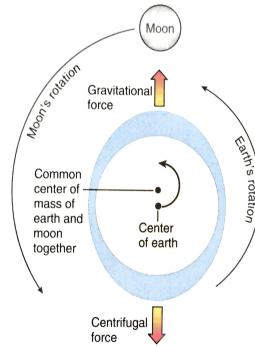


Figure 1: Forces of Moon and Earth on Ocean [12]

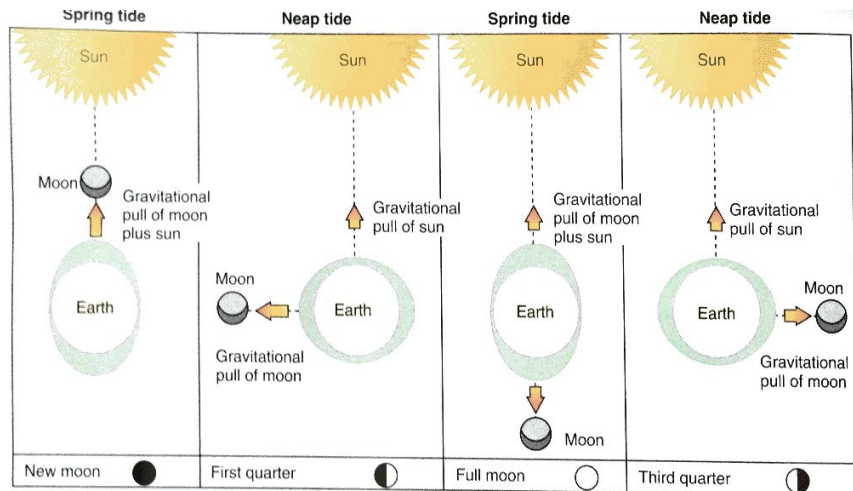


Figure 2: Sun and Moon Effects on Tide [12]

There are several ways to harness tidal energy: tidal dams or barrages, tidal lagoons, tidal fences, and underwater tidal turbines. The tidal dam or barrage uses a sliding gate to allow the tide to flow in or out across a narrow bay or estuary. This creates uneven water levels and water flows through a sluice into low-head hydro turbines. Low-head hydro turbines are turbines that generate electricity, generally with minimal environmental impact, in a river or tidal source that

is at most 66 feet deep. In order for the low-head hydro turbines to be feasible, the tides must have a difference of at least 16 feet [3]. The first and largest tidal barrage is in La Rance Station, France; it has been operating since 1966, and produces 260 MW [3]. The tidal dam and barrage have some drawbacks. They cause changes to marine environments and shoreline ecosystems, mainly fish populations. Tidal lagoons, tidal fences, and underwater tidal turbines are currently not manufactured; the most promising of these is the underwater tidal turbines. Underwater tidal turbines are placed offshore or in estuaries with strong tidal currents exceeding 5-6 mph and at 60-120 feet deep [3]. Fortunately for the environment, tidal energy generates clean electricity without producing pollutant emissions or greenhouse gases. There are some uncertain environmental impacts, but they are predicted to be small. The main concerns include impacts on marine ecosystems, fisheries, and other coastal economic activities.

2.3 River Resource and Environmental Impact

Rivers are a constant flowing part of the hydrologic cycle, which makes them ideal for a renewable energy resource. Dams and reservoirs are built to harness the energy of the river by cascading water to turn turbines, which are connected to magnets that spin in an electric coil, producing electricity. Roughly one gallon of water per second falling one hundred feet can generate one kilowatt of energy. While this produces a considerable amount of energy, dams and reservoirs cause huge impacts to the river and its ecosystem.

The purpose of a dam or reservoir is to block the flow of the river, which causes the river to back up, generating hydropower. To control the flooding of the backed up river, hilly areas

and canyons are preferred since their geography stops water from spreading. However, flooding the land has an extreme environmental impact; it destroys forests, wildlife habitats, agricultural lands, and scenic lands. The decomposing organic material trapped under the flooding water causes methane to be released, which reduces the oxygen content in the water, killing aquatic wildlife. The flooded water created by the reservoir or dam causes the water to become more stagnant than normal river water, causing higher rates of evaporation. Higher amounts of sediment and nutrients get backed up, creating excess algae and aquatic weeds, which crowd out other river animal and plant life. Manual harvesting or introducing fish that eat those aquatic plants helps control the situation. With the reservoir controlling the flow of the water, less water gets transported downstream and the reservoir creates artificial flow patterns. Some river segments can dry up, harming animal and plant life. To counter this effect, reservoirs must release a minimum amount of water at certain times during the year. The water released from the bottom of the reservoir has low circulation and remains stagnant, causing low levels of dissolved oxygen and colder temperatures. To fix this, aerating turbines can be installed to increase dissolved oxygen and have multi-level intakes to release water from multiple levels in the reservoir reducing the environmental impact of dams and reservoirs.

Dams and reservoirs impact people and aquatic life. When a dam or reservoir is built, people have to be relocated due to the creation of a flood zone. The turbine blades of the dam or reservoir can injure or kill fish and other organisms. In the Pacific Northwest and California, large dams have blocked migrations of coho, chinook, and sockeye salmon. The number of salmon journeying upstream has fallen 90 percent since four dams have been constructed on the lower part of the Snake River [11]. To fix this issue, fish ladders, barges, and intake screens

have been used, but the young fish making the journey downstream can be caught in the turbines and killed. Alternative methods to help aquatic life live unharmed by the dams and reservoirs is still being researched.

3. Existing Technology

Humans have used water power for thousands of years; ancient Greeks used it to grind wheat into flour, textile manufacturers in the Industrial Revolution used it to power their mills, and modern utility companies and governments operate large hydroelectric dams to generate and store electricity [13]. Despite this long history of growth and innovation, many sources of water power remain unutilized. Relatively few modern, utility-scale devices exist to harness the energy held in the reliable flows of rivers, tides, and ocean currents. The power available in these flows can be quantified using Equation 1 [14]. The devices discussed are designed to draw power from these flows without any surface presence (visual, physical, or acoustic) and a minimal environmental impact. They can be installed close to population centers, as well.

$$P = \frac{1}{2}\rho AV^3 \quad [Equation 1]$$

$$\rho = \textit{Fluid density}$$

$$A = \textit{Swept area}$$

$$V = \textit{Flow velocity}$$

The opportunity present in rivers, tides, and ocean currents (which from here forward will be referred to as tides for brevity), and a growing desire to further renewable energy technology has led to recent and inventive designs for devices to generate power from tides, or tidal energy

converters (TECs). The European Marine Energy Centre Ltd. (EMEC) outlines six distinct classes of TECs, as well as some techniques for affixing these structures to the seabed [15]. This section explores some recent advances in each of the EMEC's categories, as well as some other noteworthy designs. A brief overview of potential techniques for mounting TECs to the seabed has been included as well.

3.1 Horizontal Axis Turbine

Horizontal axis turbines are analogous to modern wind turbines, but instead of wind, water flows past the rotor disk. The hydrodynamic lift over the TEC's hydrofoils turns a shaft, thus converting the flow's translational kinetic energy into rotational kinetic energy [15]. This rotation can produce electricity using traditional generator technology. Like horizontal axis wind turbines, these turbines are unidirectional and thus need continuous yawing to ensure they are facing the optimal direction for power generation [15]. A model horizontal axis turbine is illustrated in Figure 3.

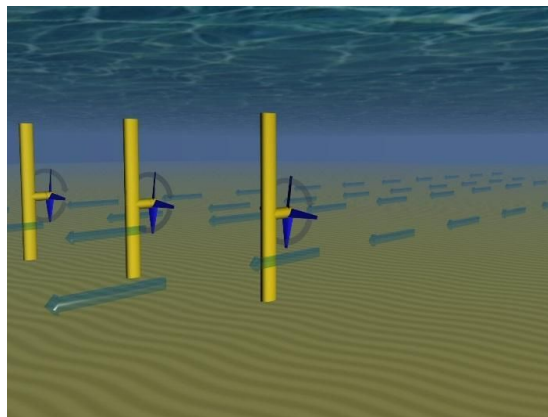


Figure 3: A rudimentary model of a horizontal axis water turbine [16]

It is interesting to compare Equation 1 for the cases of wind and water turbines. For the former, the fluid's density is low (on the order of 1 kg/m^3), the rotor's area is high (on the order of 10^3 m^2), and the fluid's velocities are moderate (on the order of 10 m/s) [14]. While water flows naturally at roughly one-third of common wind speeds, it is about 850 times as dense as air [14]. This means that wind turbines need to sweep much more area to generate the same amount of power as water turbines, which drastically increases their manufacturing and installation costs and visual impact [14]. This, taken with the inherent unreliability of the wind [14], has driven intense interest in using horizontal axis wind turbine technology to produce analogous water turbines.

One horizontal axis water turbine that has been successfully connected to an electric grid is Bluewater's BlueTEC [17]. This device, which was deployed off of the Dutch island of Texel in 2016, contains much of its controls and electrical technology in an above-water buoy [17]. The turbine itself sits below this floating structure, which is kept in place with flexible mooring cables as shown in Figure 4. By floating the device (as opposed to fixing it to the bottom of the seabed), designers made the BlueTEC easier to install and maintain than other TECs and ensured it is minimally affected by boundary layer effects in tidal flows [17].



Figure 4: A digital model of Bluewater's BlueTEC [17]

3.2 Vertical Axis Turbines

Similar to horizontal axis turbines, vertical axis turbines require a fluid flow along their blades to generate hydrodynamic lift and spin a shaft. However, the axis of rotation for these turbines is vertical, perpendicular to the direction of the flow [15]. This allows these devices to potentially generate power from fluid flowing in any direction; such a configuration is illustrated in Figure 5.

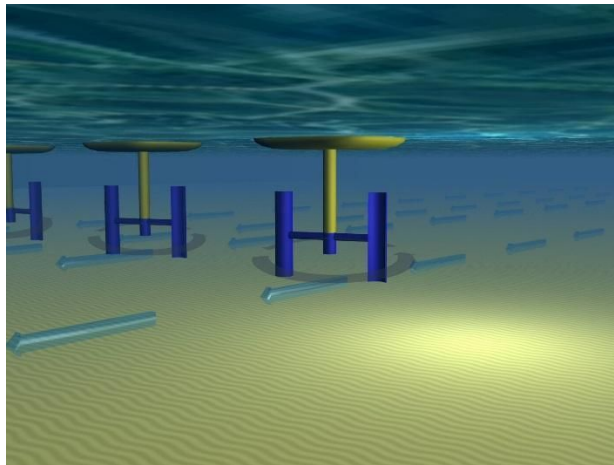


Figure 5: A rudimentary model of a horizontal axis water turbine [16]

Blue Energy Canada, Inc. (BEC) is heavily researching shrouded vertical axis TECs. Their patented design, shown in Figure 6, can either be mounted to the seafloor or suspended from a floating buoy [18]. The company is working on stacking their modular turbines like building blocks so as to create a large submerged structure they call a tidal bridge; by combining the efforts of numerous stacks of turbines across an entire tidal channel, designers believe grid level power outputs can be achieved [18]. Note that BEC's engineers opted for a shrouded

vertical axis water turbine, which removes the TEC's omnidirectional functionality (without the assistance of a yaw controller) but provides other benefits, some of which are discussed later in this section.

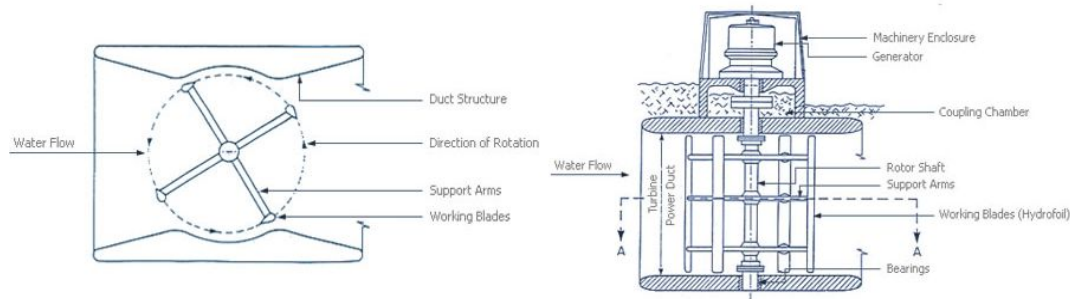


Figure 6: Blue Energy Canada's vertical axis water turbine [18]

3.3 Oscillating Hydrofoil

Oscillating hydrofoils rely on a single, symmetric hydrofoil to move a lever arm, which then runs a generator. The flow of water over the hydrofoil creates hydrodynamic lift, which causes the hydrofoil to rise or fall depending on its orientation [15]. Oscillating hydrofoils usually require some sort of actuator to re-orient the hydrofoil at the end of its upstroke or downstroke, which reduces the system's net power output [15]. Depending on the orientation of the device, the concept is analogous to a whale's or fish's tail. A simple oscillating hydrofoil device, perhaps inspired by the former, is shown in Figure 7.

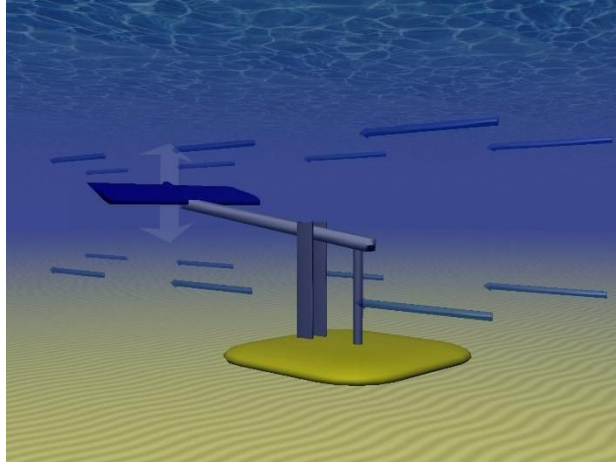


Figure 7: A rudimentary model of an oscillating hydrofoil [16]

The Australian company BioPower Systems is currently developing a 250 kW oscillating hydrofoil prototype which was inspired by the side-to-side motion of a fish's tail (see Figure 8) [19]. The bioSTREAM™ is designed for flows that have a peak speed of 2.5 m/s and uses an onboard computer to keep the hydrofoil at an optimal angle of attack [19]. The company is performing a site assessment of a location off of Flinders Island, Tasmania, Australia, for a potential deployment of the bioSTREAM [19].



Figure 8: An image of BioPower's BioSTREAM [19]

3.4 Enclosed Tips (Venturi) Devices

The Venturi effect is a phenomenon that occurs in pipe flows. When the flow's area is reduced, mass conservation demands that its velocity rises by the inverse amount [20]. As the velocity increases, the fluid's pressure drops, in accordance with the famous Bernoulli equation. The Venturi effect is used widely in industry, especially in pumps [20]. However, the phenomenon can and has been extended to TECs by simply introducing a shroud around a turbine as is shown in Figure 9. Decreasing the flow's area will increase its velocity, which, when taken with Equation 1, means the power extracted from the flow will increase greatly. The mass flow rate, which is $\rho \cdot A \cdot V$, is held constant as mass is always conserved; therefore in Equation 1 the velocity is effectively squared, not cubed as one of the velocity terms is “absorbed” into the mass flow rate [15]. Alternatively, the Venturi effect could be used to create an above-water pressure differential to power an air turbine [15].

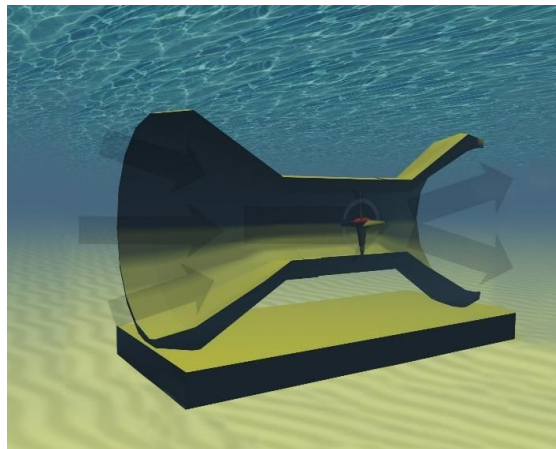


Figure 9: A rudimentary model of a shrouded horizontal axis water turbine [16]

In addition to Blue Energy Canada, another company which takes advantage of the Venturi effect is OpenHydro, a subsidiary of Direction des Constructions Navales Services. OpenHydro produces horizontal axis hydro turbines with shrouds and has won contracts to create several utility scale tidal power plants [21]. It is worth noting that OpenHydro's design does not have a hub or shaft in the center of the device; instead, there is only an open channel (see Figure 10). This greatly reduces the complexity of OpenHydro's TECs and makes them cheaper, more robust, and safer for the environment than other horizontal axis water turbines [21].

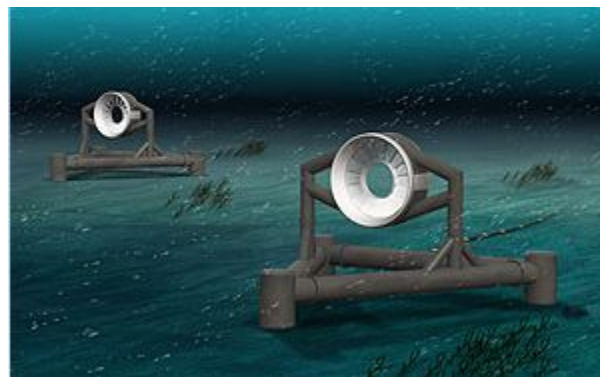


Figure 10: OpenHydro's shrouded horizontal axis water turbine [21]

3.5 Archimedes Screw

The EMEC defines an Archimedes screw as “a helical surface surrounding a central cylindrical shaft” [15]. For thousands of years these devices have been used as simple pumps; by manually turning the screw's shaft users could pump water or grain up a channel, “carrying” the fluid in the device's threads [22]. However, Archimedes screws are now being used for

power generation in rivers with dams. Water flowing down a channel along the device's threads can turn the shaft, completely reversing Archimedes' original intent [15]. It may be possible to use a tide or river, without a dam or channel, to turn the shaft by orienting the screw at a certain angle with respect to the flow; this notion is illustrated in Figure 11 [15].

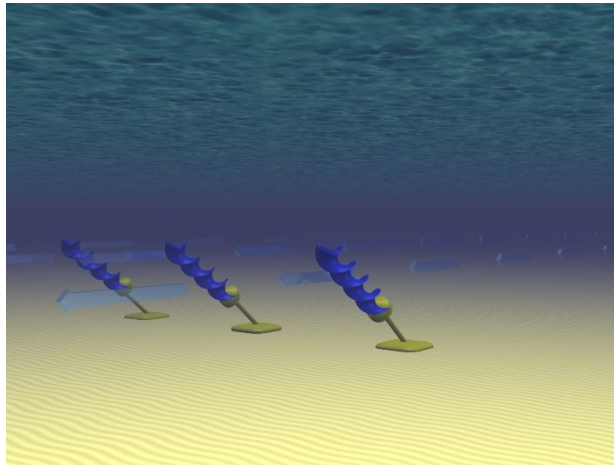


Figure 11: A rudimentary model of a possible Archimedes screw power plant [16]

While no Archimedes screw TEC companies exist yet, the principle of using Archimedes screws for power generation is a well established idea. Rehart Power is one of many companies which sells Archimedes screws for electricity generation in rivers with dams. Rehart Power's generators, like all Archimedes screws, are simple, low-speed devices that operate with low volumetric flow rates. These traits mean that these generators are relatively cheap and have small environmental impacts at sites where they have been deployed, compared to traditional hydroelectric generators at dams [23]. Furthermore, Archimedes screws are highly scalable, both in size and volumetric flow capability. However, while increasing length or volumetric

flow rate may increase an Archimedes screw's power output, this technology inherently cannot produce as much power as other, more grid-level renewable technologies, such as modern wind turbines. Rehart Power, for example, has completed projects ranging from 21 to 250 kW [23]. A model of Rehart Power's hydropower screw is shown in Figure 12.

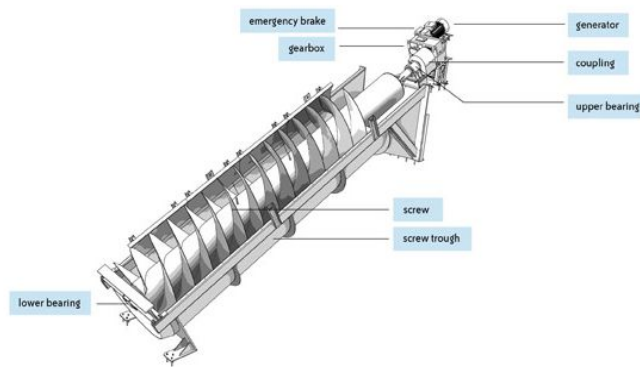


Figure 12: A model of Rehart Power's Archimedes screw for power generation [23]

3.6 Tidal Kite

Tidal kites mount shrouded horizontal axis turbines on underwater kites, which are “flown” in a figure-eight pattern [15]. Note that, similar to oscillating hydrofoils, these kites can simply fly up and down to power a lever arm. For the mounted turbine design, as the low-speed water current propels the kite, water flows through the turbine at an increased velocity; this means these TECs can generate a lot of power from even low-speed flows [15]. Furthermore, underwater kites are easy to install and have a minimal impact on the environment. However, these TECs do require a controller to ensure an optimal figure-eight flight path is established.

Minesto's Deep Green is an existing hydro kite prototype. It is designed to operate in the 1.2 to 2.5 m/s flows and at depths between 60 and 120 meters [24]. Minesto estimates that a single Deep Green kite could supply 3.3 kW of power, but the devices could be deployed in a large array [24]. Deep Green's components are shown in Figure 13.

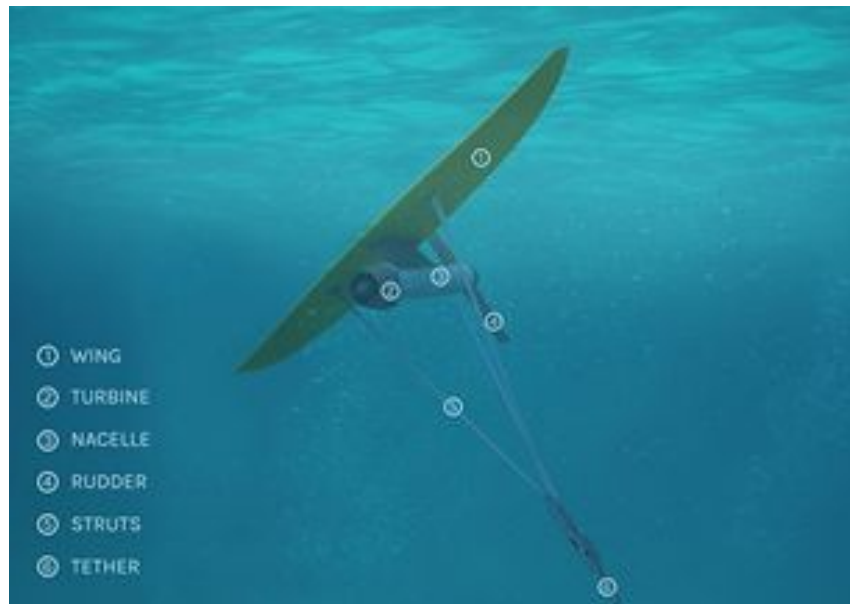


Figure 13: A model of Minesto's Deep Green [24])

3.7 Impoundment Tidal Devices

Modern hydroelectric dams work by storing water at a high elevation, then running it down a narrow channel past a turbine [25]. This process is shown in Figure 14. The underlying challenge of this principle is getting water to a high elevation so it has a high potential energy. Ordinarily this problem is solved by building a dam (a practice employed for thousands of

years), or pumping water into an elevated reservoir during off-peak hours of electrical demand when prices are low, then running it down the dam at peak hours when prices are high [25].

While both methods work and make economic sense, it would be logical to let tides move the water naturally. For instance, as a tide comes in water could rush into a basin past a turbine, generating power. Then, as the tide goes out that stored water could be released, flowing past a different turbine and generating more power [14]. This is the underlying principle of impoundment tidal devices such as France's La Rance Tidal Power Station. This site, built in 1967, has an average tidal range of 8.5 meters and a mean output of approximately 65 MW [26]. Other potential sites include the Bay of Fundy, which could support 2 GW of reliable electricity generation with its peak 15 m tides [27]; so far, competition from fossil fuels, costs, and a lack of cooperation between the United States' and Canadian governments have stalled efforts to fully harness the Bay of Fundy's tides for power generation [27].

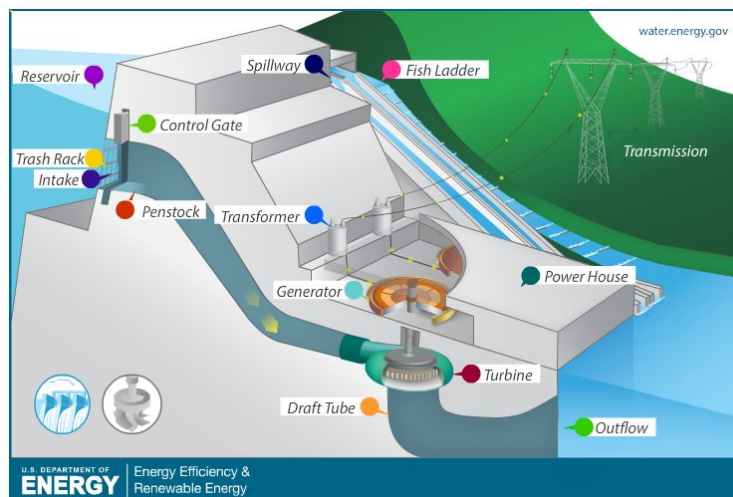


Figure 14: A diagram of a traditional hydroelectric plant [25]

3.8 The VIVACE Generator

A well-explored fluid phenomenon is vortex induced vibration (VIV), where a low-speed flow over a blunt body causes the body to oscillate [28]. VIV occurs because the flow forms and sheds vortices in the low pressure region behind the body, alternating which half of the body establishes the vortex. The vortex represents a relatively high pressure region, so if it forms on the top half of the body, the body will move down, and vice versa [28]. This is illustrated in Figure 15.

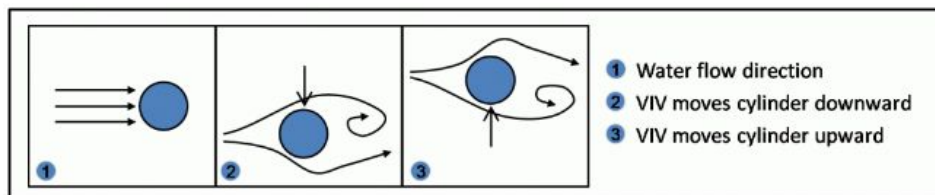


Figure 15: A visualization of VIV [28]

Ordinarily, VIV is a dangerous phenomenon for man made structures, causing the infamous collapse of the Tacoma Narrows Bridge in 1940 [28]. However, a company called Vortex Hydro Energy has found a way to harness this motion so it can produce electrical power. As water flowing with a velocity anywhere from 1 to 2 m/s (most rivers and ocean currents in the United States flow below 1.5 m/s) moves across a cylinder in Vortex Hydro Energy's patented VIVACE converter, it moves the cylinder up and down [28]. A magnetic induction generator in the cylinder's supports converts this oscillating linear motion into electrical power, as shown in

Figure 16; theoretically many VIVACE converters could be placed in the same location to collectively generate utility-level power [28]. The VIVACE converter is currently being tested and optimized in real environments, including the St. Clair River [28].

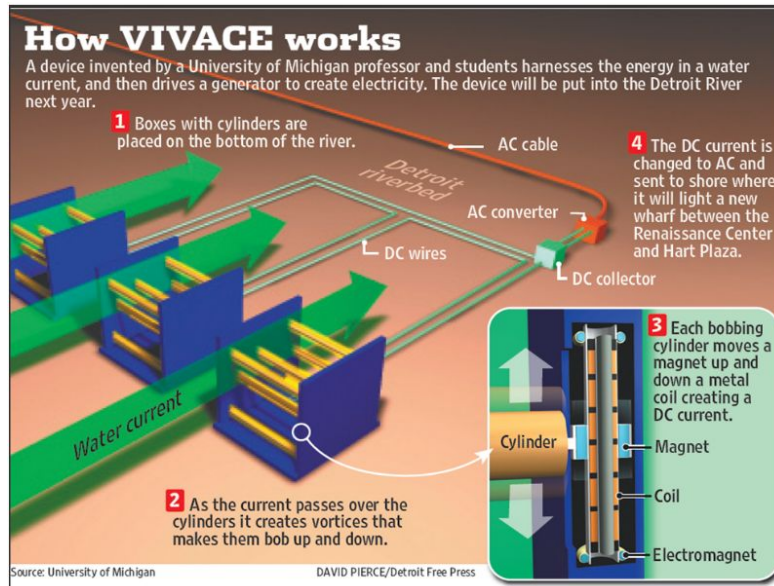


Figure 16: A diagram of the Vortex Hydro Energy’s VIVACE converter [29]

3.9 Mounting Techniques

The EMEC outlines several common techniques for affixing TECs to the seafloor; many methods exist, and the technique used depends greatly on the TEC. An overview of common practices is included here:

- Seabed Mounted/Gravity Base [15]: The sheer weight of the structure holds it in place.
- Pile Mounted [15]: The structure rests on large piles driven deep into the seabed. In some orientations, the structure could be raised along the piles so it can be accessed

above water. It is worth noting that this is the most common technique to install offshore wind turbines.

- Hydrofoil Inducing Downforce [15]: As water flows past a hydrofoil, it produces a downward force sufficient to keep the structure in place. Note that the hydrodynamics of this design are no different from hydrofoils that generate lift; here the hydrofoils are simply inverted.
- Floating [15]: Flexible moorings allow devices to move relatively freely in all directions, rigid moorings constrain devices to one position, and these floating structures can rise and fall with the sea level.

4. Biomimicry

A major issue with the current energy harvesting technology is the inability to exhibit competitive efficiencies. Currently, many rotating blade wind turbines face difficulty approaching the Betz limit of turbine efficiency. Rotational energy harnessing generators are common in applications where the power source flows normal to the apparatus. In recent years continual development of oscillating energy harvesting technology, particularly focusing on the oscillatory motion of ocean waves, has provided another approach to increasing energy harnessing efficiencies to a competitive level.

In an attempt to successfully move past the challenges faced today, engineers are looking to nature as a source of inspiration and innovation. Marine animals require propulsion through the water for survival, whether this be to search for food, escape danger, or acquire oxygen. Through evolution, all sea animals have developed some form of propulsion with which to move through the water suitable to the habitat and behavioral needs. Using energy, the animal moves in such a way that the body creates a force acting on the water and an equal and opposite reaction causes propulsion through the water.

While there are a handful of different propulsion methods depending on the type of aquatic animal, the use of an oscillating fin is most commonly seen in amphibians, fish, reptiles, and mammals. Comparing nature's method of propulsion to the rotary blade propeller of today's engine powered marine vehicles illustrates two vastly different forms of generating propulsion. Knowing the complexity of the components behind a completely rotational propulsion method and the corresponding rotary engine, it is not surprising why nature has not developed this type

of propulsion through years of evolution. In the unexplored realm of oscillatory fins, the question remains if nature has developed a more efficient form of propulsion. However, by inverting the concept of propulsion, energy generation inspired by existent biomechanics gives light to numerous possibilities for increased efficiency.

4.1 Humpback Whale Pectoral Fin

The rate of new developments in current water energy harvesting technology that significantly increase the generation efficiency is limited by the mechanical intent of many energy harnessing apparatuses. The concept of utilizing a natural phenomenon intended for propulsion and adapting its use for energy harvesting has already been proven capable in the wind energy harvesting industry. Inspired by the pectoral fin design of humpback whales, redesigned wind turbine blades have increased energy harvesting efficiencies and produce more power than ever before. The humpback whale, weighing up to 80,000 pounds, demonstrates remarkable agility and control while hunting krill. Analysis of the whale's movement pattern concludes that the maneuverability of the whale can be attributed to the nonuniform bumps along the leading edge of the pectoral fin as seen in Figure 17 [30]. The turbulent flow created as a result of water flowing over a relatively smooth surface creates unnecessary drag and a loss of control for any type of aquatic animal. However, the unique tubercles on the humpback whale's fin increase the hydrodynamic quality allowing for more control in the water. Aerodynamic testing of the humpback whale fin shape compared to a traditional fin with a smooth leading edge resulted in an increase in lift capability, decrease in drag, and an increase in the angle of

attack before a stall condition. Utilizing the whale fin's irregular design, wind energy harvesting companies, such as Whale Power, are implementing tubercles on turbine blades to obtain as much as 8% improvement in lift and as high as 32% drag reduction.



Figure 17: Humpback whale pectoral fin [31]

4.2 Black Ghost Knifefish

In hopes of developing a hydroelectric generator that is more efficient and pushes the boundary of energy extraction, engineers look to reverse engineer oscillatory waveforms found in nature to improve the extraction of power from a system that is known for being the most common propulsion method of marine life. The black ghost knifefish, Figure 18, is a tropical fish known for an oscillatory fin along the underside of the body, which is used to propel the fish through the water. The fin is capable of moving the fish laterally in all directions along its horizontal axes and also in all directions along its vertical axis, with each transition occurring nearly instantaneously [32]. This unique biological fin design is capable of directing forces in all

directions. The ribbon fin allows the fish to create a force along a swept volume as compared to a swept area, allowing it to generate more force proportional to the size of the fish than other marine animals. Analysis of the black ghost knifefish's movement through water provides insight as to the interaction of forces between the water and the fin. Computational fluid dynamics (CFD) is used to model the ghost fish ribbon fin revealing the mystery behind the black ghost knifefish itself. As the ribbon fin oscillates, primary and secondary shedding vortices are created along with a centralized vortex ring, all of which propel the fish through the water in any direction [33].



Figure 18: Black Ghost Knifefish [34]

4.3 Ghostbot

The capability of the ribbon fin has inspired researchers at Northwestern University to create a robotic fish with the same propulsion system as the ghost fish. Their creation of the Ghostbot, Figure 19, not only proves that the concept is replicable by man, but provides the ability to further understand the kinematics through additional controlled testing and analysis of

the ribbon fin. In reverse, the concept of extracting energy from a swept volume can be implemented using a similar biologically inspired ribbon fin design. The ribbon fin concept provides another path into experimental technological advancement that may increase electrical generating efficiency beyond previous expected capabilities.



Figure 19: Ghostbot [35]

Fluid dynamic modeling of the Ghostbot fin provides valuable information for optimizing the fin design and movement pattern. Most analysis of the design was concentrated on the relationship between the fin wave pattern and the resulting surge force. Surge force, determined through the use of CFD analysis, defines the power law relation between the fin dimensions and specific wavelength.

$$F_{surge} = C_1 \rho f^2 L_{fin}^4 \Theta_{max}^{3.5} \left(\frac{h_{fin}}{L_{fin}}\right)^{3.9} \Phi\left(\frac{\lambda}{L_{fin}}\right) \quad [Equation 2] [33]$$

$C_1 = \text{Experimental constant}$

$\rho = \text{Density of water}$

$f = \text{Frequency of the wave along the fin length}$

$L = \text{Fin length}$

$\Theta_{max} = \text{Max angle of deflection from center plane}$

$h = \text{Height of fin}$

$\Phi\left(\frac{\lambda}{L_{fin}}\right) = \text{Specific wavelength approximated by;}$

$$\Phi\left(\frac{\lambda}{L_{fin}}\right) = \frac{1 - \exp\left[-\left(\frac{\lambda}{L_{fin}}\right)^2\right]}{\frac{\lambda}{L_{fin}}} \quad [Equation 3] [33]$$

The results of the CFD reveal the secret to the propulsive power of the Ghostbot and, similarly, the knifefish. The undulating motion of the fin creates numerous primary and secondary vortices, which in turn create the pressure differential forming the surge force. Modeling the flow of water around the movement of the fin is key to understanding the fin and water interaction, providing the ability to optimize the fin for performance. Figure 20 illustrates the complex reality of the interaction between the fin and the fluid. The fluid velocity (u) in the x-direction is normalized relative to the wave speed of 10 cm/s (V) showing the relative speed of the fluid in the x direction compared to the constant wave speed of the fin. Both the top view (A) and the front end view (B) in Figure 20 show the variation in fluid velocity relative to the fin

wave speed, providing the means to propel the ghostbot forward. In reverse, energy harvesting requires understanding of the interaction between the water and fin when the fluid is providing the driving force to cause movement of the fin. Through modeling of these force interactions, the fin can be optimized to harness energy with competitive efficiencies.

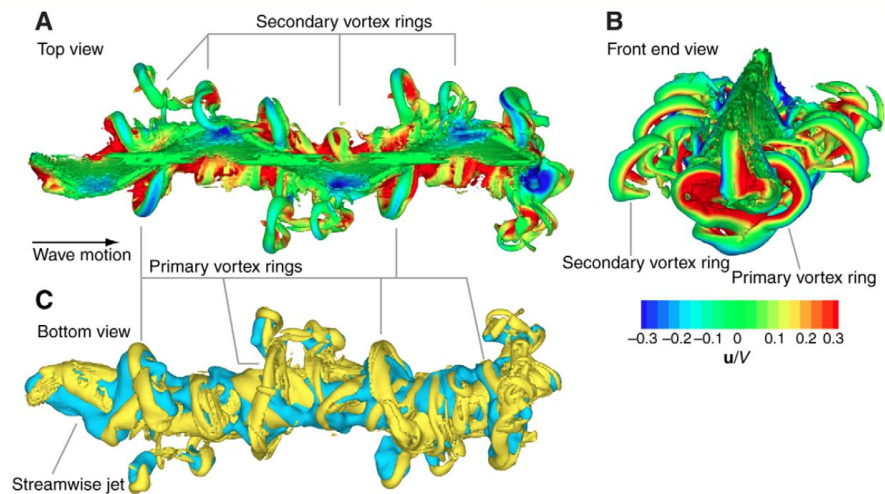


Figure 20: Central, Primary, and Secondary Propulsion Vortices [33]

4.4 Strandbeest

Biomimicry for the purpose of oscillatory energy harvesting has already been proven by kinematic artist Theo Jansen and his creation of the “Strandbeest” (Figure 21). Using a ribbon like fin, the Strandbeest harnesses energy from the wind converting it to mechanical energy propelling it across the beach. Reproduction of naturally occurring phenomena to solve modern challenges is the key to biomimicry. Inspired by the knifefish ribbon fin and proven effective by

the Ghostbot, it is believed that the same ribbon fin structure can be used for the reverse purpose of extracting energy from the fluid.



Figure 21: Strandbeest walking on the beach [36]

5. Previous Work

This project is a continuation of two years of previous work in harnessing tidal stream power, “*Design of a Novel Concept for Harnessing Tidal Stream Power*” [38] and “*Design of a Novel Concept for Harnessing Tidal Stream Power, A Continuation*” [39]. Past work involved the design, manufacturing, and testing of a water energy harvesting device. The concept of a ribbon fin apparatus was inspired by the black ghost knifefish, known for its maneuverability and propulsion capability. Understanding the restrictions imposed by the Betz limit, the team focused on designing an apparatus that would extract energy from a swept volume versus a swept area with a sinusoidal ribbon fin design. Utilizing a camshaft power transmission mechanism, the oscillatory motion of the ribbon fin extracts energy from the moving fluid, which is transferred through the camshaft to a drive shaft, ultimately connected to a dynamometer. The first group designed and tested four different fin configurations, varying the size and material composition of the fin. Testing of the ribbon fin apparatus was conducted in both the Higgins Laboratory flow tank and the Donahue Rowing Center tank. Analysis of data collected during testing determined that the ribbon fin apparatus was capable of generating 14 watts of power at a flow speed of 1.23 m/s with an average efficiency of 41 percent using a hybrid neoprene and acrylic fin material. A majority of the data collected was deemed inconclusive due to excessive vibration of the apparatus during testing.

This work was continued by another group who used the same ribbon fin concepts, but redesigned the power transmitting mechanism, as well as the hybrid fin. The second group believed that the acrylic sections within the neoprene fin caused the fin to oppose the forces of

the water [39]. Utilizing a more traditional crankshaft and more flexible fin design, the second group was unable to achieve an equal or greater power generation output [39]. The current team's work will focus on reevaluating the contrasting designs of both groups and the inefficiencies limiting the output potential of the ribbon fin apparatus.

6. Device and Initial Testing

6.1 Initial Device

The fin generator that the team began with was a product of the labor of a second year of work, work done by a “Team-2” which improved upon the original designs of “Team-1”, the theorists and pioneers. From a general standpoint, the fin generator consisted of a frame, crankshaft, rocker shaft, crankshaft and rocker supports, rockers, and a fin. The frame, upon which all components were assembled, was constructed using 1 inch 80/20 T-slot aluminum rails. These housed supports, cut out of 1/4” acrylic sheet, for crankshaft and rocker shaft bearings. The crankshaft assembly was a medley of acrylic and 3D printed parts. The shaft itself was made of acrylic blocks and rods which were bolted together. The connecting rods were 3D printed. The rocker shaft was a 1/4”-20 threaded rod which supported 3D printed plastic rockers held in place by nylon insert lock nuts that were threaded onto the rod. These rockers were epoxied to seven brass shafts that acted as masts. The fin was made entirely out of 1/8” neoprene which was sewn onto each individual mast.

Theoretically, this fin generator worked, but there were a few issues with it when it was bequeathed to the team. The fin generator was redesigned with structural integrity, ease of manufacture and assembly, and flawless operation in mind. The issues that needed to be addressed were as follows:

- broken crankshaft
- rotational binding during operation

- shaft flexion during operation
- rockers prone to failure
- loose parts
- incorrect timing between successive masts

The first and most substantial design change was the adaptation of an eccentric cam system, as opposed to the original crankshaft. Initial testing was done with a pre-existing 1/4" hexagonal shaft (main shaft) with seven eccentric cams, one for each rocker and mast, which proved to flex severely during operation.

After initial testing was conducted and the device was proven to work, a number of changes to the design were made. In order to achieve the design goals, the main shaft, rocker shaft, supports, eccentric cams, eccentric cam mounts, main shaft bearings, and rockers were all either redesigned or replaced, and the number of masts was reduced. First and foremost, the main shaft and rocker support shaft were changed to 1/2" round steel rods. This aimed to improve overall device rigidity and eliminate shaft flexion during operation. The end supports were redesigned to be manufactured solely from 1/2" acrylic sheets, and the center supports were merged into one support, manufactured from a 1/2" aluminum plate. The center support was designed to bolt directly to the frame rails to prevent movement and also included a set screw to secure the rocker support shaft. The eccentric cams were redesigned to use commercially manufactured ball bearings to greatly improve eccentric cam strength and substantially reduce friction within the system. New aluminum cam mounts were required to accept the larger 1/2" shaft. These follow the same basic design as the original cam mounts and use 1/4"-20 set screws to ease adjustment of the eccentric cam timing. Three sealed pillow bearings replaced the open

bearings and bolted directly to their respective support. This prevents water from entering the bearings, reduces friction, and ensures the bearings will not fall out or move. The rockers were designed to utilize a hybrid construction of 1/4" acrylic plates and aluminum cores. These aluminum cores are threaded to accept the brass masts, facilitating removal of the masts and easier removal of fins. The rockers bolt together to improve strength. They also include needle bearings press fit into the aluminum core of the rocker which reduces friction between the rocker and rocker support shaft as the rocker pivots.

These changes were implemented successfully and fulfilled the design goals. The device is structurally sound and operates dependably, and parts are easier to manufacture and assemble. Ultimately, this allowed for increased flow speeds during testing and reduced noise and errors in collected data. CAD files for the full design of the device have been submitted alongside the electronic version of this report. The completed redesigned device can be seen in Figure 22 below.

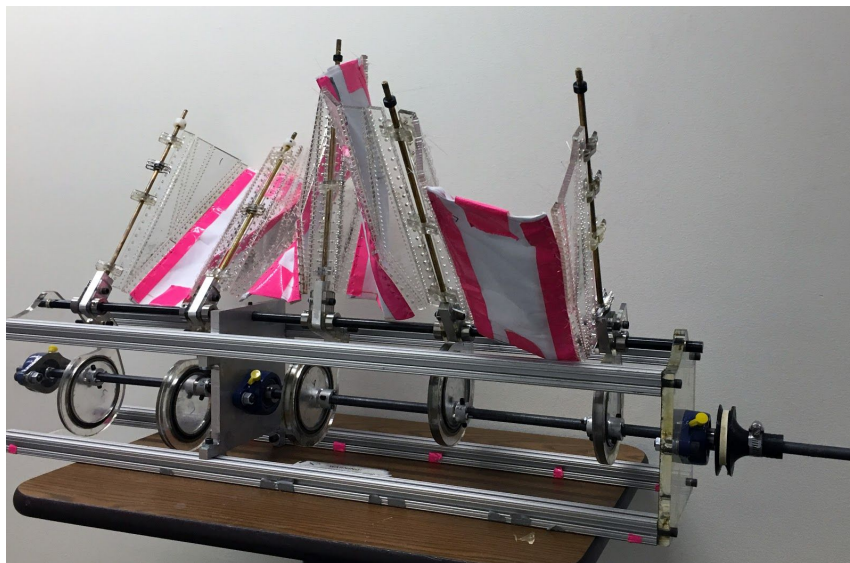


Figure 22: Redesigned device

6.2 Eccentric Cam Timing

Eventually, an issue of timing came to light. It is important to understand that while the kinematics of one eccentric cam and rocker may function successfully, combining five eccentric cam and rocker subassemblies in succession required careful consideration of the timing between cams. As evident in a car engine, the crankshaft restricts the movement of each piston to only one degree of freedom. As the crankshaft rotates, each piston must follow with the correct timing. If the rotation of the crankshaft causes the piston to rise while the forces of combustion counteract that motion, the engine will bind, ceasing rotation of all components. The same timing principles apply to the fin generator and must be accounted for during assembly. If one rocker and eccentric cam subassembly is not constrained to the main shaft with the correct angular displacement relative to the next subassembly, the apparatus will bind. Forces acting on the fin created by the flowing water surrounding the apparatus attempt to rotate each mast about the rocker shaft. Subsequently, the forces applied by the rocker arm on the eccentric cam will attempt to rotate the eccentric cam and the affixed main shaft. Without correct timing, forces exerted by one rocker/eccentric cam subassembly will attempt to rotate the main shaft in a way that counteracts the rotation of a subsequent rocker/eccentric cam subassembly causing the apparatus to bind and the shaft to deflect. In order for the device to operate properly, the team assembled the apparatus such that each rocker/eccentric cam subassembly is angularly offset by 60° relative to the next rocker/eccentric cam subassembly.

6.3 Fin Design and Eccentric Cam Kinematics

Due to construction constraints and the desire to reuse components from previous MQP teams, the apparatus was restricted to a five-mast system. Wavelength and wave form were the two parameters considered when designing the fin shape. The team believed that a longer sine wave would result in higher efficiency, but the limitation of five masts created a direct correlation between wavelength and wave form. The team first considered a wavelength of one full sine wave with masts at the 0° , 90° , 180° , 270° , and 360° positions. However, this resulted in a triangular fin shape as seen in Figure 23 below. The team believed this would cause the fin to deflect water rather than “catch” it, thereby reducing the energy that could be transferred to the device’s shaft. The team decided to reduce the wavelength to $2/3^{\text{rd}}$ sine wave allowing for placement of the masts at the 0° , 60° , 120° , 180° , and 240° positions, ensuring a smoother fin shape which the team believed would ultimately result in a higher fin efficiency (Figure 24).

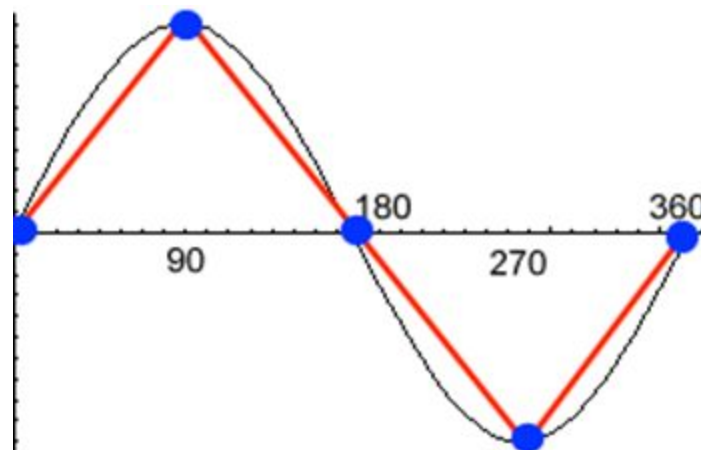


Figure 23: Triangular shaped fin

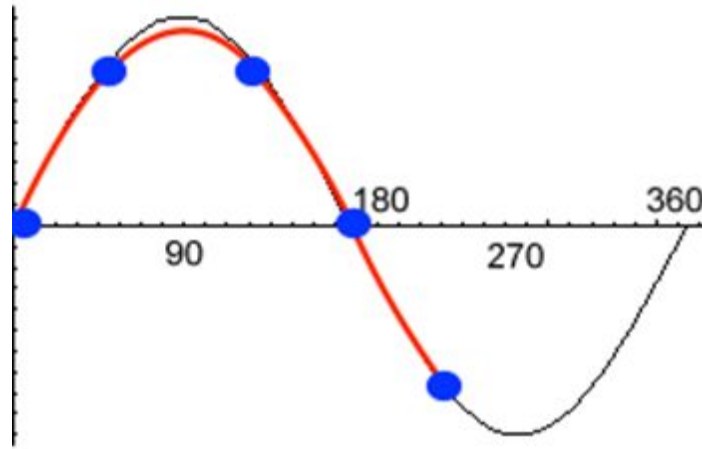


Figure 24: Smooth shaped fin

$$form = \Theta_{max} * \sin(2 * \pi * \frac{x}{\lambda}) \text{ [Equation 4]}$$

$$edgeL(r) = \int_0^{len} \sqrt{1 + (\frac{d}{dt} * form(l) * r)^2} dl \text{ [Equation 5]}$$

$$\lambda = \frac{2\pi}{\phi * n} * d \text{ [Equation 6]}$$

Equations 4 and 5 were used to calculate the fin form and edge length dimensions based on the chosen design parameters that the team set; note that these equations were originally included in the first team's report [38]. (Θ_{max}) represents the maximum angular displacement from vertical at any time and (x) represents the linear distance along the length of the fin. The team chose a maximum offset from vertical of 45° with a total swept offset of 90°. Additionally, Equation 4 is dependent on the wavelength (λ) calculated using Equation 6. Here the wavelength varies based on the number of masts (n) and the linear distance between each

mast (d). Most importantly, the wavelength is dependent on the angular position of the mast along the sine wave (Φ). The team chose a (Φ) value of 60° , as described previously to preserve the smooth curve of the sine wave. Using these calculations, the team accurately designed and fabricated test fins; the length of the top of the fin was 54.7" (radius 26.8"), the length of the bottom of the fin was 30.2" (radius 14.8"), the angle between the first and last mast when the fin is laid flat is 116.7° . The equations used to solve for these parameters are solved in the previous two teams' reports [39, 40]. Using these parameters the team constructed a flexible control fin out of 1/4" acrylic and four sheets of negligibly thin plastic; this fin, referred to as the acrylic-hybrid fin in this report, was originally designed by the first team [39]. The white and pink plastic sheets, seen in Figure 25, provide minimal stiffness while the acrylic segments help the fin keep its shape. The team also constructed two neoprene fins of various thicknesses. As fin thickness increases, so too does fin rigidity; thus thickness controls rigidity. The acrylic-hybrid fin and a neoprene fin are shown below in Figures 25 and 26.



Figure 25: Acrylic-hybrid fin



Figure 26: Example neoprene fin

Once the fin was fabricated, the team needed to ensure that the five masts of the apparatus correctly corresponded to the desired locations along the fin. The masts are limited to one degree of freedom relative to the rocker/ eccentric cam subassemblies. Each eccentric cam was fixed to the main shaft at an angular displacement of 60° relative to the next eccentric cam as defined previously by (Φ) . This relationship guarantees that the masts originally reside at 0° , 60° , 120° , 180° , and 240° positions along the sine wave. Additionally, the team designed the rockers such that the kinematic relationship between the rocker arm and eccentric cam would produce a maximum angular displacement of 45° from vertical at any time. This value set by (θ) corresponds directly to the amplitude of the sine wave.

6.4 Testing Apparatus

Over the past two years of experimentation with the fin generator, two very different testing apparatuses have been built that were optimized for use in WPI's Donahue Rowing Center and the pool in WPI's Sports and Recreation Center. The current team ultimately used both facilities for different applications.

6.5 Tow Tank

One past MQP team used the large pool in WPI's Sports and Recreation Center as a rudimentary tow tank. The apparatus they designed, which the current MQP team reused, requires users to invert the fin generator and place it on a floating platform they could pull through the water. The merits of this setup were that the water was fairly placid, the size of the

fin was not constrained by the depth of the pool, the team already had a working testing rig from a past MQP team, and the team could easily access the pool. Also, it was relatively easy to set up the entire apparatus for testing in the pool. However, this testing setup did make it difficult to collect data and tweak the fin generator *in situ* as it was constantly moving and the Vernier sensors required power from a wall plug. Furthermore, a team member had to swim behind the fin generator to keep it aligned with the flow direction. Finally, there was no ready way to measure and control the velocity of the apparatus. Ultimately the team chose to rely on the flow tank for all of their precise data collection. Still, for rapid, qualitative, and/or proof-of-concept testing, the team relied on the tow tank setup because of its ease of use and availability.

6.6 Flow Tank

The other past MQP team used WPI's Donahue Rowing Center as a simple flow tank. This team inverted their fin and suspended it over the water, ensuring water touched only the fin. This testing rig allowed for adjustments and data acquisition to be performed fairly easily because the fin generator remained stationary. However, the rowing tank was shallow (on the order of one to two feet), which limited the maximum height of the fin, and created a unique standing wave at each velocity which may have added noise to data collection. Additionally, the team was not allowed to stand in the flow channels, which made set up relatively difficult. Furthermore, it was frequently used by WPI's athletic teams and other MQP teams. Still, it remained the best option for precise data collection on WPI's campus, and thus was used

heavily by the current team.

Unfortunately, the rowing tank did not provide flow speed data, but instead the flow was increased by inputting a number from one to two thousand which corresponds linearly with flow speed. Therefore the team needed to find the scaling factor to relate the input number to the flow speed. This was accomplished by timing a float as it moved a known distance in the tank; the team's results for this preliminary testing are shown below in Figure 27. Of course, this technique only measured the surface velocity of the flow. The rowing tank is shallow, so boundary conditions in the channel created a velocity profile that impacted the fin's operation.

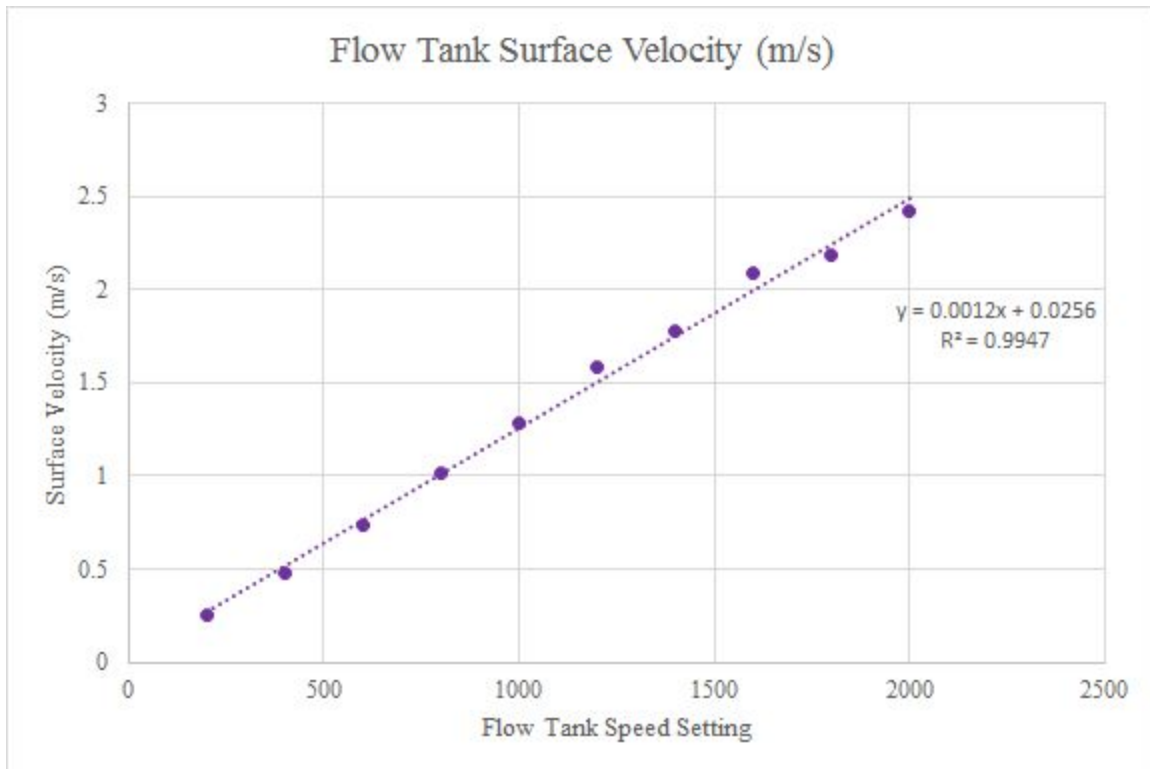


Figure 27: Flow tank speed conversion chart

7. Variables and Pre-testing Analysis

7.1 Independent Variables

The team chose to study two independent variables: fin stiffness, as controlled by material thickness, and alternate fin designs. The team conducted physical testing to determine the effect of fin stiffness whereas alternate fin designs were studied exclusively with CFD. The two main focus areas are discussed in greater detail below, but first it is worth mentioning potential research areas the team chose not to explore:

- Alternative fin materials: While further investigation can be conducted, the team felt the durability, variety, and availability of neoprene made it ideal for the scope of this report.
- Crankshaft vs. camshafts: A separate MQP team is currently working to employ a crankshaft in a different iteration of this fin generator.
- Varying fin height: While the first MQP team already showed that bigger fins produce more power, the direct relationship between fin height and power output has yet to be documented. Note that the WPI's Donahue Rowing Tank, where the team conducted their quantitative testing, has a maximum depth of about fifteen inches, which limits the amount by which the fin's height can be varied.
- The number of support masts: Theo Jansen's Strandbeest (see above) used many masts to ensure the fin maintained the proper shape. However, Jansen's device was meant to capture wind, not water, and the team felt sturdy neoprene would work sufficiently well

without the added complexity of additional masts.

- Fin swept area: By changing the cam and rocker connection point, the angular swept area of the fin can be increased or decreased, the team felt that this could impact the power output of the device and could help accommodate various water flow speeds.

7.2 Fin Stiffness

Previous teams found that if the neoprene in their masts became too thin, the fin would not be rigid enough to keep its shape. However, if the neoprene was too thick, the fin would become too heavy for the water to move and for the fin generator to support. Therefore the current team wanted to find the neoprene thickness that optimized the fin's stiffness. To do so, they constructed, to the dimensions specified in the first team's report [37], two fins with neoprene thicknesses of 1/16" and 1/8". As a control the team used the acrylic-hybrid fin described in the first team's report [37]; although this fin did not have a constant thickness, it was more flexible than either of the two neoprene fins as it is predominantly thin sheets of plastic stitched together.

7.3 Fin Shape

The fin design taken from the first team yields a fin of constant height along the direction of the water's flow [37]. The current team believed that while this design had been proven, it may not be the optimal fin design. It is possible that while the first few masts are

fully engaged, the turbulence they produce reduces the output of the last few masts; therefore the entire fin may underperform even though each individual fin is at the tallest possible height. The team thought that if the masts are ordered in increasing height along the flow direction, there will be less interference and mass so the fin will perform better as a whole.

7.4 Computational Fluid Dynamics

In order to study the effect of novel fin designs, and to provide pressure and force data unavailable in physical testing, the CFD package COMSOL was used. A three dimensional model of the fin was created and analyzed in various fluid flow situations. Beginning with a stationary, laminar flow situation, the CFD simulation was capable of determining the pressure distribution along the surface of the fin due to the water flowing past the apparatus. The fluid velocity at various locations was also determined in the simulation.

COMSOL is a powerful tool, but it requires a great deal of attention in setting up the simulation model. First, a three-dimensional model of the fin was created in SolidWorks computer aided design software; the model was then imported into COMSOL Multiphysics as an imported geometry. Second, a geometric cube was created, encompassing the fin, representing the water that flows past the fin. Finally, a union was formed between the fin and the geometric cube signifying the geometric separation between both objects; meanwhile the simulation was configured to analyze the interaction between the two objects. COMSOL provides the ability to apply material settings to each geometric component; the two objects were defined, the fin being designated as neoprene (nylon) and the cube being designated as

water. The boundary condition of the normal inflow velocity was set to 2 m/s at the leading edge of the fin in atmospheric pressure (101,325 Pa). Creating a mesh of the geometric surfaces is the final step in setting up the simulation; an “extra fine” mesh was selected in order to create one continuous surface mesh of all components. Upon completion of the simulation, COMSOL provides the ability to extrapolate data for numerous physical parameters and variables, both in two- and three-dimensional graphical representations.

Selecting “Generate Convergence Plot” under “Study Settings” instructs COMSOL to include a convergence plot with the simulation results. The plot indicates the simulation error during all simulation iterations. This plot can be used to determine the accuracy of the simulation and the corresponding number of iterations required. The pressure profile of various cross sectional regions of the fin helped the team understand the variations in pressure along the length of the fin, as well as the pressure exerted on the mast causing the mast to oscillate. A velocity profile at each mast location was also determined to understand the variation of fluid velocity along the length of the fin. Finally, the streamline profile was determined at various locations along the fin to better understand the deflection of water after coming in contact with the fin.

7.5 Finite Element Analysis (FEA)

Finite element analysis (FEA) is a virtual simulation used to determine how an object will react to real world stimulus (such as external forces, vibration, fatigue, or temperature) and discern if the object will function as intended. The team used SolidWorks to conduct analysis

of key parts where failure was anticipated and make design changes based on the results.

Additionally, a large scale design (size increased by 500%) was created and analyzed to study the effects of real world forces on a larger, theoretical device.

After studying the previous MQP group's prototype, the team decided to focus efforts on the masts and the main shaft. Deflection calculations were performed on the masts of the COMSOL model, the main shaft of prototype, and the upscaled fin's masts. SolidWorks was used to confirm these calculations. Static studies were performed in SolidWorks on these parts. In order to execute a static study, the part must be fixtured, a force must be applied, and a mesh must be created. A fixture defines where the part will remain static during the simulation, the force is applied with the desired magnitude and direction, and the mesh acts as a "skin" which deforms based on the applied force. Additionally, the simulated object must be set to the correct material so that the material properties match that of the actual object. The results presented are displacement, stress, and strain, which allow the operator to determine if the object will perform as designed.

8. Device Testing

8.1 Data Collection Apparatus

It is a well-established principle that the power of a rotating shaft is its torque (τ) multiplied by its angular velocity (ω) ($P = \tau * \omega$). Therefore, in order to measure the usefulness of the fin generator, the team needed to find a way to measure both (τ) and (ω). Note that after studying previous MQP reports, the team expected output torques up to 10 N*m and angular velocities up to 25 RPM (2.62 rad/s) [37, 38]. With torque and angular velocity information, the team generated plots comparing power, torque, angular velocity, water current speed, efficiency (the fin generator's power over the flow power equation discussed earlier in this report, Equation 1), and a nondimensional speed parameter Γ .

$$\Gamma = \frac{\omega * R}{U} \text{ [Equation 7]}$$

$$\omega = \text{Shaft angular velocity (rad/s)}$$

$$R = \text{Sine wave amplitude (m)}$$

$$U = \text{Free stream velocity (m/s)}$$

These plots provide a quantitative way to compare multiple iterations of the fin generator and help the team optimize its design and make suggestions for future work.

The team considered two possible methods to collect torque and angular velocity data, a Prony brake dynamometer and a DC motor. After researching the pros and cons of each

technique, interviewing a member of WPI's Electrical and Computer Engineering Department, and discussing the matter with their advisor, the team decided the Prony brake dynamometer was better suited for their experiments. This technique is discussed in detail below, along with a brief discussion of the DC motor technique for comparison.

8.2 Prony Brake Dynamometer

This simple technique for measuring the power output from a shaft has been used for centuries. It requires users to apply a known torque to the shaft via a lever arm and observe how the shaft's angular velocity changes. This setup is shown in Figure 28.

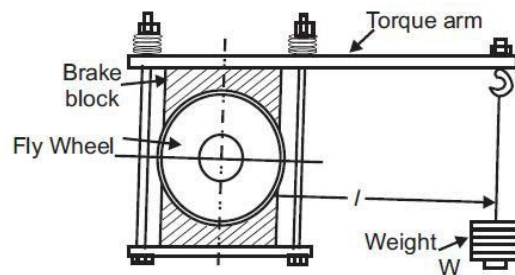


Figure 28: A diagram of a Prony brake dynamometer [40]

The user knows how much weight has been applied to the lever arm and, thus, how much torque is being applied to the rotating shaft ($\tau = W \cdot l$). In order to keep turning, the shaft must overcome the applied torque (which is transferred from the lever arm via friction). The power of the shaft is then calculated using the following equation:

$$P = N * W * l * \left(\frac{2\pi \frac{rad}{rotation}}{60 \frac{sec}{min}} \right) \text{ [Equation 8] [40]}$$

$P = \text{Power (W)}$

$N = \text{Shaft rotational speed (RPM)}$

$W = \text{Weight applied to the lever arm (N)}$

$l = \text{Length of the lever arm from the weight to the axis of rotation (m)}$

A previous MQP team used this method to measure the power output of their iteration of the fin generator [38]. That team used Vernier force and rotation sensors, coupled with LoggerPro software, to take continuous readings of the force applied to the shaft and the shaft's angular velocity. The force was applied by manually pressing a brake down onto a disk of known radius; as the brake turned with the shaft, it pulled a strip connected to the force sensor. This force was then multiplied by the disk's radius to give the torque of the shaft. This setup is shown below.



Figure 29: Dynamometer from first MQP team

In the report produced by the first MQP team to study fin-based hydropower, the team described several problems with the measurement setup shown in Figure 29, most notably that it led to vibrational noise in their data [38]. They suggested that this may have been because the rubber brake pad had too great of a coefficient of friction to slow the disk consistently, the entire testing rig was not connected securely to the fin generator, and the disk was not perfectly round.

The current team used a more traditional Prony brake dynamometer setup; it is depicted in full in Figures 30 through 32 below. Figures 30 and 31 show the full device and data collection setup from the front and side, while Figure 32 annotates the electronic equipment necessary to record data.

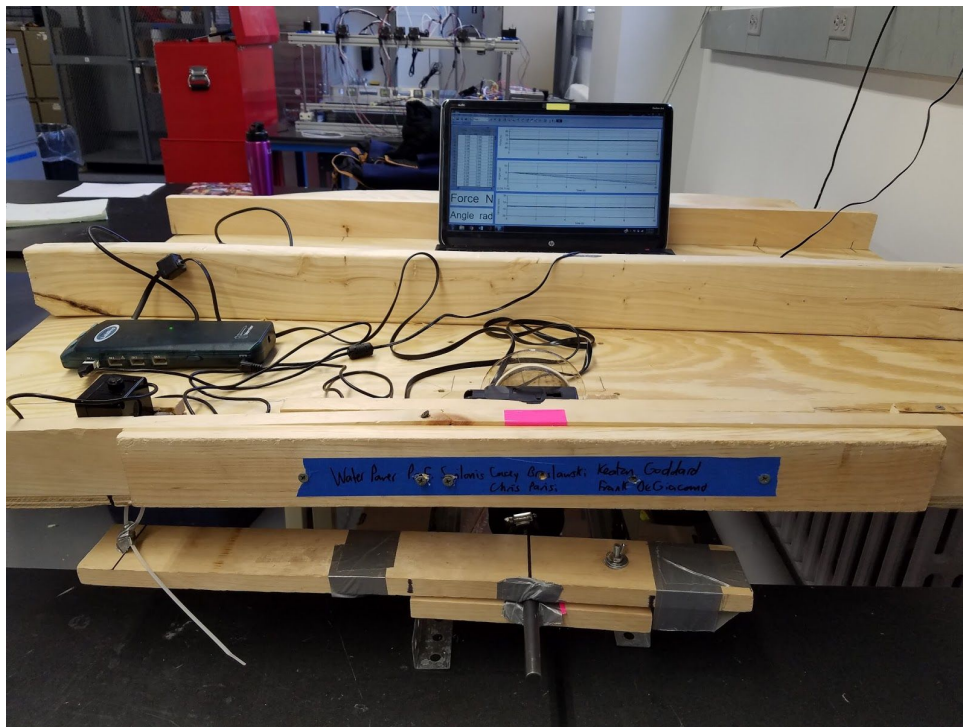


Figure 30: Device and data collection apparatus, front view

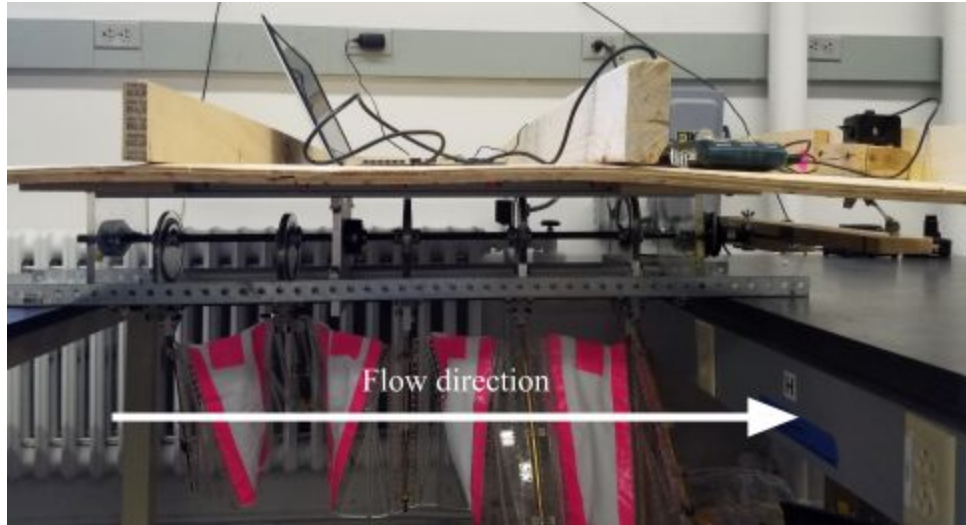


Figure 31: Device and data collection apparatus, side view

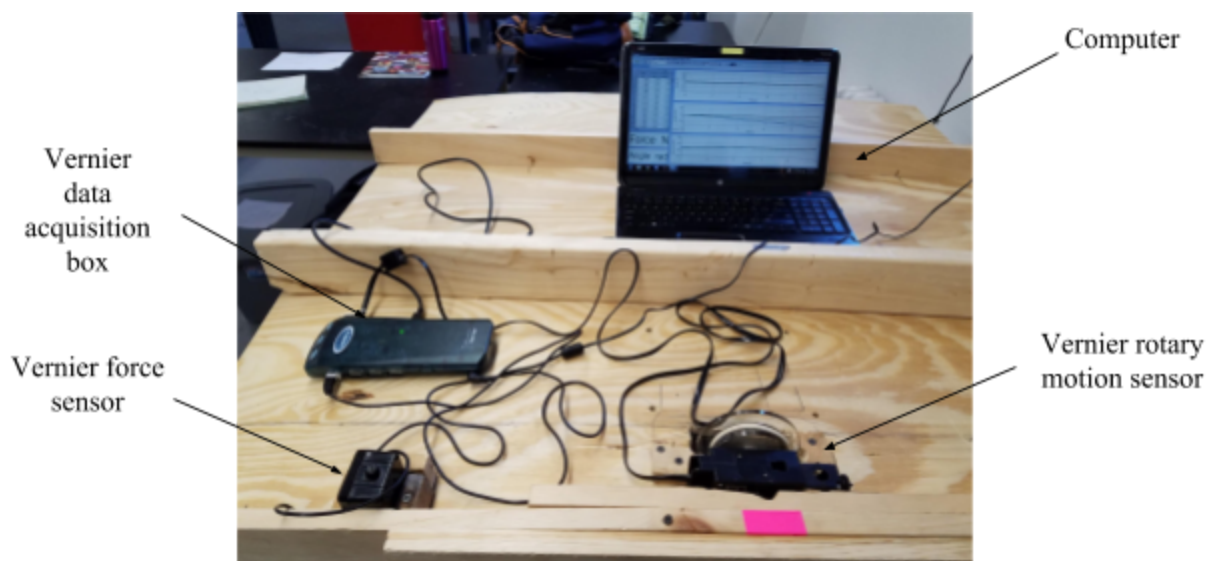


Figure 32: Data collection electronic equipment

A rubber band acted as a belt between two pulleys, one on the device's shaft (3D printed, two-inch diameter) and another on the rotational velocity sensor's shaft (laser cut,

three-inch diameter). Thus the shaft's angular velocity is transferred to and recorded by a Vernier rotation sensor. The setup is depicted below in front and top views.

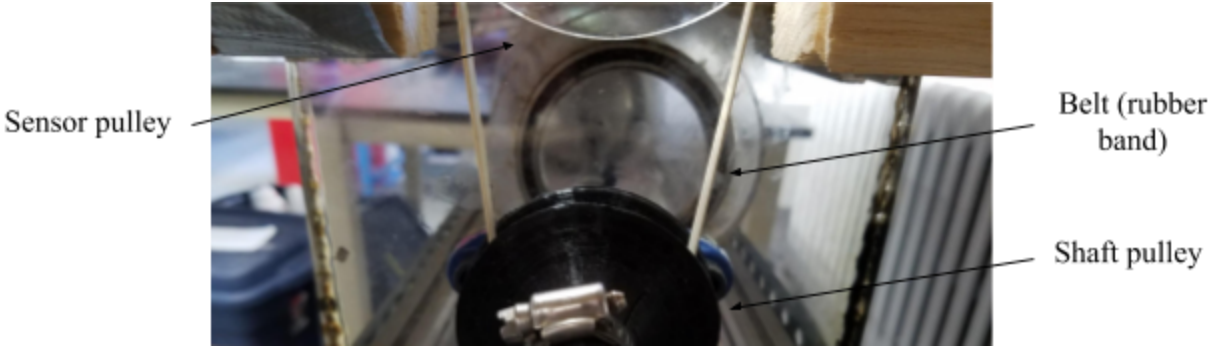


Figure 33: Angular velocity measurement apparatus, front view

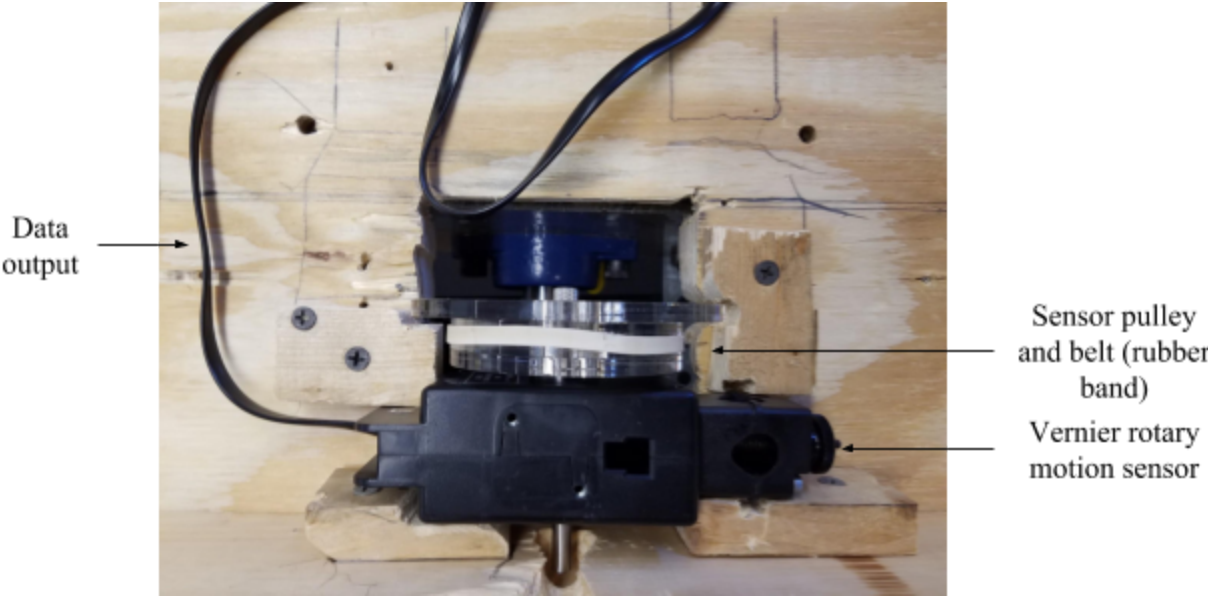


Figure 34: Angular velocity measurement apparatus, top view

The flexibility, friction, and variable tension allowed by the rubber band removed any non-rotational motion from the Vernier sensor's shaft, thereby improving the clarity of the data.

The following equation was used to find the angular velocity of the shaft:

$$V_{Sensor} = V_{Shaft}$$

$$r_{Sensor} * \omega_{Sensor} = r_{Shaft} * \omega_{Shaft}$$

$$\omega_{Shaft} = \frac{r_{Sensor} * \omega_{Sensor}}{r_{Shaft}} \quad [Equation 9]$$

$$V = \text{Linear velocity (m/s)}$$

$$r = \text{Radius (m)}$$

$$\omega = \text{Angular velocity (rad/s)}$$

In order to measure torque, and thereby calculate power, the braking force applied to the shaft must be known. To collect this data, a wooden lever arm was constructed to clamp on to the generator's shaft with variable force controlled by a wingnut; this component of the testing rig is shown in detail below.

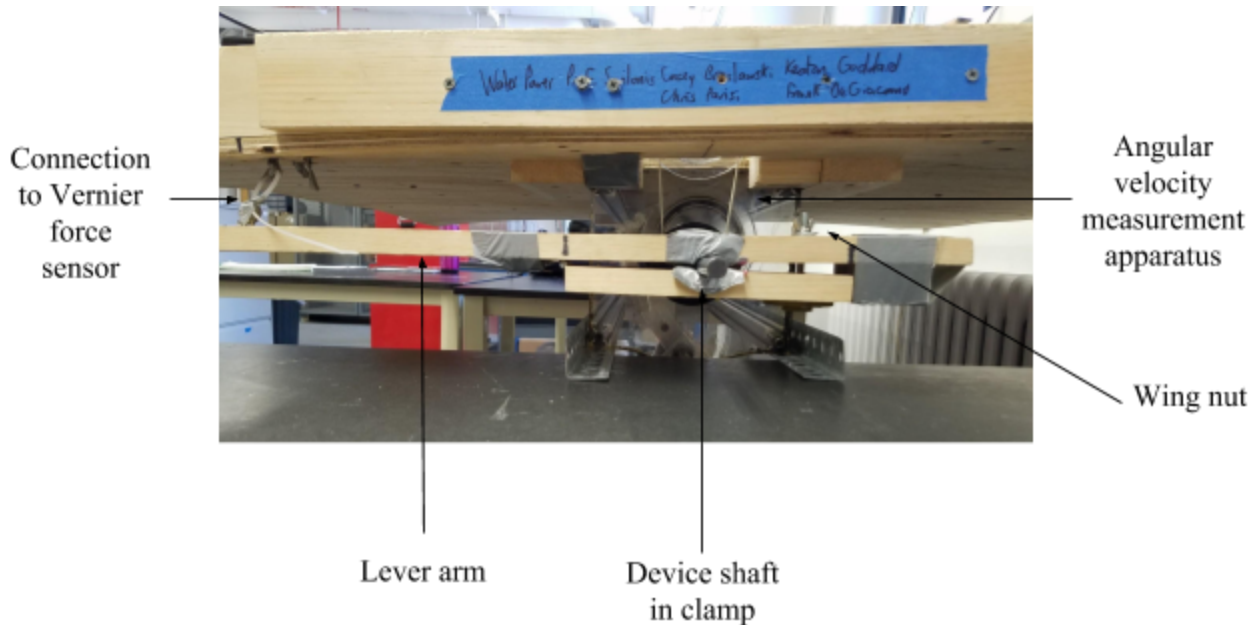


Figure 35: Prony brake

The lever arm was then connected to a Vernier force sensor positioned at a known distance from the shaft. When the wing nut loosens the clamp, minimal friction is applied to the shaft, and minimal force is applied to the sensor representing the “no-load case.” However, when the wing nut is tightened, the lever arm clamps more tightly onto the shaft; this means more friction is applied to the shaft, so it spins less freely and transfers more force to the sensor. Eventually, the clamp is fully tightened and the lever arm becomes rigidly attached to the shaft. In this case, as the shaft attempts to turn, it is stopped completely by the friction applied by the lever arm and force applied by the force sensor; therefore this represents the “maximum load case.” Note that counterweights were added to the lever arm to ensure it was evenly balanced. Additionally, the force sensor was calibrated before data was collected to ensure accuracy. The team uses a 0.35 m lever arm since the maximum force that the Vernier force sensor can record

is 50 N; a 0.35 m lever arm allows the team to record torques up to 17.5 N*m, which is well above highest torque output expected. Also, a shorter lever arm makes the entire Prony brake less cumbersome and less prone to vibration. Finally, the angular placement of the cams on the shaft determines which way the shaft spins, so the team ensured there was a place to put the force sensor on either side of the device so data collection could occur no matter which way the shaft spun.

The force and rotation sensors are supported by a large wooden board with additional planks to provide support near the force sensor; this entire apparatus is attached to the fin generator. This setup is shown above in Figure 35; note that this picture was taken in Worcester Polytechnic Institute's MQP Laboratory, and that in the flow tank the two tables supporting the structure would be wooden beams. The firm fastening, support planks, and the board's weight helped reduce vibration and erroneous measurements in the system. After a round of preliminary testing, the team bolted the testing platform to the wooden cross beams holding the entire apparatus over the water in order to further reduce vibration.

To ensure accurate data collection, the team tested the Prony brake before official data was collected; the lessons learned during this test, as well as throughout the testing process, were used to improve the team's Prony brake design. While the direct coupling of the shaft and lever arm removed the need for a wheel to transfer the force on the shaft (so long as a circular shaft was used), some trial and error was needed to find a material that could consistently and effectively apply friction to the shaft; the team found the most success in duct tape.



Figure 36: Device and data collection apparatus installed in flow tank

8.3 DC Motor

The same team that used the Prony brake dynamometer suggested later in their report that a direct current (DC) motor could provide better measurements of the fin generator system's power output. As was mentioned before, the current MQP team decided collecting data with a DC motor was not appropriate for the current stage of the project. For thoroughness, this section briefly introduces the main ideas involved in data collection via a DC motor, as well as some of the concerns the team had with this technique at this time.

DC motors rely on electromagnetic induction to convert electrical energy into the rotation of a shaft. This principle could be reversed so that by rotating the shaft of a small DC motor, an electrical voltage will be produced. Users could complete the circuit by connecting the motor's leads to a resistor. The following basic equations could then be used to determine the power generated by the shaft, which, if the angular velocity is known, could be used to find the torque of the fin generator:

$$P = I * V = I^2 * R = \frac{V^2}{R} \quad [Equation 10]$$

$$P = Power (W)$$

Iterations are derived from Ohm's Law:

$$V = I * R \quad [Equation 11]$$

$$V = Voltage (V)$$

$$I = Current (A)$$

$$R = Resistance (\Omega)$$

Thus, by coupling the output shaft of the fin generator with the input shaft of the motor, the team would have a way to directly convert the fin generator's power into measurable electrical quantities. However, upon performing some preliminary research, the team found that locating an appropriately sized motor, one that could provide sufficient torque at low voltages, was difficult. This, coupled with the necessity of setting up a microcontroller to process all of the sensors' data when Vernier sensors and LoggerPro software could readily be borrowed from WPI's Physics Department, made the selection of a Prony brake dynamometer more appealing.

8.4 Testing Methodology

The team physically tested the hypothesis that increasing the stiffness, as controlled by the thickness, of the fin will improve the device's performance (speed, torque, power, or efficiency). The control fin was the acrylic-hybrid fin designed by the first team [38]; 1/16" and 1/8" neoprene fins illustrate the effect of increasing fin stiffness. Note that all of these fins were constructed to the same specifications, and that both of the neoprene fins are stiffer and thicker than the control fin.

Each fin was tested at 600, 650, 700, 700, 750, 800, 850, 900, 950, 1000, 1100, and 1200 flow speeds (this corresponds to a range of .75 m/s to 1.47 m/s; see the conversion chart above). The smaller speed increment at lower speeds adds resolution to the team's data. This was important because preliminary testing suggested trends would be clearer with more data points at lower speeds. Vibration, the risk of damage to the fin, large standing waves in the flow tank, and time constraints prevented the team from increasing the flow tank's speed at increments of 50 at higher speeds.

The team's testing methodology is described below:

1. Install desired fin. Set up testing apparatus and place fin in the water. Do not install lever arm.
2. Set up all sensors and computers. Do not calibrate the force sensor.
3. Power on tank. Set the flow speed to 600.
4. Collect angular velocity data for 20 s.
5. Increase tank velocity. Repeat Step 4 for the other velocity cases.

6. Power off tank. Save data.
7. Install lever arm (completely loose).
8. Power on tank. Set the flow speed to 600
9. Allow flow sufficient time to accelerate. Open a new LoggerPro file and calibrate sensors.
10. Start new data series. Run data collection for 10 s.
11. Tighten wingnut. Repeat Step 10 until fin stops moving.
12. Save data. Loosen lever arm completely. Increase tank velocity. Repeat Steps 9 through 11 for remaining velocities.
13. Power off tank. Remove electronics. Remove lever arm. Remove testing apparatus/device.
14. Make necessary adjustments to fin. Repeat the above for all testing cases.

The above steps were used to collect all of the physical, quantitative data the team needed.

8.5 Calculations

For each fin at each speed, the Vernier force and rotation sensor collected a series of force and angular velocity data. This section covers how that data was processed. Because of significant scatter in the rotation sensor's angular velocity readings, the team chose to find a single value for shaft angular velocity at a given flow speed and shaft loading by taking the slope of an angular displacement vs. time graph. The force sensor's data had much less scatter, so the team simply averaged the force values collected to get a single value from each data series.

Torque was calculated by multiplying this average force by the length of the lever arm (0.35 m). Power was calculated by multiplying the torque at a given flow speed and shaft loading by the corresponding single value of the shaft's angular velocity. Efficiency was then calculated by dividing this power by the flow's power (see Equation 1 above, where area is the fin's theoretical submerged swept area). Also, a nondimensional speed parameter (Γ) was calculated using Equation 7. Finally, the efficiency data for each fin was amalgamated, standardized, and filtered such that values two standard deviations above and below the mean were removed (4.2% of data removed); the values removed were qualitatively checked to ensure they were truly outliers.

These calculations meant that for every fin, the following data was available:

- No-load angular velocity at an array of flow velocities
- Force, angular velocity, torque, power, efficiency (original and filtered), and speed parameter arrays for each flow speed

The team used this data to generate the following plots:

- No-load angular velocity vs. flow velocity (plots provided with angular velocity in radians per second and rotations per minute)
- Shaft angular velocity vs. torque
- Power output vs. torque (linear fit connects estimated peak torque values for the different flow velocities)
- Efficiency vs. speed parameter
- Filtered efficiency vs. speed parameter
- Linear regression lines for peak power output for each fin vs. torque plot
- Filtered efficiencies for each fin vs. speed parameter plot

The plots, as well as an analysis of their significance, are included in the next section of this report. Note that all of the plots are provided in Appendix A through D.

9. Results and Analysis

This section is divided into three parts so as to provide a clear discussion of the team's three main research areas. The first subsection presents and analyzes the results produced during the team's flow tank testing. The second section is dedicated to the team's simulations with the CFD package COMSOL. The third and final section covers stress and finite element analysis and uses data generated by these simulations to determine how the parts and the fin will react to forces exerted on it during testing.

9.1 Flow Tank Results

The team initially hypothesized that thicker fins would produce more power than thinner because they would better keep a sinusoidal shape and prevent "cupping" where the fin sags in between masts. However, as the team installed progressively thicker fins on the device it became apparent that, in fact, thicker fins are more difficult to turn than thinner ones. This is because the extra material on thicker fins makes them heavier and more rigid. Quantitatively, the data suggests an increase in rigidity reduces the device's power output, disproving the team's original hypothesis. After observing the different fins during operation, the team noticed that more rigid fins cannot bend and fold to accurately adopt the appropriate sinusoidal shape; additionally, thicker fins were less able to rotate about the masts, which hindered their performance.

The presentation and discussion of the team's quantitative data begins with a subsection wherein the results generated from the preliminary and modified testing apparatus and methodology are compared. Next, the overall trends in the team's fin thickness tests are illustrated and discussed with cumulative power vs. torque and filtered efficiency vs. speed parameter plots. Finally, the bulk of the team's data was visualized by plotting shaft speed vs. torque, power vs. torque, and efficiency vs. speed parameter for each fin. The presentation and analysis of each of these plots is included in its own separate subsection below. Note that additional plots (shaft speed vs. flow speed, in RPM and rad/s, and individual efficiency vs. torque for each fin) are included in the Appendix A through D.

9.2 Improvements to Testing Methodology and Apparatus

The team performed their first flow tank test with the acrylic-hybrid fin. After observing the fin in operation, they made certain critical changes to the testing methodology and rig to improve the clarity and accuracy of the data collected during all subsequent tests. For this reason the team tested the acrylic-hybrid fin a second time with the revised procedure; the results from this second test are used to compare the acrylic-hybrid fin to the neoprene fins. However, the data collected during the first round of testing with the acrylic-hybrid fin can be compared to that of the second test with the same fin. This illustrates the effect of the changes to the testing methodology and apparatus.

The team made three major changes to the testing procedure and equipment. One was to increase the tension in the rubber band connecting the sensor's shaft to the device's shaft by

increasing the diameter of the sensor's pulley from 0.75" to 3"; this helped reduce vibration in the rubber band, which caused the sensor's shaft to turn more regularly. Another improvement was to increase the Prony brake's ability to clamp on to the device's shaft by decreasing the diameter of the hole in the Prony brake with duct tape and tightening down on the brake's wing nut with pliers. This allowed more force to be measured by the force sensor as well as more data points to be collected at each flow speed. The final major adjustment the team made to the testing apparatus after preliminary testing was bolting the data collection platform to the rig's wooden cross beams. This helped reduce vibration in the entire system, which improved the device's operation, ensured the fin submersion level remained constant at the given speed, and improved the accuracy of the data collected by the force and rotation sensors. Note that efforts to reduce vibration in the system were especially valuable at higher flow speeds.

The team observed immediate improvements in the operation of both the device and the testing apparatus: the entire system vibrated less and the shaft's sensor spun more smoothly. Generally speaking, these improvements were reflected in the collected data. To begin, the shaft's angular velocity vs. flow speed plots showed consistent results between the two tests; these plots are shown below in Figure 37 (angular velocity in RPM, plots in rad/s are included in Appendix A through B). The main difference between these two plots is that more data points were collected during the second test than the first in order to provide a better picture of how the device performs. Increasing the number of data points may have caused the R^2 value on the new plot to decrease as there is more opportunity for error, but because the R^2 values are comparable despite the large increase in the number of data points the team's adjustments to the testing apparatus and methodology are verified. Additionally, variance may have been caused by

changes in the tank's water level between tests.

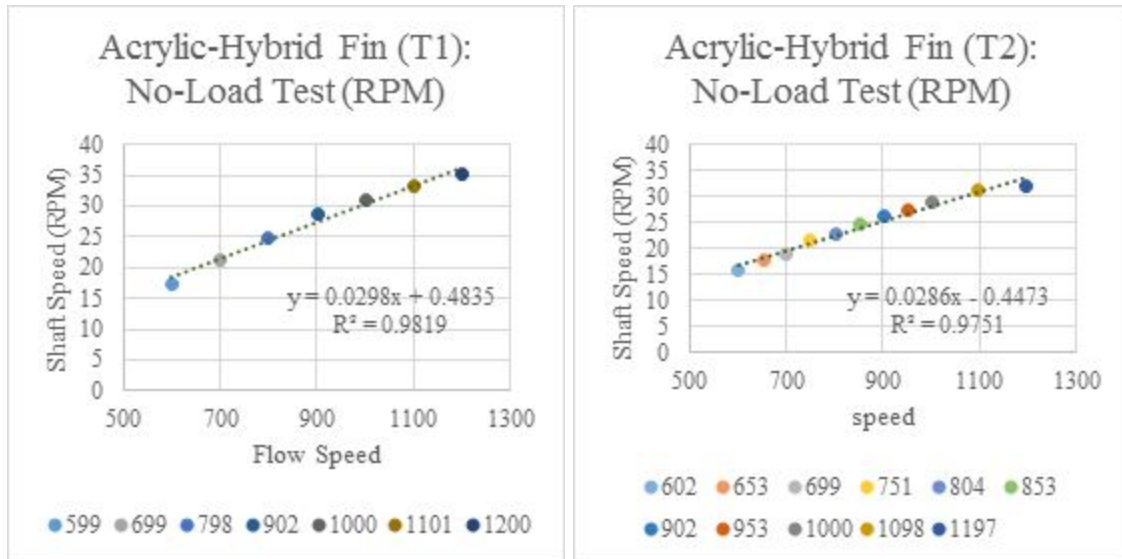


Figure 37: Acrylic-hybrid Fin RPM Tests 1 and 2

The data shown in the following RPM vs. torque, power vs. torque, and filtered efficiency vs. torque plots all demonstrate the same general effects of improving the data collection methodology and apparatus; these plots are shown in Figures 38 through 40. Figure 39 includes a linear trendline, as well as its equation and R^2 value, which fits the peak power values for each flow speed before and after the methodology and testing apparatus improvements. For clarity the flow tank's speed dimensions were used for Figures 38 through 40; see Figure 27 for a conversion between these speed units and meters per second.

To begin, more data points were collected, which adds merit to any observed trends. Also, despite the increase in data points, when R^2 values were calculated they increased, most likely due to a decrease in vibration. Additionally, the team was able to collect peak load (no

shaft angular velocity) data. The observations discussed above show that the changes made to the testing apparatus and methodology improved the system overall and helped the team make important quantitative observations.

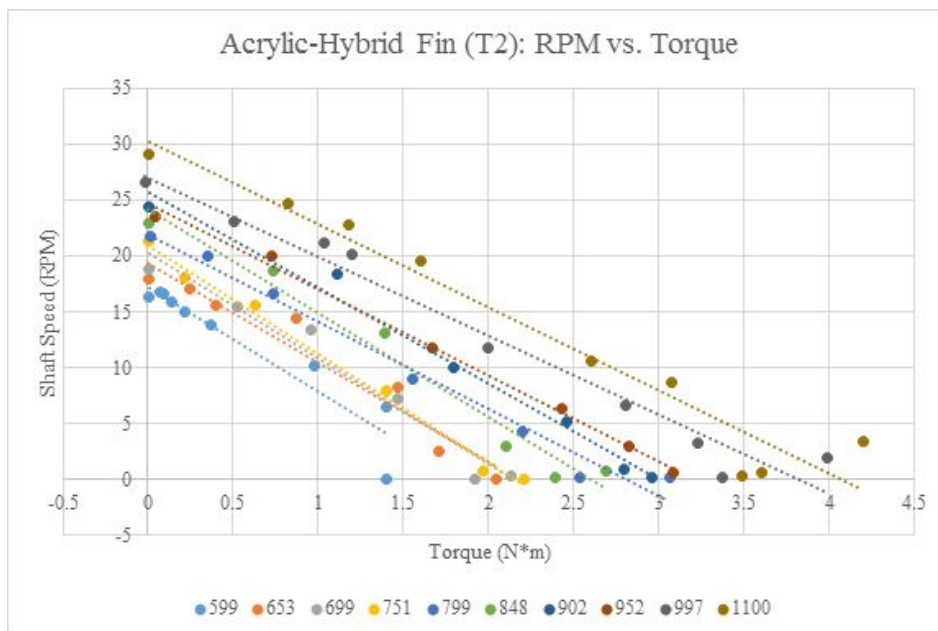
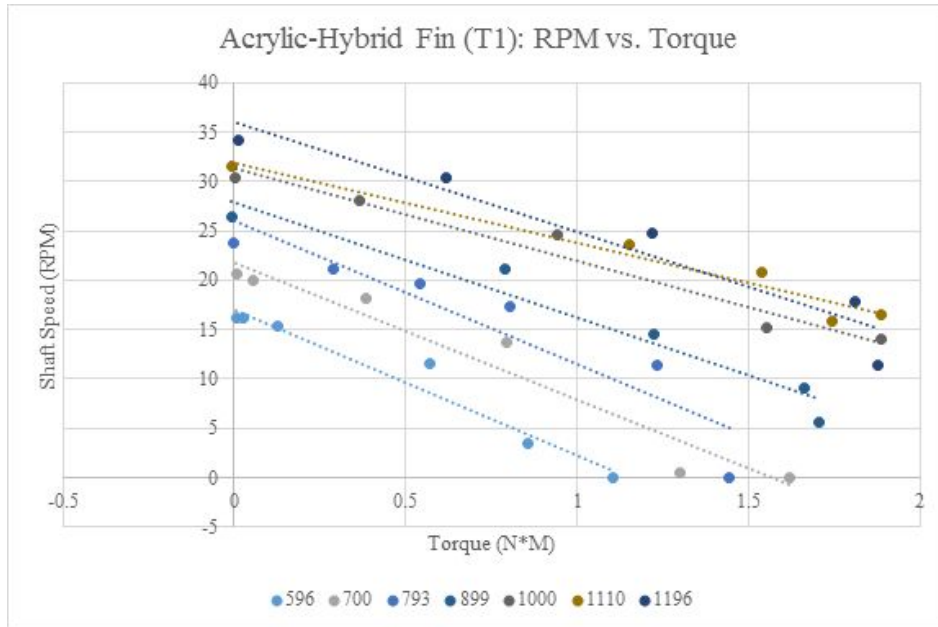


Figure 38: Comparison of acrylic-hybrid fin RPM vs. Torque plots

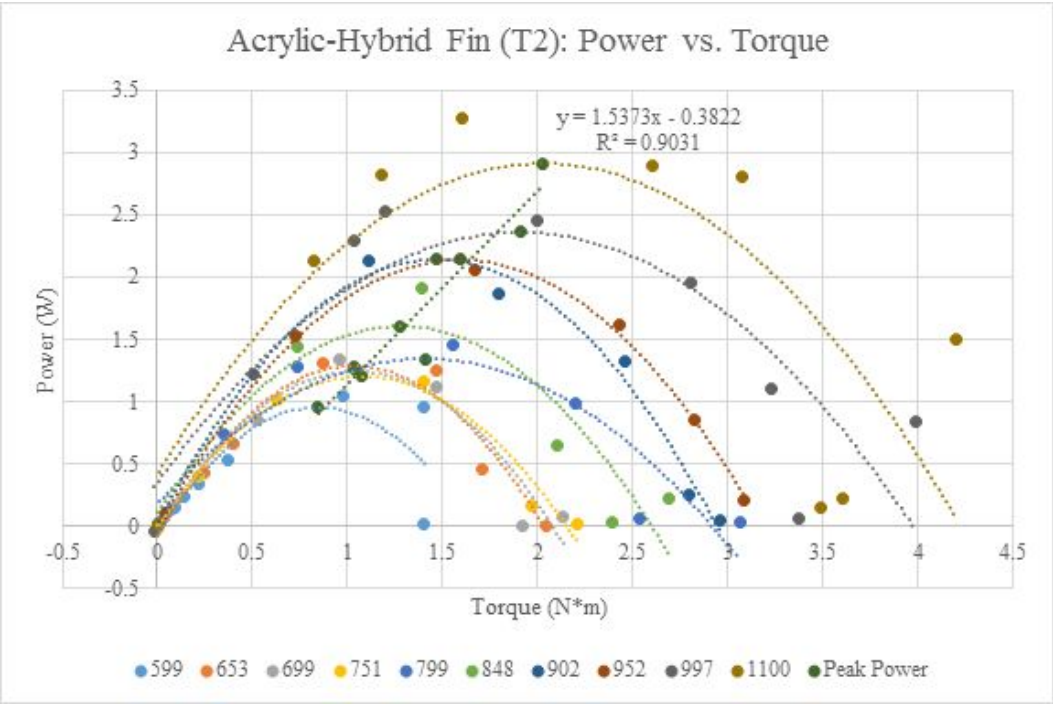
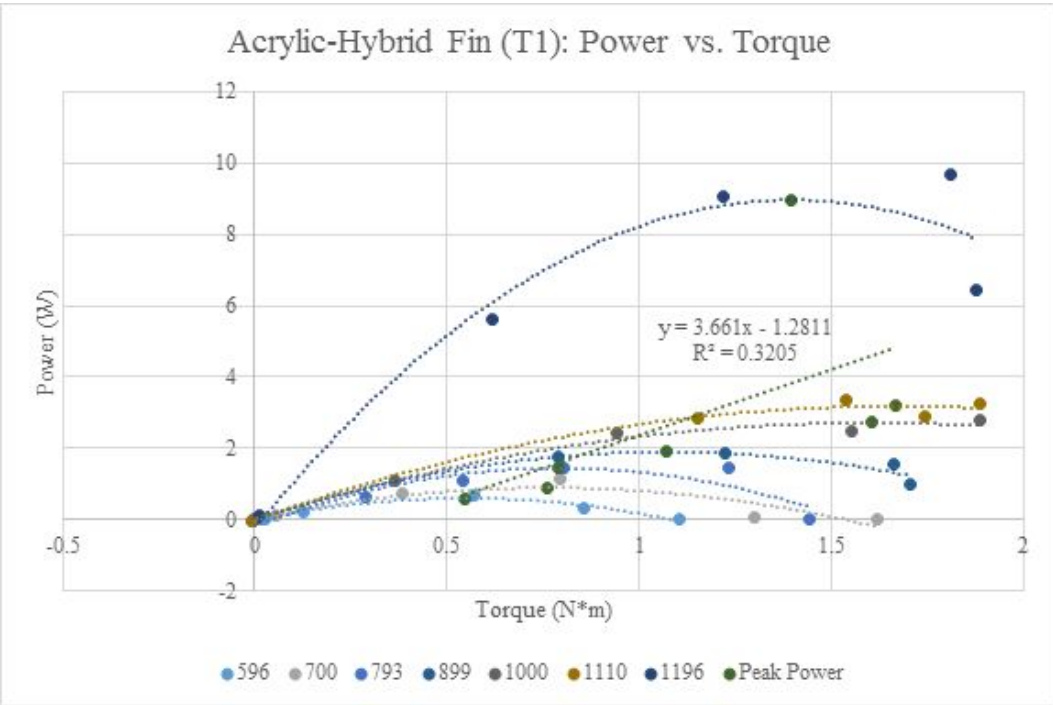


Figure 39: Comparison of acrylic-hybrid fin Power vs. Torque plots

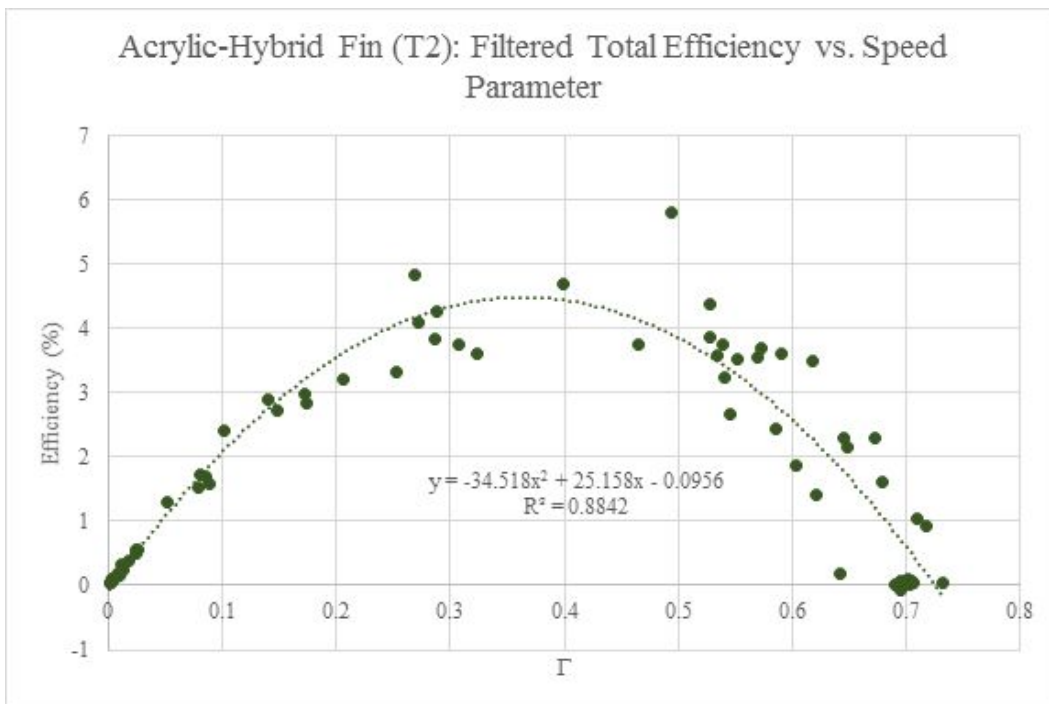
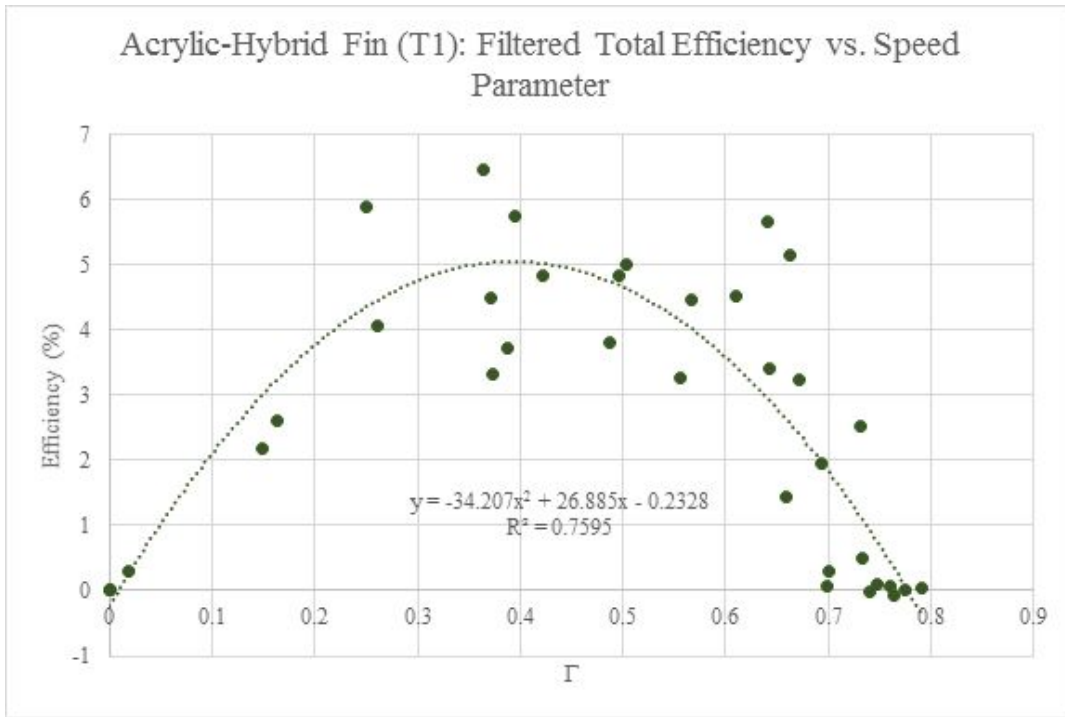


Figure 40: Comparison of acrylic-hybrid fin Filtered Total Efficiency vs. Speed Parameter plots

9.3 Fin Stiffness Testing Overall Results

The team's original hypothesis is refuted by the data collected during flow tank tests, as well as qualitative observations. For each of these fins, the team combined all of the filtered efficiency and peak power trendlines, then plotted the peak power and filtered efficiency results on two graphs (Figures 41 and 42, respectively). Doing so allows for immediate comparison between all of the peak power and filtered efficiency data collected for the three cases.

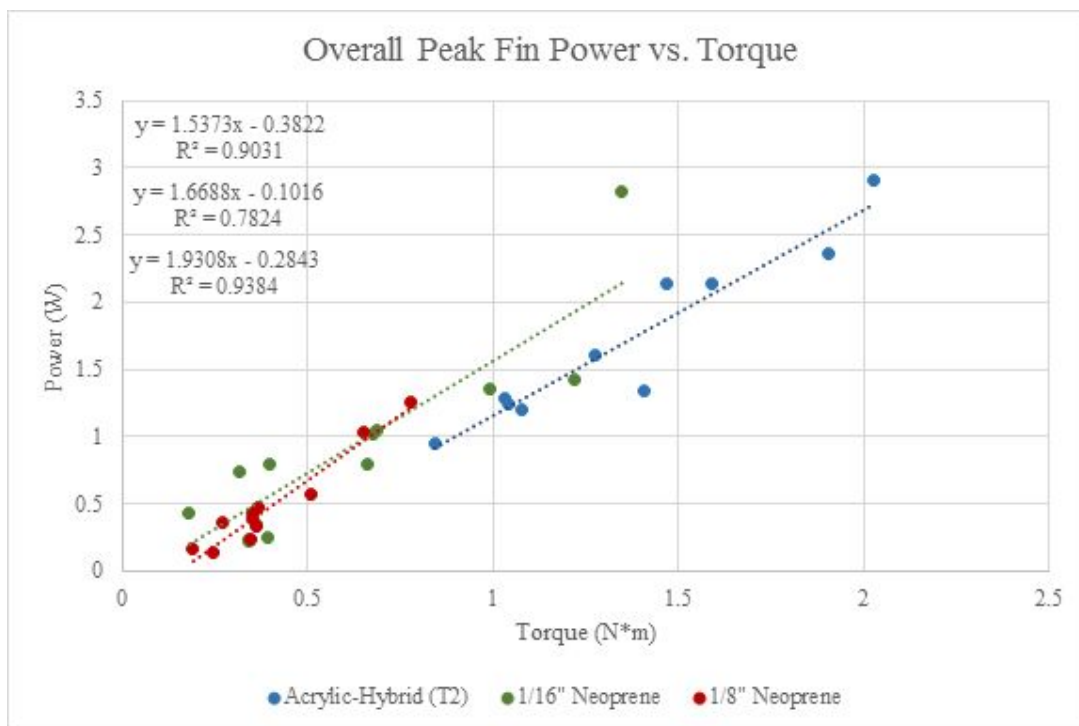


Figure 41: Comparison of peak power trendlines

Figure 41 shows that as the fin thickness increases, the peak power range decreases; for

example, the acrylic-hybrid fin (blue trendline), predicts higher torque and power outputs than the 1/8" neoprene fin (red trendline). It therefore makes sense that the intermediary 1/16" fin (green trendline) fills the performance gap between the two extreme fins. The similarities between all three trendlines suggest that a single trendline could be applied to all of the collected data. This makes sense because, apart from the fin, the device's performance does not change between tests. Therefore if a thicker fin is, for example, 50% as effective as a thinner fin, the relationship between power and torque should scale accordingly along the device's overall performance curve. The team's data supports this theory and suggests that not only do thinner fins outperform thicker fins, but also that the team successfully isolated the fin thickness variable and its effect.

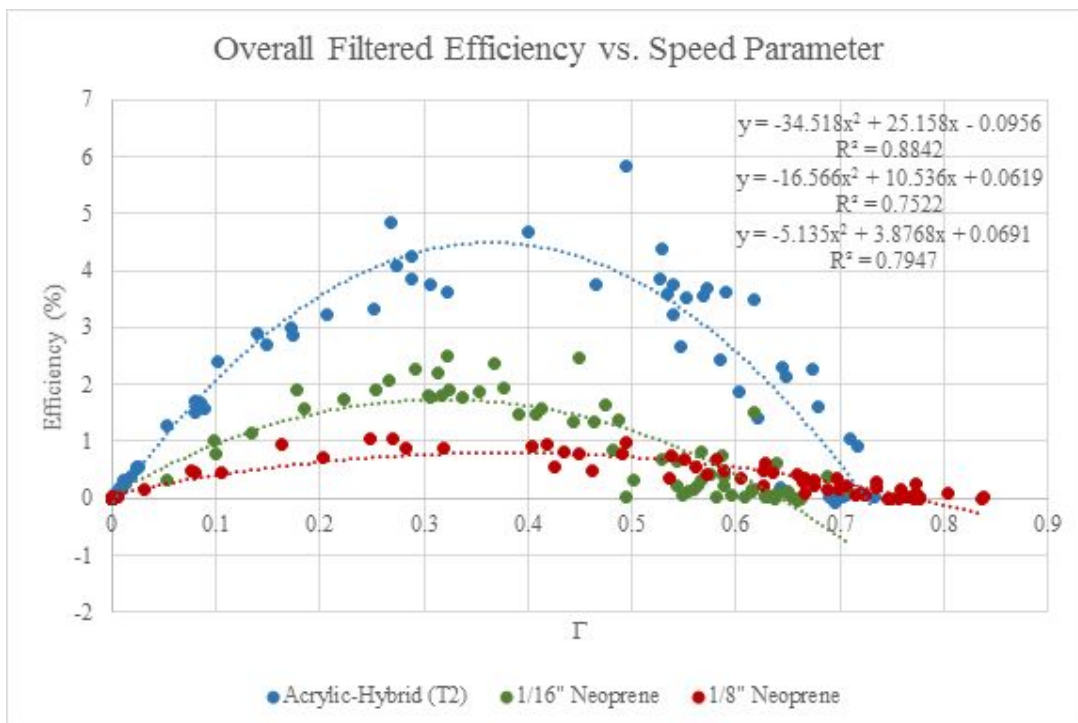


Figure 42: Comparison of filtered efficiency data

The overall filtered efficiency plot, Figure 42, further quantifies the above finding. It shows that the device's, or moreover the fin's, efficiency drops as the fin's thickness increases. However, efficiencies always begin and end at $\Gamma=0$ and $\Gamma\approx 0.7$, respectively, and peak between approximately $\Gamma=0.3$ and $\Gamma=0.4$. These three "control points" are set by the device (camshaft, rocker, bearings, etc.); any variation the curves in Figure 42 display is entirely due to different fins. It seems that as the fin's thickness doubles, the device's peak efficiency halves; for example, between the 1/16" fin (green trendline) and the 1/8" fin (red trendline) the peak efficiency drops from approximately 1.75% to approximately 0.875%. The trend roughly continues for the acrylic-hybrid fin (blue trendline), which has a peak efficiency of approximately 4.5%. However, it is important to note that while the acrylic-hybrid fin is the thinnest and most flexible of those tested it is not neoprene nor of uniform thickness, so without verifying the actual rigidity of the three fins the team can only surmise the continuation of the exact halving relationship between fin thickness and peak efficiency to this fin is largely coincidental.

9.4 RPM vs. Torque

The shaft speeds remain approximately the same between each fin under no-load conditions, ranging between about 13 and 30 RPM for the acrylic-hybrid fin, about 13 and 30 RPM for the 1/16" neoprene fin, and about 13 and 40 RPM for the 1/8" neoprene fin. This

suggests that fin thickness has no effect on shaft speed. However, the similarity between fins ends here; the torque output of the device varies greatly depending on the fin. Peak torque for the acrylic-hybrid fin ranges from 1.5 to 4.25 N*m, depending on flow speed. Peak torque for the 1/16" fin drops to a range of 0.5 to 2.75 N*m. Peak torque for the 1/8" fin drops again to a range of 0.4 to 1.5 N*m. The acrylic-hybrid fin has approximately twice the torque output of the 1/16" fin, and, coincidentally, the 1/16" fin has approximately twice the torque output of the 1/8" fin. This suggests that more flexible fins are more effective than more rigid fins.

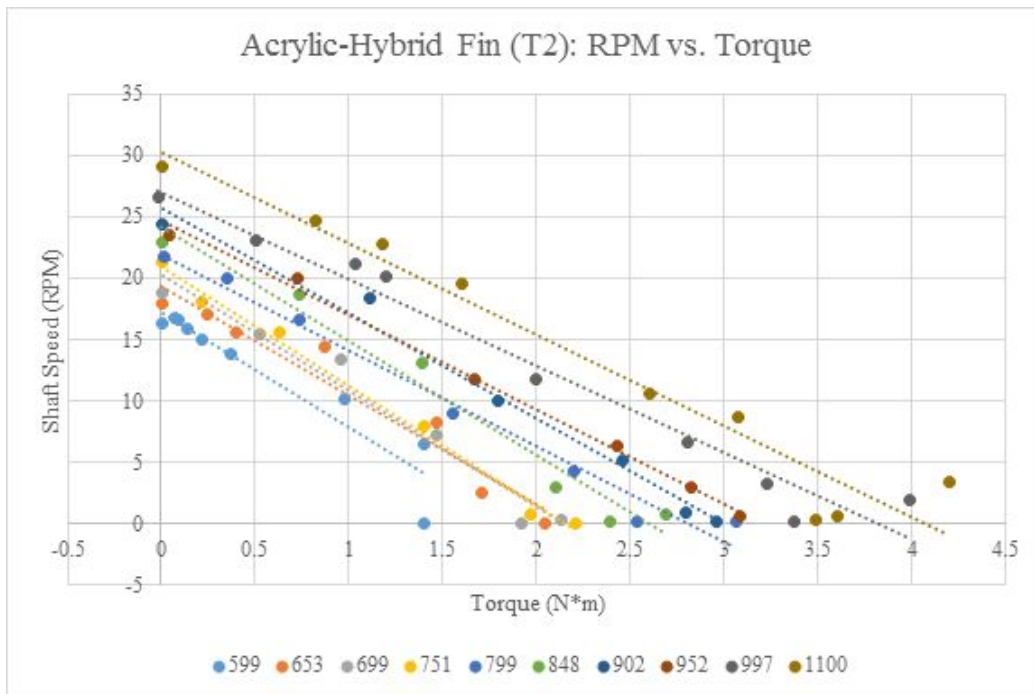


Figure 43: Acrylic-hybrid Fin RPM vs. Torque plot

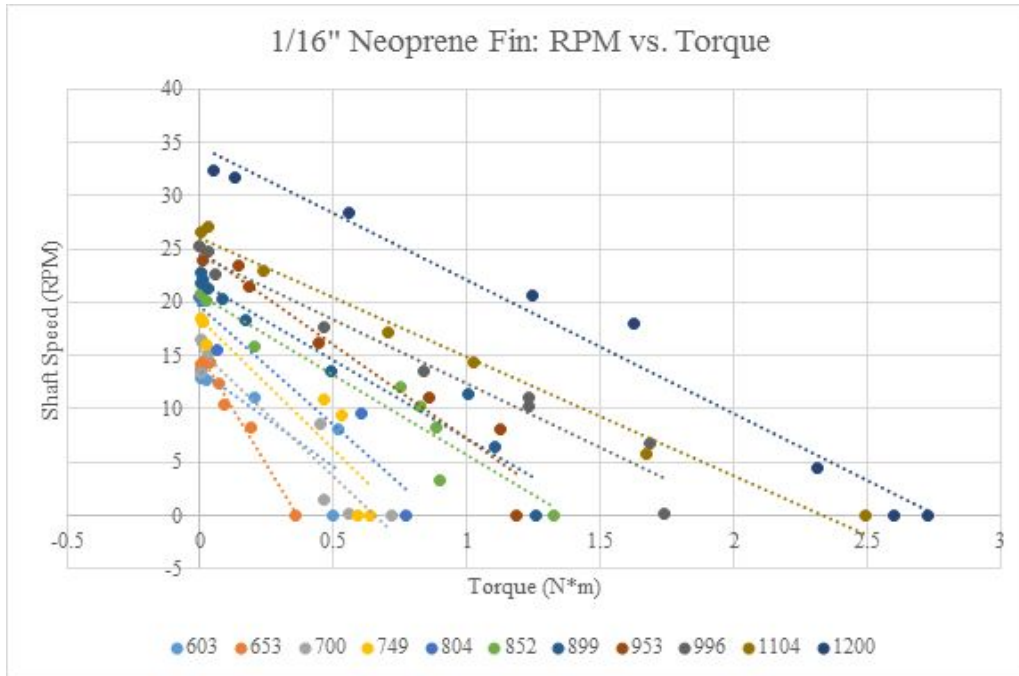


Figure 44: 1/16" Neoprene Fin RPM vs. Torque plot

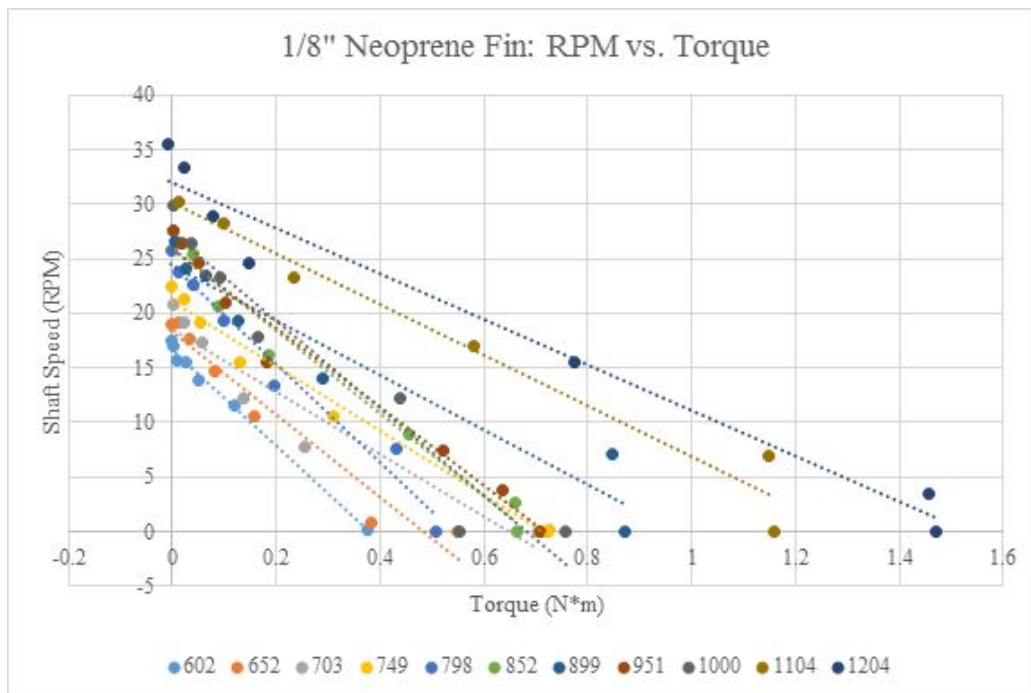


Figure 45: 1/8" Neoprene Fin RPM vs. Torque plot

9.5 Power vs. Torque Results

Using the data collected during flow tank testing the group determined the associated power vs. torque curves for the acrylic-hybrid fin, the 1/16" neoprene fin and the 1/8" neoprene fin. Focusing on the acrylic-hybrid fin, angular velocity data was collected for various applied torques at 10 different rowing tank speed settings. Using the angular relationship for power ($P = \tau * \omega$), a power curve for each flow speed of the tank was generated. Figure 46 shows the power vs. torque relationship for the 10 rowing tank speed settings collected while testing the acrylic-hybrid fin (T2). A linear trendline, as well as its corresponding equation and R^2 values, has been added to Figures 46 through 48 to demonstrate the connection between the peak powers for each flow velocity case for the three fins tested.

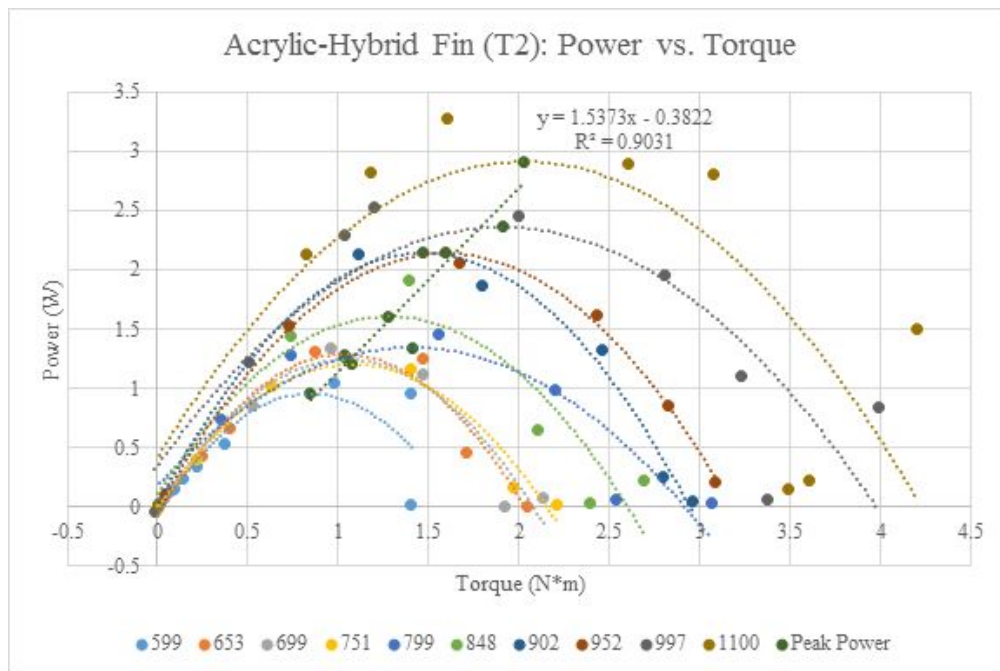


Figure 46: Acrylic-hybrid Fin Power vs. Torque plot

Additionally, power vs. torque curves were generated under various flow speed settings for the 1/16" neoprene fin and the 1/8" neoprene fin following the same plotting method. These power curves can be seen in Figures 47 and 48, respectively.

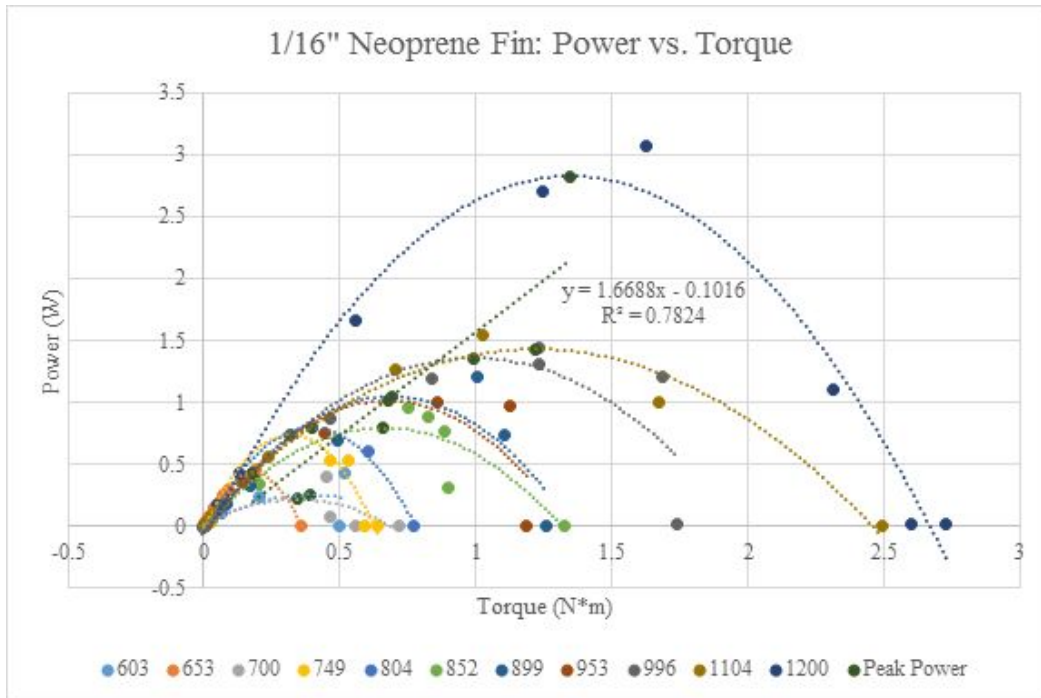


Figure 47: 1/16" Neoprene Fin Power vs. Torque plot

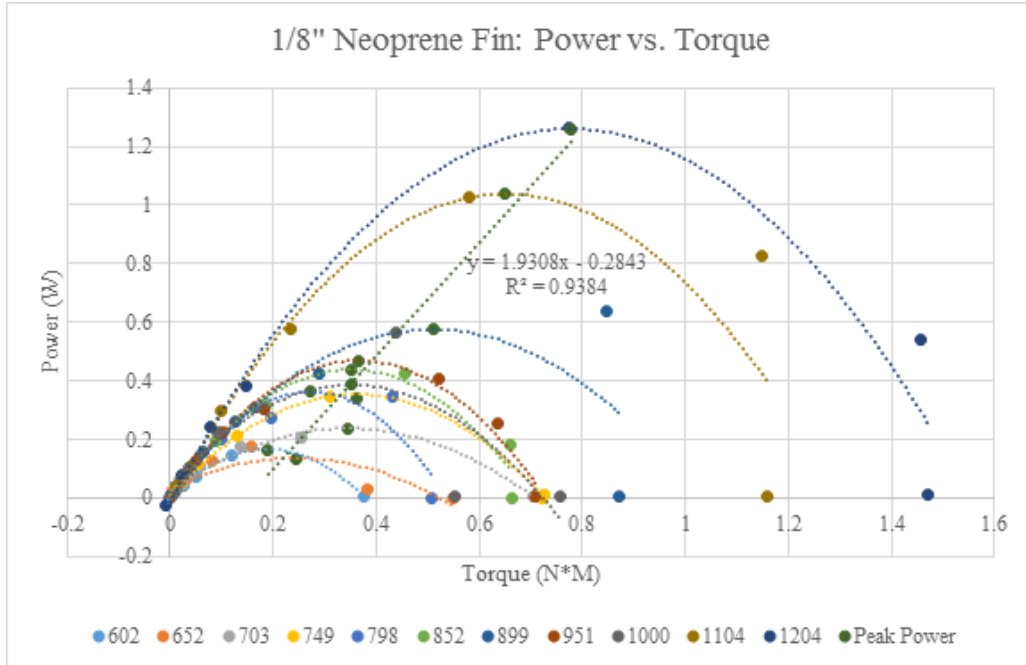


Figure 48: 1/8” Neoprene Fin Power vs. Torque plot

For the acrylic-hybrid fin, the resulting R^2 value for the linear trendline is 0.9031, for the 1/16” neoprene fin the R^2 value is 0.7824, and for the 1/8” neoprene fin the R^2 value is 0.93837. Again, it is reasonable to believe the peak power generated by each fin follows a linear relationship relative to the flow speed. Using the peak powers for each flow speed setting, valuable comparisons can be made between the three fins.

The linear trendline of the peak powers for the acrylic-hybrid, 1/16” neoprene, and 1/8” neoprene fins shows a peak power of approximately 1 to 3 W, 0.25 to 2.1 W, and 0.1 to 1.2 W, respectively. This analysis of the peak power trendlines for each fin confirms the existence of a trend between fin flexibility and power extraction. The acrylic-hybrid fin was very flexible and required the least amount of startup torque to begin the sine wave propagation along the fin. This fin also extracted the highest range of peak power during testing. In comparison, the linear

trend of the peak power for the 1/16" fin, which is of medium stiffness, shows that the range of peak power was less than that of the acrylic-hybrid fin. This adds merit to the trend that more flexible fins can perform better than stiffer fins. This trend is further supported by the data collected from the 1/8" neoprene fin, which was the stiffest of the three fins tested. The 1/8" neoprene fin shows the lowest range of peak power output. These results follow to a logical conclusion that the stiffer the fin, the more energy required to propagate the sine wave and the less power extractable from the water through the fin.

9.6 Efficiency vs. Speed Parameter

Considering the aforementioned trend, that more flexible fins produce more power than rigid fins, it makes sense that more flexible fins are also more efficient than rigid fins. The team presents the efficiency data below in the form of efficiency vs. speed parameter plots (Figures 46 through 48). It is expected that for each fin all of the efficiency data falls on the same parabolic trendline when plotted against the speed parameter Γ . This trend is observed and, along with the peak efficiencies for each fin, discussed below.



Figure 49: Acrylic-hybrid Fin (T2) Efficiency vs. Speed Parameter plot

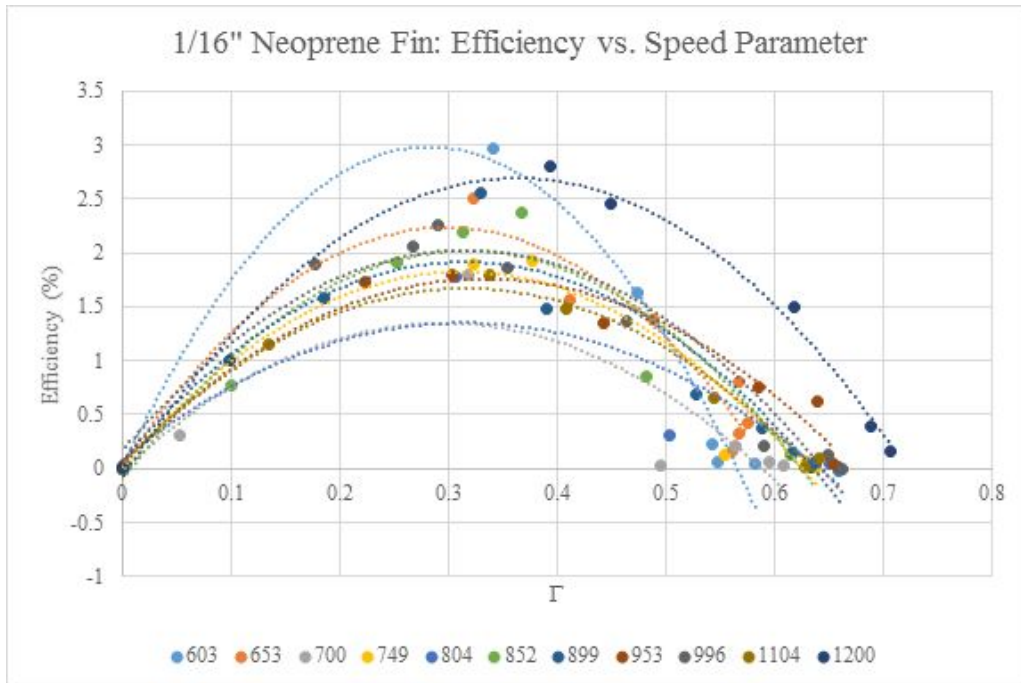


Figure 50: 1/16 “ Neoprene Fin Efficiency vs. Speed Parameter plot

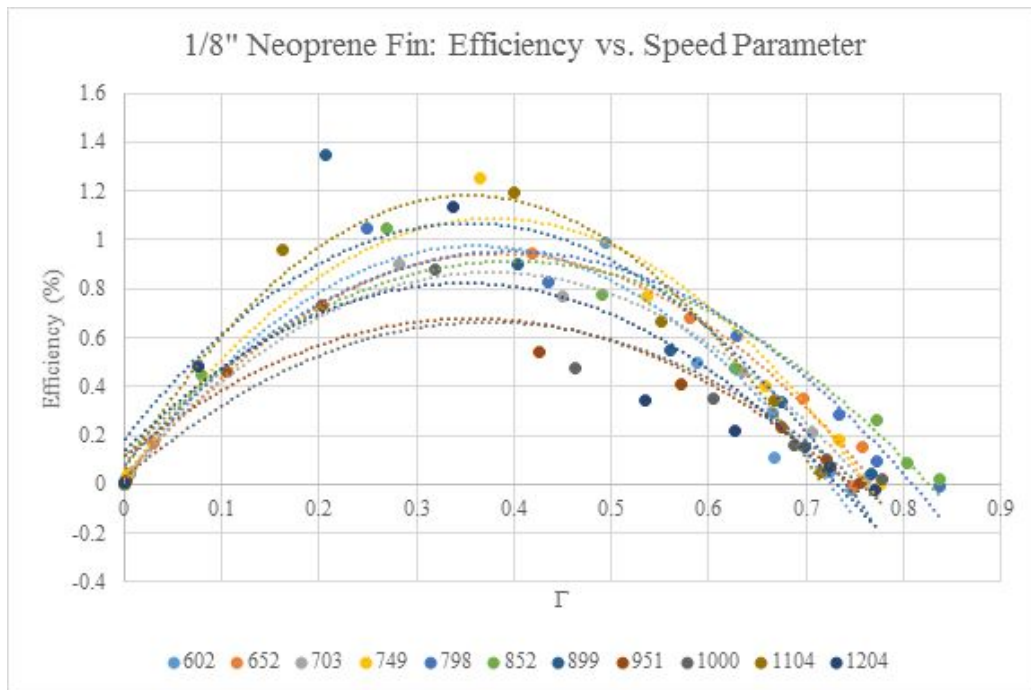


Figure 51: 1/8” Neoprene Fin Efficiency vs. Speed Parameter plot

An analysis of Figures 49 through 51 reveals several noticeable results. To begin, all of the fins operate most efficiently when Γ is between approximately 0.3 and 0.4; this immediately suggests that there exists an optimal shaft speed which depends on the velocity of the fluid. This could be valuable for future work when gearing must be used to connect the device’s shaft to a generator. Another interesting result is that the device performs most predictably when the flow is between 700 (0.8 m/s) and 1100 (1.35 m/s). This is visible in the graphs generated for each flow speed in which the parabolas are the most clustered within this range. This provides another suggestion for the optimal operating conditions of the device.

This section provides additional support for the observation that more flexible fins outperform more rigid fins. This observation was quantified by analyzing the peak efficiencies

for each fin. The peak efficiency of the acrylic-hybrid fin in Figure 49 was approximately 5%. The peak efficiency of the 1/16" neoprene fin in Figure 50 was approximately 2%. The peak efficiency of the 1/8" neoprene fin in Figure 51 was approximately 0.8%. The acrylic-hybrid fin was the most efficient of the three fins tested. The 1/16" neoprene fin had approximately double the efficiency of the 1/8" neoprene fin, and coincidentally the acrylic-hybrid fin had approximately double the efficiency of the 1/16" fin. With more fin thickness testing, the team concludes that this efficiency trend would continue. This supports the overall trend that more flexible fins outperform more rigid fins.

9.7 Sources of Error

It is important to note that the acrylic-hybrid fin failed during the second round of testing at the 1200 flow speed. This means that the data the team collected at this speed is unreliable and was omitted from the analyses. Also, throughout the fin thickness testing the team added constraints to the testing apparatus to reduce vibration during testing. While technically this does add an additional variable to the results, in reality it did not affect the fin's overall performance, but rather just reduced the scatter in the data. Finally, the water level changed between individual rounds of testing; for the first acrylic-hybrid fin test, the team did not measure fin submersion (9" was assumed), for the neoprene fins 9" of the fin was submerged, and, finally, for the second acrylic-hybrid fin test 10" of the fin was submerged. Fin submersion obviously has a profound effect on the device's performance, so this is one of the main sources of error in the data. Other sources of error include unquantifiable friction in the components of

the apparatus, vibrations of the overall device, and the location of a standing wave in the rowing tank.

The presence of the standing wave in the rowing tank was especially detrimental to the team's testing, as at times the majority of the fin was caught in a trough and was therefore only partially submerged. This means the actual portion of the device capable of generating power changed depending on the presence, location, and size of a standing wave in the tank. The team believes that as little as 33% of the fin was in the water when the standing wave caused a large trough to form where the fin was placed. Unfortunately, the standing wave moved to different locations at different flow speeds and changed depending on water depth. Additionally, the team installed the fin at different locations in the tank between different fin tests, so it is not possible to use a single correction factor to adjust the team's data to account for the standing wave's effect. Thus managing the standing wave should be an important objective for any future research.



Figure 52: Standing wave in flow tank (1200 speed)

9.8 Computational Fluid Dynamics (CFD) Results

Originally the team decided to physically test numerous fin thicknesses, fin displacement ranges, and various fin shapes to determine an optimal fin from the options presented, but the team felt there would not be enough time to test these numerous options and collect accurate data. The team determined they would reduce the number of physical tests by eliminating the various fin shape tests, leaving this analysis to simulation through COMSOL Multiphysics. The control fin, adopted from previous project work [37], measures a constant height of 12 inches. A CAD model of this fin was created in SolidWorks and imported into COMSOL Multiphysics for use in fluid simulation and analysis. Following the previously described simulation setup procedure, Figure 53 shows the resulting pressure distribution along the surface of the fin resulting from the simulation. These pressure distributions aid in identifying the net pressure along specific regions of the fin. While COMSOL Multiphysics has the ability to integrate the pressure distribution over the area of the fin and report the net force over the entire surface, the pressure distribution over a small differential area was more important in specific regions, especially the mast locations along the fin. Using the pressure distribution, the team was able to determine an average pressure, average force, and torque along various regions of the fin. This analysis helped the team determine which fin shape would provide the best power producing capability. The shape and pressure distribution of the control fin were used as the baseline measurement to compare to the various fin shapes simulated in COMSOL Multiphysics. The varying fin shapes were modeled using an increasing wave height along the length of the fin. While the control fin has a constant height of 12 inches along the length of the fin (Figure 53),

Test Fin 1 is a constant height of three inches along the length of the fin (Figure 53). Figure 53 through 56 are included purely for illustrative purposes, and a quantitative analysis of COMSOL’s simulation results is included later in this report.

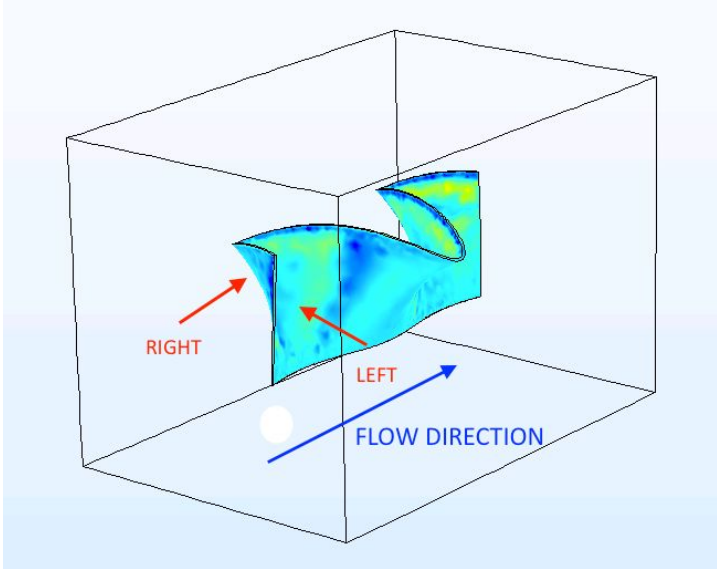


Figure 53: Pressure distribution along Control Fin surface

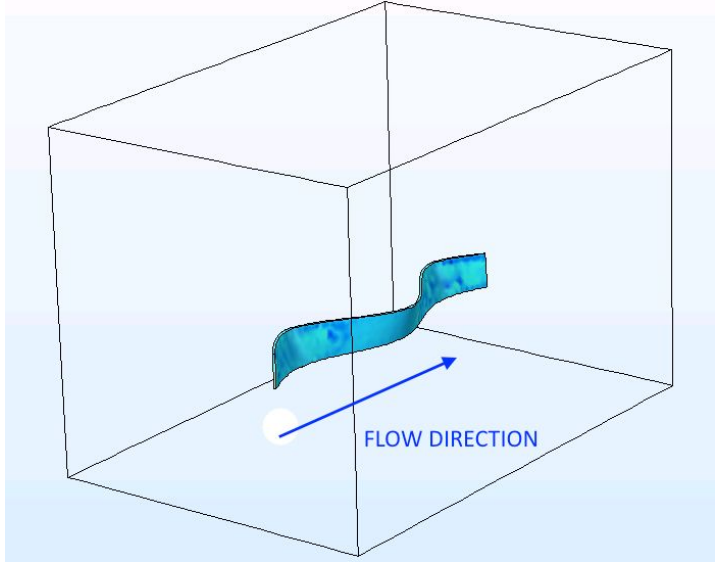


Figure 54: Pressure distribution along Test Fin 1 surface

Test Fin 2 has a fin height of three inches at the leading end and a height of nine inches at the trailing end. A side view of the fin shows a linear height increase such that the middle of the fin has a height of six inches; Test Fin 2 can be seen in Figure 55.

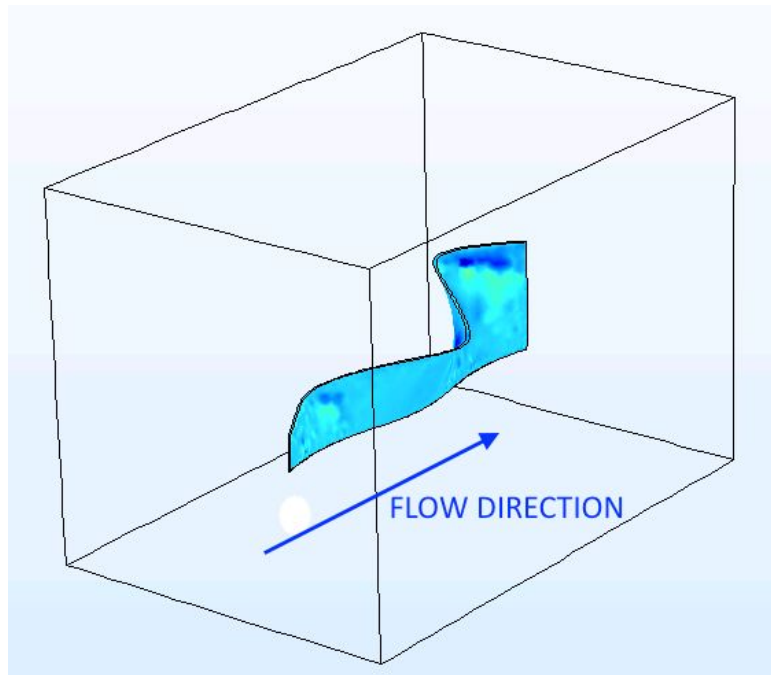


Figure 55: Pressure distribution along Test Fin 2 surface

Finally, Test Fin 3 has a fin height of three inches at the leading end, again, increasing linearly, such that the middle of the fin has a height of 7.5 inches and the trailing end has a height of 12 inches (Figure 56).

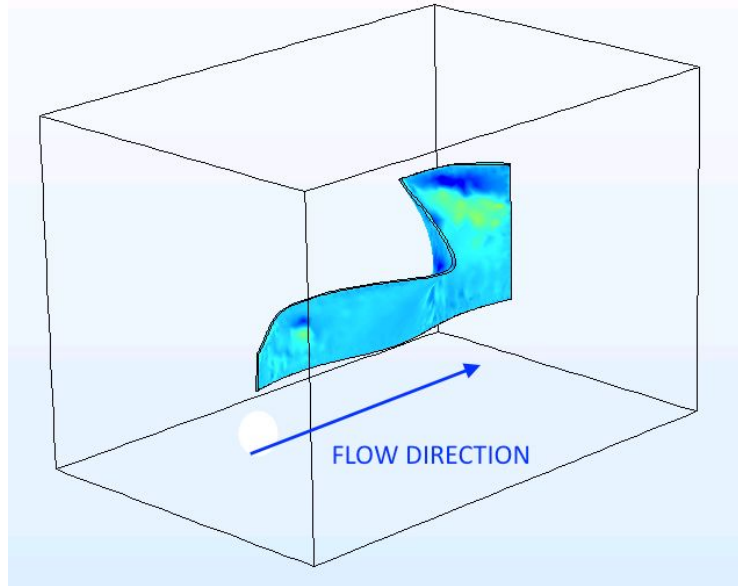


Figure 56: Pressure distribution along Test Fin 3 surface

Both sides of each fin were split into sections on which the pressure distribution of each section was generalized and represented by an average. Comparing the average pressure between sections provides the opportunity to quantify the net pressure along the fin. This information is used to determine which fin shape will produce the highest torque necessary to produce the highest power output.

As shown in Figure 57, the surface of the control fin was split into 36 different sections, 18 sections for each side of the fin surface. Each fin has three distinct cusps. Each cusp was split in half vertically being distinguished by “region.” The fin was then split into three horizontal regions designated as “top,” “middle,” and “bottom,” and six vertical regions designated as “1,” “2,” “3,” “4,” “5,” and “6.” Using the color coded scale outputted as part of the simulation results shown in Figure 57, each section was associated with an average pressure reading.

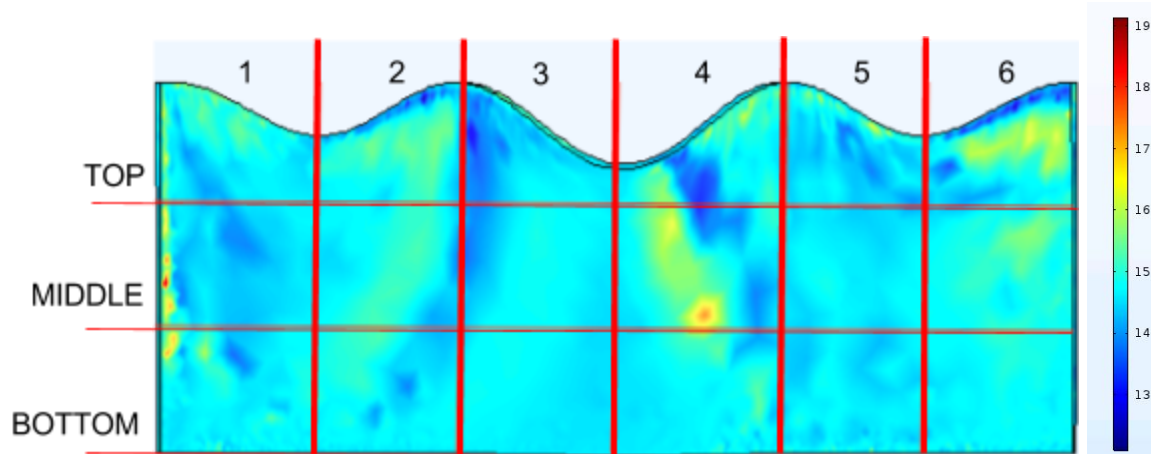


Figure 57: Grid layout of fin regions and pressure distribution scale (psi)

These readings were determined by the analyzer’s visual interpretation, matching the colors presented on the fin surface with the pressure as defined by the color-coded scale. Figures 58 through 61 show the sectional layout on both sides of a selection of fin models used in the simulation. Each visual interpretation of the pressure distribution for all sections on both sides of each fin was recorded in Table 2 through Table 5. These tables quantify the average pressure on each section of the fin along with the corresponding force and torque. The “Total Torque” row indicates the total torque on each region of the fin along both the left and right side respectively. The maximum total torque between the left and right side for each section is highlighted in green, yellow, or red. A green highlight indicates that the maximum total torque for that region corresponds with the natural propagation of the sine wave, while a yellow highlight indicates a zero net torque. Finally a red highlight indicates the maximum total torque for that region opposes the natural propagation of the sine wave

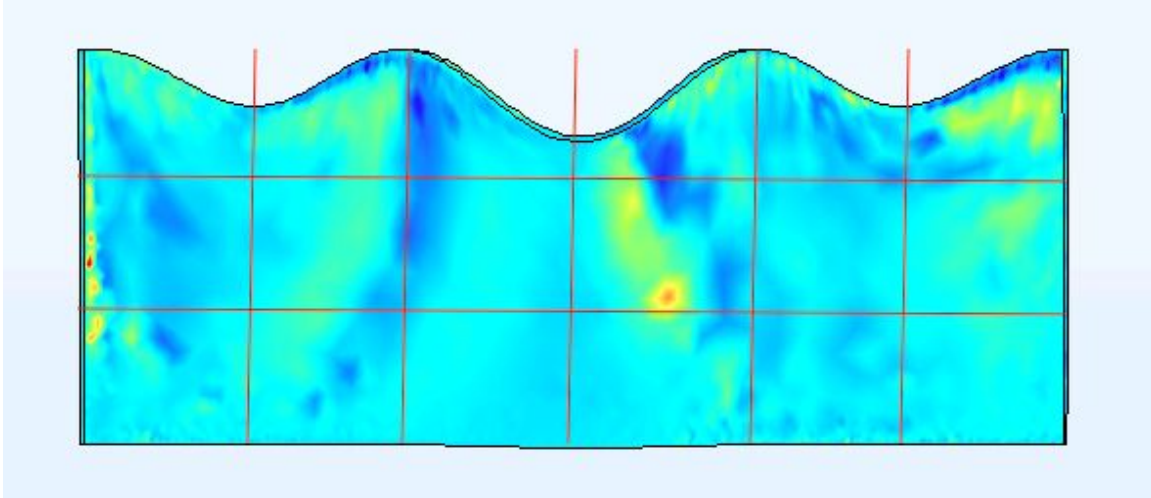


Figure 58: Left side of Control Fin

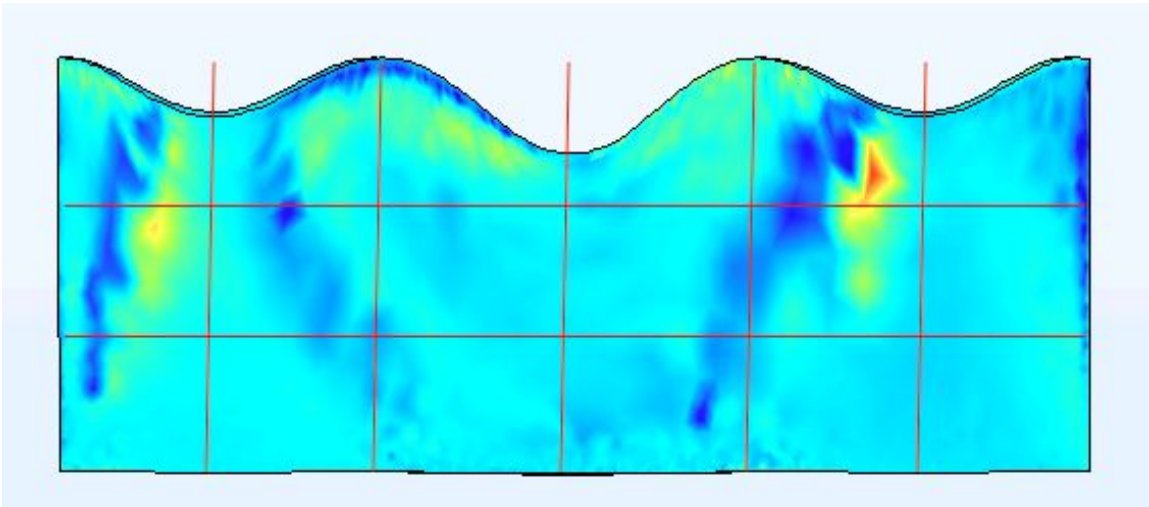


Figure 59: Right side of Control Fin

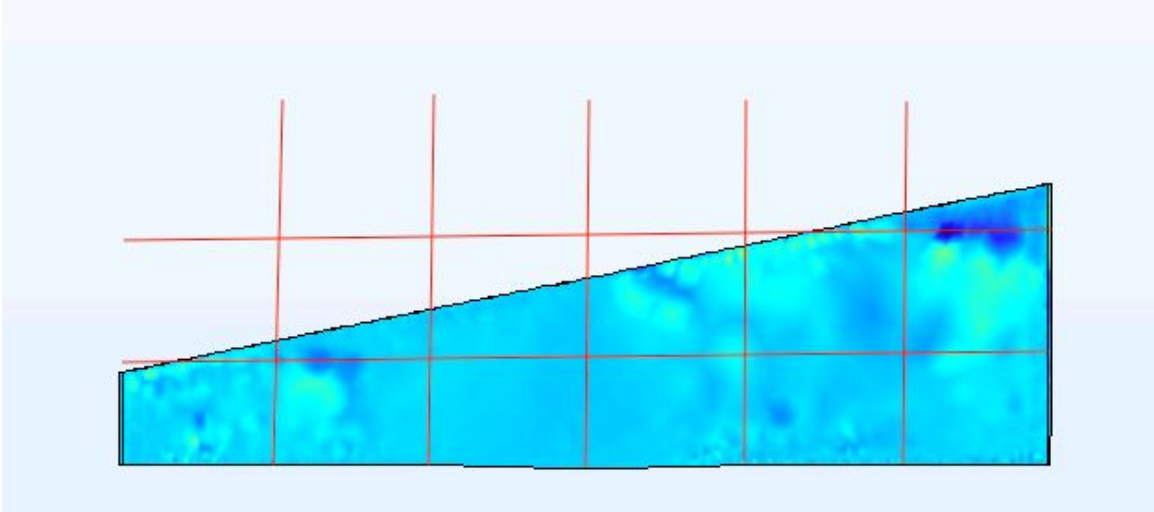


Figure 60: Left side of Test Fin 2

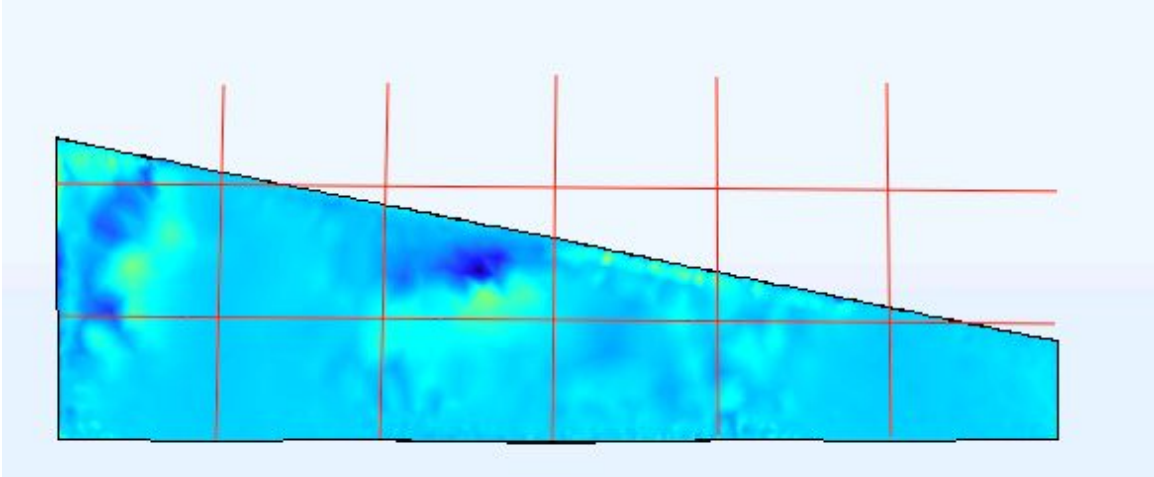


Figure 61: Right side of Test Fin 2

Table 2: Original Fin results and analysis based on COMSOL Simulation

		Original							
		Left Pressure (psi)	Left Force (lbf)	Left Torque (ft*lbf)	Right Pressure (psi)	Right Force (lbf)	Right Torque (ft*lbf)	Centroid Distance from Pivot (ft)	
Region	1	TOP	14.85	297.00	247.50	14.30	286.00	238.33	0.83
	MIDDLE	15.65	313.00	156.50	14.45	289.00	144.50	0.50	
	BOTTOM	14.90	298.00	49.67	14.75	295.00	49.17	0.17	
	Total Torque			453.67			432.00		
	2	TOP	15.10	302.00	251.67	15.40	308.00	256.67	0.83
	MIDDLE	15.10	302.00	151.00	14.65	293.00	146.50	0.50	
	BOTTOM	15.20	304.00	50.67	14.50	290.00	48.33	0.17	
	Total torque			453.33			451.50		
	3	TOP	14.50	290.00	241.67	16.15	323.00	269.17	0.83
	MIDDLE	14.75	295.00	147.50	14.50	290.00	145.00	0.50	
	BOTTOM	14.75	295.00	49.17	14.30	286.00	47.67	0.17	
	Total Torque			438.33			461.83		
	4	TOP	15.00	300.00	250.00	14.95	299.00	249.17	0.83
	MIDDLE	15.50	310.00	155.00	14.70	294.00	147.00	0.50	
	BOTTOM	15.00	300.00	50.00	14.50	290.00	48.33	0.17	
	Total torque			455.00			444.50		
	5	TOP	14.95	299.00	249.17	14.90	298.00	248.33	0.83
	MIDDLE	14.65	293.00	146.50	14.45	289.00	144.50	0.50	
	BOTTOM	14.80	296.00	49.33	14.80	296.00	49.33	0.17	
	Total Torque			445.00			442.17		
	6	TOP	15.10	302.00	251.67	14.90	298.00	248.33	0.83
	MIDDLE	15.35	307.00	153.50	15.30	306.00	153.00	0.50	
	BOTTOM	14.80	296.00	49.33	14.75	295.00	49.17	0.17	
	Total Torque			454.50			450.50		

Table 3: Test Fin 1 Results and Analysis Based on COMSOL Simulation

		Test Fin 1							
		Left Pressure (psi)	Left Force (lbf)	Left Torque (ft*lbf)	Right Pressure (psi)	Right Force (lbf)	Right Torque (ft*lbf)	Centroid Distance from Pivot (ft)	
Region	1	TOP	-			-			0.83
	MIDDLE	-			-				0.50
	BOTTOM	15.05	301.00	50.17	14.70	294.00	49.00	0.17	
	Total Torque			50.17			49.00		
	2	TOP	-			-			0.83
	MIDDLE	-			-				0.50
	BOTTOM	14.60	292.00	48.67	14.65	293.00	48.83	0.17	
	Total torque			48.67			48.83		
	3	TOP	-			-			0.83
	MIDDLE	-			-				0.50
	BOTTOM	14.40	288.00	48.00	14.50	290.00	48.33	0.17	
	Total Torque			48.00			48.33		
	4	TOP	-			-			0.83
	MIDDLE	-			-				0.50
	BOTTOM	14.50	290.00	48.33	14.50	290.00	48.33	0.17	
	Total torque			48.33			48.33		
	5	TOP	-			-			0.50
	MIDDLE	-			-				0.17
	BOTTOM	14.55	291.00	48.50	14.50	290.00	48.33	0.17	
	Total Torque			48.50			48.33		
	6	TOP	-			-			0.83
	MIDDLE	-			-				0.50
	BOTTOM	14.30	286.00	47.67	14.40	288.00	48.00	0.17	
	Total Torque			47.67			48.00		

Table 4: Test Fin 2 Results and Analysis Based on COMSOL Simulation

		Test Fin 2							
		Left Pressure (psi)	Left Force (lbf)	Left Torque (ft*lbf)	Right Pressure (psi)	Right Force (lbf)	Right Torque (ft*lbf)	Centroid Distance from Pivot (ft)	
Region	1	TOP	-			-		0.83	
	MIDDLE	-			-			0.50	
	BOTTOM	14.75	295.00	49.17	14.75	295.00	49.17	0.17	
	Total Torque			49.17			49.17		
	2	TOP	-			-		0.83	
	MIDDLE	14.40	72.00	36.00	14.85	74.25	37.13	0.50	
	BOTTOM	15.10	302.00	50.33	14.75	295.00	49.17	0.17	
	Total torque			86.33			86.29		
	3	TOP	-			-		0.83	
	MIDDLE	14.70	147.00	73.50	15.10	151.00	75.50	0.50	
	BOTTOM	14.70	294.00	49.00	14.60	292.00	48.67	0.17	
	Total Torque			122.50			124.17		
	4	TOP	-			-		0.83	
	MIDDLE	14.55	218.25	109.13	14.85	222.75	111.38	0.50	
	BOTTOM	14.63	292.50	48.75	14.75	295.00	49.17	0.17	
	Total torque			157.88			160.54		
	5	TOP	-			-		0.83	
	MIDDLE	14.80	296.00	148.00	14.60	292.00	146.00	0.50	
	BOTTOM	14.60	292.00	48.67	14.60	292.00	48.67	0.17	
	Total Torque			196.67			194.67		
	6	TOP	13.65	68.25	56.88	14.95	74.75	62.29	0.83
	MIDDLE	15.95	319.00	159.50	15.00	300.00	150.00	0.50	
	BOTTOM	14.95	299.00	49.83	14.90	298.00	49.67	0.17	
	Total Torque			266.21			261.96		

Table 5: Test Fin 3 Results and Analysis Based on COMSOL Simulation

		Test Fin 3							
		Left Pressure (psi)	Left Force (lbf)	Left Torque (ft*lbf)	Right Pressure (psi)	Right Force (lbf)	Right Torque (ft*lbf)	Centroid Distance from Pivot (ft)	
Region	1	TOP	-			-		0.83	
	MIDDLE	14.85	37.13	18.56	14.70	37.63	18.82	0.50	
	BOTTOM	14.85	297.00	49.50	14.70	294.00	49.00	0.17	
	Total Torque			68.06			67.82		
	2	TOP	-			-		0.83	
	MIDDLE	14.10	141.00	70.50	15.10	151.00	75.50	0.50	
	BOTTOM	15.60	312.00	52.00	14.80	296.00	49.33	0.17	
	Total torque			122.50			124.83		
	3	TOP	-			-		0.83	
	MIDDLE	14.75	258.13	129.06	14.70	257.25	128.63	0.50	
	BOTTOM	14.75	295.00	49.17	14.60	292.00	48.67	0.17	
	Total Torque			178.23			177.29		
	4	TOP	15.40	77.00	64.17	14.10	70.50	58.75	0.83
	MIDDLE	14.75	295.00	147.50	14.45	289.00	144.50	0.50	
	BOTTOM	14.70	294.00	49.00	14.75	295.00	49.17	0.17	
	Total torque			260.67			252.42		
	5	TOP	15.10	151.00	125.83	14.30	143.00	119.17	0.83
	MIDDLE	14.35	287.00	143.50	14.75	295.00	147.50	0.50	
	BOTTOM	14.60	292.00	48.67	14.75	295.00	49.17	0.17	
	Total Torque			318.00			315.83		
	6	TOP	14.50	217.50	181.25	15.90	238.50	198.75	0.83
	MIDDLE	15.30	306.00	153.00	15.90	318.00	159.00	0.50	
	BOTTOM	14.80	296.00	49.33	14.65	293.00	48.83	0.17	
	Total Torque			383.58			406.58		

As seen in the figures, and as indicated in the tables, in some fin designs the surface layout did not cover the entire 18 sections per side. To determine the average force applied to the fin per region, the area of each region corresponding to the fin surface was multiplied by the average pressure for each section. In some cases where the fin surface did not fully occupy a region, the corresponding fraction of that regional area was used when determining the force. Finally, the average force was multiplied by the distance from the centroid of each corresponding region to the base of the fin. This calculation determined the torque applied by the fin to the mechanical components of the apparatus. Comparing these torques led the team to make a decision regarding which fin shape would produce the highest power output.

An analysis of the tables suggests Test Fin 2 will have the greatest capability to produce the most power of any of the fin shape models. The idea to vary the overall shape of the fin was conceived after the original physical testing of the hybrid fin and a computer fluid dynamic simulation of the control fin were completed. While watching the physical fin during testing, it was apparent that vortices were developing around each cusp and impinging upon the motion of the fin between cusps. After running the fluid dynamic simulation on the control fin model, the pressure distribution along the surface indicated a relatively high-pressure region on the backside of the second cusp in region 4. The net pressure in this region opposes the continual motion of the propagating sine wave, therefore reducing the fin's efficiency and power harvesting capability. The team believed the severity of the vortex was due to the relatively sudden onset of fluid dispersion when coming into contact with the fin. The fluid flow is steady and unidirectional upon entering the simulation region. When the fluid comes into contact with the fin surface, the vast change in velocity causes vortices to form, flowing around the cusp, and

impacting the fin surface on the backside of the cusp. The impact creates a net pressure contradicting the natural motion of the propagating sine wave. The impact was most significant between regions 3 and 4 and between regions 4 and 5.

The team attempted to reduce the impact of fluid vortices inhibiting the natural propagation of the fin by reducing the height of the leading edge and gradually increasing the height along the length of the fin. The data shows that the control fin experiences a net pressure corresponding to the natural sine wave movement in regions 2 and 6, while the fin experiences a net pressure contradicting the natural propagation of a sine wave in regions 1, 3, 4, and 5. Test Fin 1 exhibited a neutral net pressure in region 4, while exhibiting a net surface pressure opposing natural sine wave propagation in regions 1, 2, 3, 5, and 6. Test Fin 2 exhibited a net pressure corresponding with natural sine wave propagation in regions 2, 4, and 6, with opposing net pressure distributions in region 3 and 5, and one neutral net pressure in region 1. Finally Test Fin 3 exhibits naturally corresponding net pressure in region 3, while all other regions exhibit opposing pressure distributions.

To confirm the results of the pressure distribution impact on fin performance, the net torque for each section was analyzed. The resulting net torques coincide with the results of the net pressure distributions along the fin. All results are quantified in Table 2 through Table 5. For these reasons the team believes that the varying height of Test Fin 2 provides the best shape and will result in the greatest power output and efficiency. In the future, flow tank testing can be used to verify these theoretical results.

9.9 Finite Element Analysis (FEA) Results

9.9.1 Mast Deflection

FEA was able to predict the deformations and stresses experienced by the prototype fin assembly during testing. Since the water only covered approximately two-thirds of the fin, the team assumed that most of the force was acting near the end of the mast. Equation 12 in Figure 62 describes a simple model of this phenomena and was used to calculate the deflections of each mast. COMSOL was used to generate the cross sectional surface pressure distribution of the fin (see Section 9.8). The surface pressure across the fin was taken at 5 points from position 1 at the bottom of the mast to position 5 at the top (Figure 63) of each of the 5 masts at positions of 0° , 60° , 120° , 180° , 240° (Figure 64). The net surface pressures were determined by taking the average color in the numbered regions shown in Figure 63 and matching that color to the corresponding COMSOL pressure scale. An example of the surface pressure calculation for mast 60 can be seen in Table 6. Taking the surface pressure calculated and multiplying that with the perpendicular area of the fin (Figure 65) gives the force acting on that area of the fin. This same procedure is repeated at each cross sectional view of all the masts along the sine wave of the fin. All cross sectional views used in the remaining mast deflection calculations are located in Appendix F. Additionally, with the data generated by COMSOL for a flow speed of 2 m/s (see Section 9.8), the perpendicular deflections of the masts and the deflections of the main shaft were calculated by hand and using SolidWorks.

The parallel deflections of the mast were calculated by first finding the dynamic pressure, the parallel area, and the force of the dynamic pressure acting on that area. To find the dynamic

pressure, the equation, $q = 1/2 * \rho * v^2$, was used (ρ is the density of water, v is the flow of the water, and q is the dynamic pressure). This pressure was multiplied by the parallel area (Figure 66) to calculate the parallel force. This force P is the load used in equation 12 to calculate the parallel deflection. Finally, the parallel deflections and the perpendicular deflections combined gave a total deflection of each mast by using the Pythagorean theorem. To ensure accuracy SolidWorks was used to calculate the total deflection as well in each mast and the main shaft.

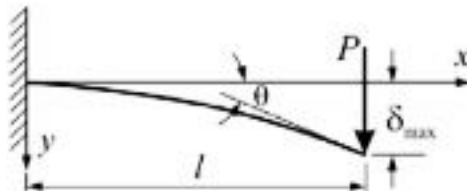


Figure 62: Cantilever beam deflection [41]

$$v_{max} = \frac{P * L^3}{3E * I} \text{ [Equation 12]}$$

$$v_{max} = \text{Deflection (m)}$$

$$P = \text{Load (N)}$$

$$E = \text{Young's Modulus (Pa)}$$

$$I = \text{Cross section area moment of inertia (m}^4\text{)}$$

$$L = \text{length (m)}$$

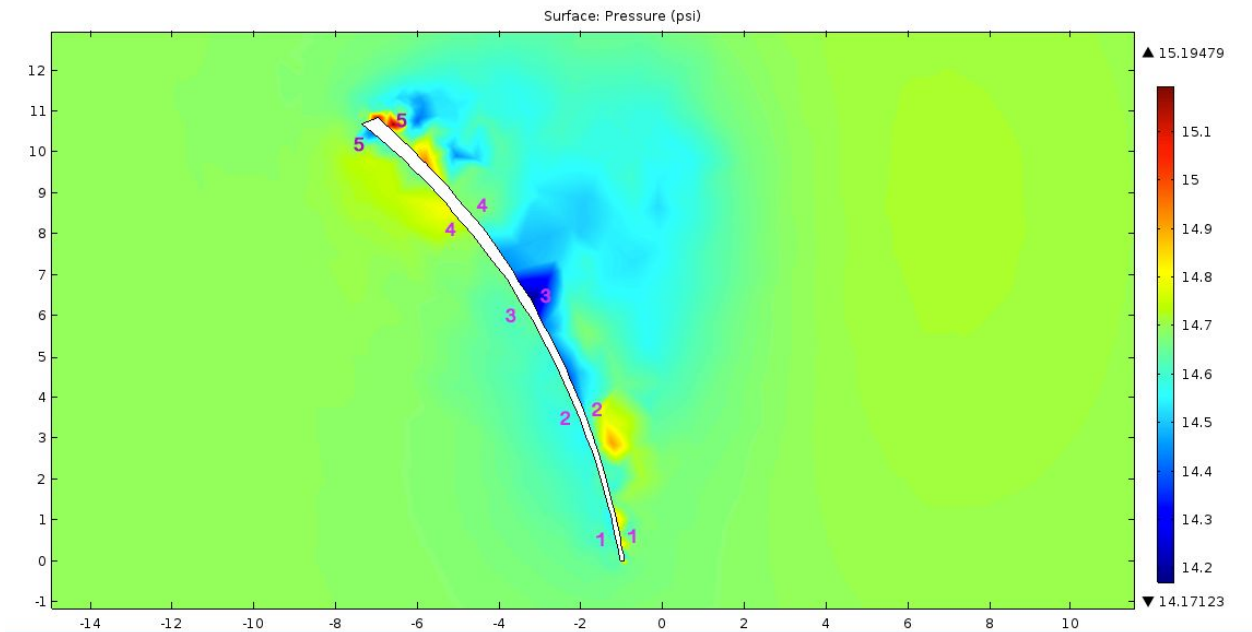


Figure 63: Cross sectional area of fin with pressure changes from fluid flow (Section 9.8)

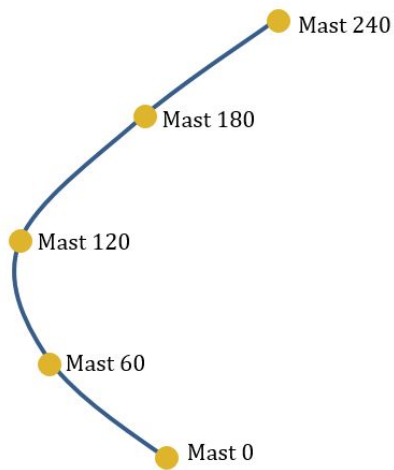


Figure 64: Mast positions

Table 6: Surface pressure calculation for Mast 60

Angle (degrees)	60		Units
Position	Left	Right	
1	14.5	14.8	psi
2	14.65	14.5	psi
3	14.65	14.3	psi
4	14.8	14.7	psi
5	14.75	15	psi
Average (psi)	14.67	14.66	psi
Net Pressure	0.01 (left side)		psi
	68.947 (left side)		Pa

Table 7: Mast information for calculation

Rod Information	CES Edu Pack: CuZn36, C26800, hard (basis brass)
Length (m)	0.305
Radius (m)	0.003175
Diameter (m)	0.00635
Yield Strength (Pa)	1.75E+11
Young's Modulus (Pa)	1.00E+11
Surface Area of Rod (m ²)	0.00608
Moment of Inertia (m ⁴)	7.98E-11

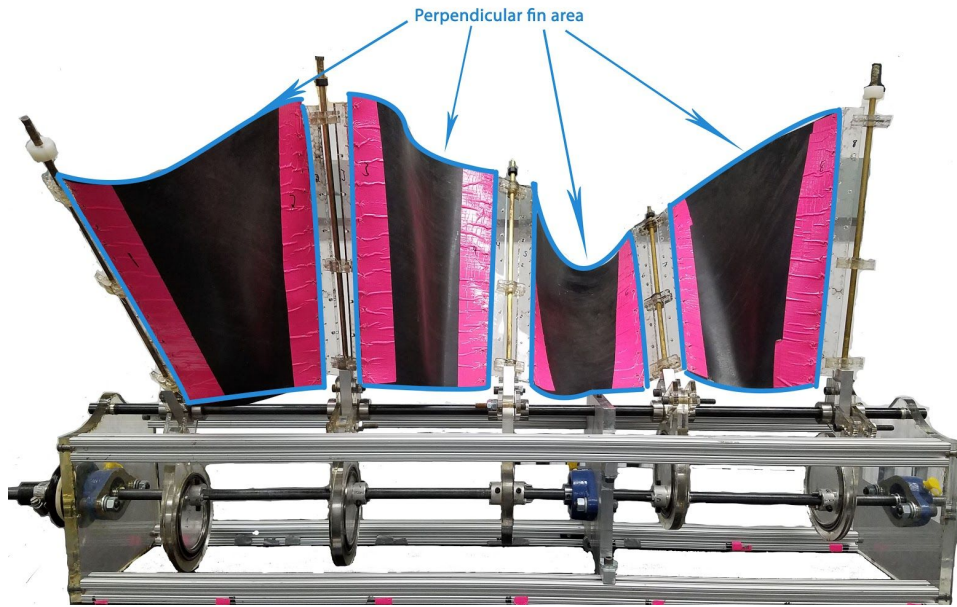


Figure 65: Perpendicular area of fin

Table 8: Mast deflection calculation in x direction

Deflection of Masts perpendicular to Water Flow - x direction					
Mast	0	60	120	180	240
Total Pressure (Pa)	3309.456	68.947	551.576	2757.88	689.47
Surface Area of Mast (m²)	0.00405	0.00405	0.00405	0.00405	0.00405
Force on Mast (N)	13.42	0.28	2.24	11.18	2.79
Total Deflection of Mast in x direction (cm)	1.59	0.03	0.26	1.32	0.33

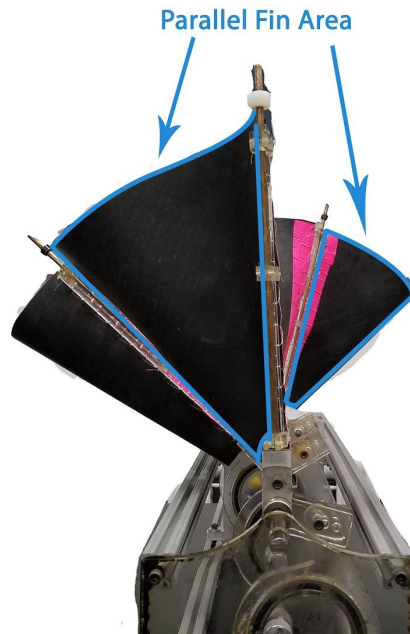


Figure 66: Parallel area of fin

Table 9: Mast deflection calculation in y direction

Deflection of Masts Parallel to Water Flow - y direction				
Masts	0 and 60	60 and 120	120 and 180	180 and 240
Total Pressure (Pa)	2000	2000	2000	2000
Sector Fin Area perpendicular to current (m²)	0.02452	0.00323	0.0219	0.0258
Force on Section(N)	49.03	6.452	43.87	51.61
Total deflection on each mast (cm)	5.80	0.763	5.19	6.11

The force values, determined from the net pressures acting on each mast's position along the sine wave as shown in Figure 64, were used in Equation 12 to calculate the deflection in the x-direction and the y-direction in the masts, presented in Table 8 and Table 9. These force components in the x and y direction are used to determine the total deflection per mast. If one mast was supporting two parallel areas of the fin, the deflection caused by each parallel area was added together to determine the total deflection of that mast, presented in Table 10 and shown in Figure 67. For the fin orientation shown in Figure 64, all the masts, except mast 180, have approximately the same net deflection. Mast 180 has twice the net deflection of the other masts. The remaining masts may have similar net deflections due to the forces acting at their position along the sine wave and their angle from the center of the apparatus, as shown in Figure 68.

The greater a mast's angle from the center of the apparatus, the greater its deflection perpendicular to the water flow. Conversely, the smaller the mast's angle from the center of the apparatus, the greater the deflection parallel to the water flow. To double check this finding, the masts would have to be shifted to another position along the sine wave and their deflections recalculated.

Table 10: Total deflection of masts in fin

Deflection per Mast		
Mast 0	6.01 cm	2.37 in
Mast 60	6.56 cm	2.58 in
Mast 120	5.96 cm	2.35 in
Mast 180	11.37 cm	4.48 in
Mast 240	6.11 cm	2.41 in

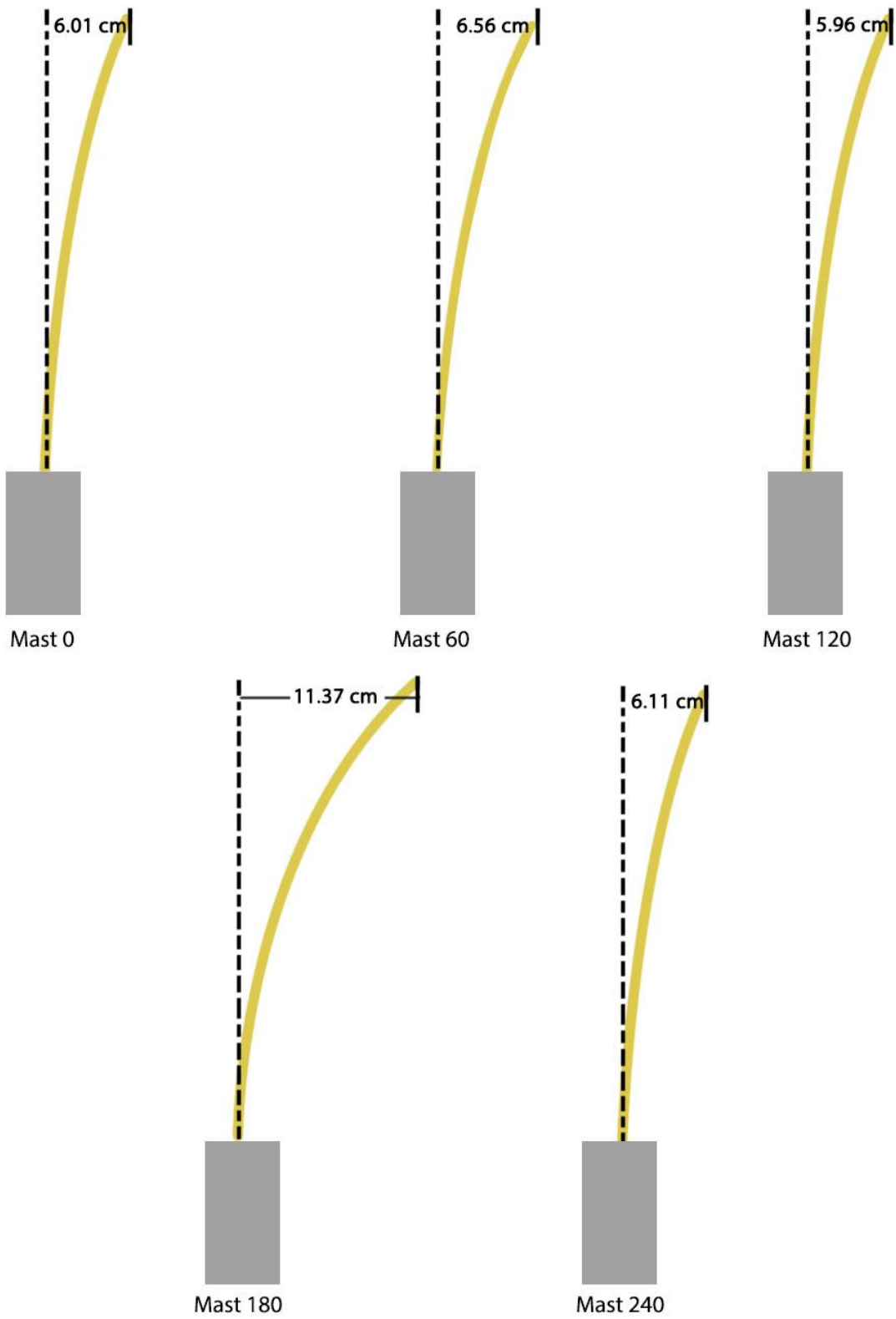


Figure 67: Deflection per mast

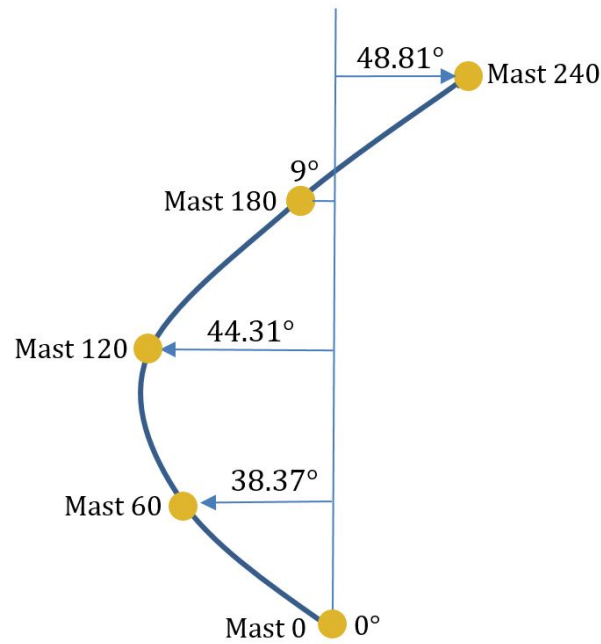


Figure 68: Mast position and angle from center of apparatus

To double check the hand calculations described above, a static study was conducted in SolidWorks with the force values calculated with COMSOL data. The deflections computed in SolidWorks were comparable to hand calculations, but were generally smaller than the results predicted by the procedure described above. The range of deflections calculated were between 2.55 cm and 4.81 cm.

As the flow was increased during testing, the team observed that the deflection of the fin's masts increased as well. In fact, during the final test that the team conducted when the flow speed reached 1200 (1.47 m/s), one of the masts snapped in the flow direction. The rod broke in the flow direction suggesting that the drag force on the fin is more pronounced than the net pressure forces acting on its sides. The team has two theories for why the rod broke. First, the

team believes that the threads added to the ends of the masts acted as stress concentrators (failure occurred at the base of the rod where the threads are located). Second, the fin was motionless in fast moving water when the mast broke (the team was conducting a peak torque test). The team believes that when the fin is not allowed to move in the water the rods must support all of the water's force instead of transferring it to the device's output shaft. The former of these theories was studied further through the use of SolidWorks' stress analysis function.

SolidWorks was used to compare stresses acting on masts affixed to blocks (rocker cores) with no threads (as previously calculated) and masts with exposed threads (a more realistic representation). The forces in the parallel and perpendicular direction that caused the greatest deflection were used in the simulations seen in Figures 69 through 71 below. SolidWorks justifies the above claim that the threads at the base of the masts act as stress concentrators. Since the fin oscillates, the masts only experience this force for a short duration and are generally able to withstand the applied stress, but may, as seen in testing, fatigue and fail over time.

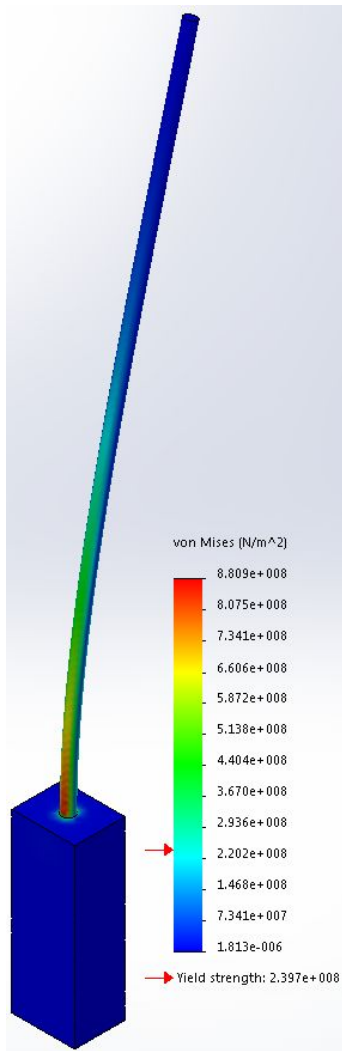


Figure 69: Mast stress with no threads

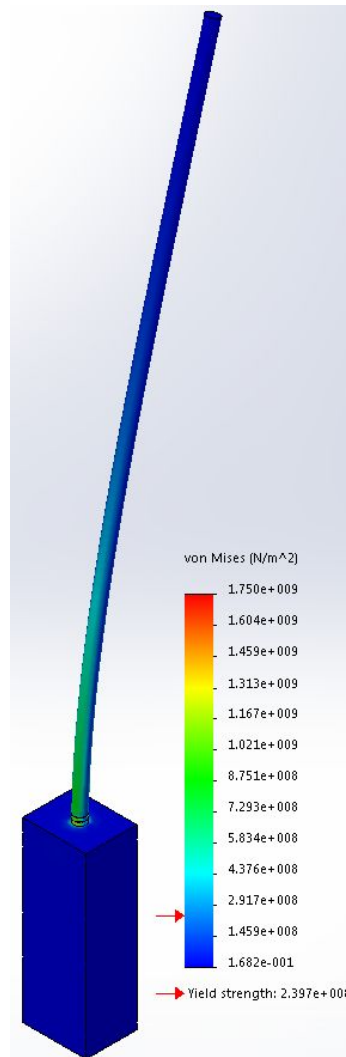


Figure 70: Mast stress with threads

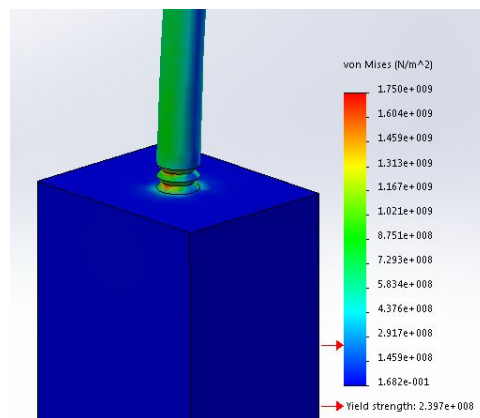


Figure 71: Detailed view of stress concentration at threads

9.9.2 Analysis of Scaled Device

In order to test how the fin and masts would perform at a scale more applicable to grid-level power output, the team decided to scale the fin by 500% to represent a potential real world device. Taking these new fin areas into account, calculations were done following the same procedure as above. As shown in Table 11 below, the deflections are noticeably higher; to account for this significant change, the diameter of the masts was increased to 1.5” and then again to 1.75” to study the effect of mast diameter on mast deflection with the scaled fin. From these calculations it can be concluded that if brass were still used as a material, the masts would need a minimum diameter of 1.75” to handle the exerted forces and have minimal deflection.

Table 11: Scaled fin mast deflections

500% Masts Deflection Total	500% Fin with 1.25” brass masts		500% Fin with 1.5” brass masts		500% Fin with 1.75” brass masts	
Mast 0	7.97 cm	3.14 in	4.61 cm	1.81 in	2.90 cm	1.14 in
Mast 60	0.89 cm	0.35 in	0.43 cm	0.17 in	0.24 cm	0.09 in
Mast 120	1.54 cm	0.61 in	0.86 cm	0.34 in	0.52 cm	0.21 in
Mast 180	6.78 cm	2.67 in	3.90 cm	1.53 in	2.44 cm	0.96 in
Mast 240	1.84 cm	0.72 in	1.03 cm	0.41 in	0.64 cm	0.25 in

9.9.3 Main Shaft Deflection

The deflection in the main shaft was determined by using the calculated forces exerted by the flowing water on the fin and assuming a total transfer of that force through the rockers and cams and into the shaft. Equation 13 was used to calculate the force exerted by the fin onto the rocker, which was then transferred from the rocker to the cam and into the shaft. The force of the water (F_W) and the force of the rocker (F_R) act at measured distances (D_1) and (D_2), as shown in Figure 72. Solving for (F_R) in Equation 13 produces the force acting perpendicular to the rocker arm, shown in Figure 72 and tabulated in Table 12.

$$F_W * D_1 = F_R * D_2 \quad [Equation 13]$$

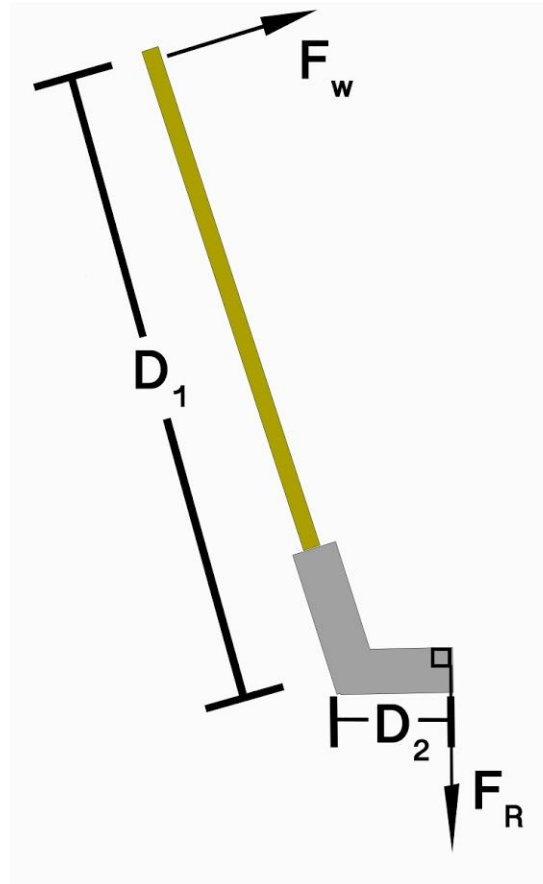


Figure 72: Rocker force calculation diagram

Table 12: Force on rocker calculations

Force on Rocker - Normal MQP Fin			
Cam	Force(w) on Mast (N)	Distance (m)	Force by Rocker (N)
5	13.415	D1 = 0.3556	136.593
4	0.279		2.846
3	2.236	D2 = 0.034925	22.766
2	11.18		113.828
1	2.795		28.457

In order to determine the moment of each cam acting on the main shaft, the team needed to find the force applied to the shaft by each rocker, as well as the corresponding cam's distance from the end of the device. The forces transferred to the main shaft by the rockers are decomposed into their x- and y-components using trigonometry as shown in Figure 73 below. Using the measured distance from each cam to the rod's supports as well as the x- and y-components of the force applied to the main shaft by the cam's corresponding rocker, the total moment in both the x and y directions were calculated. Once the moments and forces on the main shaft were calculated, the deflection at each cam could be calculated using Equation 14. To find the total deflection of the main shaft, the team added each deflection calculated at each cam.

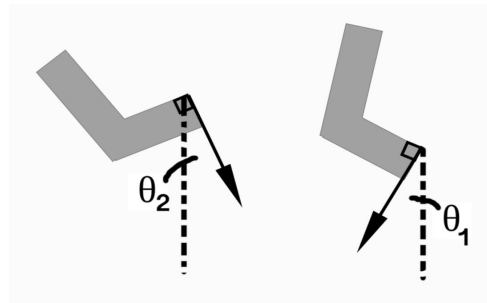


Figure 73: Angle diagram calculations

After finding the net x and y forces and net moments, the deflection in the shaft can be calculated by finding the net force from the x and y forces and net moments, then using these results in Equation 14 represented by Figure 74. This calculation resulted in nominal forces and moments exerted on the shaft (Table 13 and Table 14). To prevent deflection an appropriate material and diameter must be selected to handle the expected forces and moments.

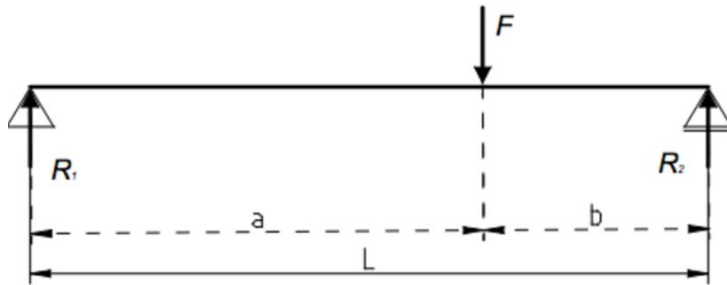


Figure 74: Eccentric load on supported beam equation diagram [42]

$$\delta_{Max} = F a^2 b^2 / (3 E I L) \text{ [Equation 14]}$$

Table 13: x and y components of rocker forces

Angle (degrees)	Position	Force x-component (N)	Force y-component (N)
30	2	68.297	118.293
15	2	0.737	2.749
38	1	-14.016	-17.939
60	1	-98.578	-56.914
44	1	-19.768	-20.470
	Net Forces (N)	-63.328	25.718

Table 14: Moments about the x and y axes

Cam	Distance from Front Plate (m)	Moment about x-axis (N*m)	Moment about the y-axis (N*m)
5	0.08255	5.638	9.765
4	0.2667	0.196	0.733
3	0.34925	-4.895	-6.265
2	0.64135	-63.223	-36.502
1	0.828675	-16.381	-16.963
	Net Moment (N*m)	-78.665	-49.232

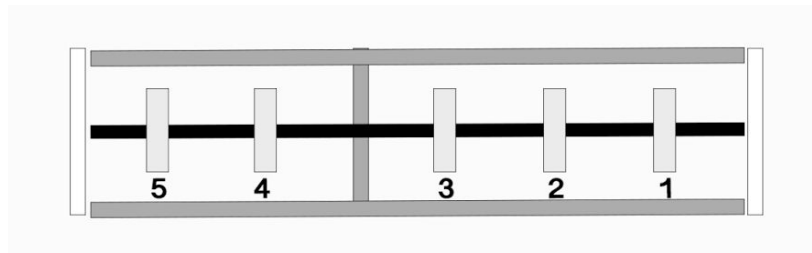


Figure 75: Cam placement on main shaft

Table 15: Main shaft deflection

Cam	Distance a (m)	Distance b (m)	x-deflection (m)	y-deflection (m)
5	0.08255	0.83185	0.000460	0.00080
4	0.2667	0.6477	3.14E-05	0.000117
3	0.34925	0.56515	-0.00078	-0.001
2	0.64135	0.27305	-0.00432	-0.00249
1	0.828675	0.085725	-0.000142	-0.000147
		Net Deflection (m)	-0.00475	-0.00272

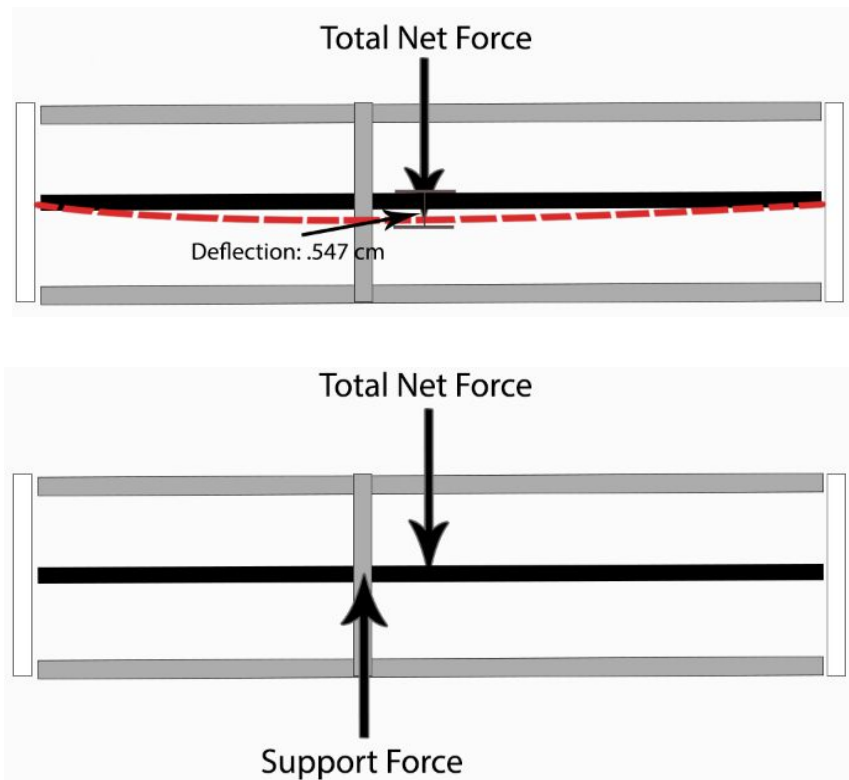


Figure 76: Main shaft deflection diagram (with and without support)

To calculate the deflection in the shaft, the deflection from each force acting on its respective cam was calculated in the x and y direction. To simplify the calculation the main shaft support between cams 3 and 4 (Figure 75) was ignored to determine if the support was necessary to reduce deflection in the main shaft. The deflection in the main shaft was calculated using the information from Table 15 to be 0.547 cm without the support between cams 3 and 4 and shown in Figure 76. This deflection is assuming that the total amount of force is transferred from the rod into the rocker and into the shaft through the cams. Although the deflection in the main shaft is minimal, it could still affect the fin's operation. This finding shows that the support is still necessary to reduce the deflection that occurs on the shaft.

10. Conclusion and Recommendations

After concluding a quantitative analysis of the fin generator, the team was able to draw several conclusions about the current state of the technology and recommend a path forward for future work. Perhaps the most overarching result of the team's testing is that the device, at this size and with the level of fin submersion, outputs too little power and operates at too low of an efficiency to be feasible. However, based on the stress analyses the team conducted, it is believed that the device can be safely scaled to output more power; completing this task may prove to be a fruitful endeavor for future research teams. To build an effective larger prototype, the current team suggests that the manufacturing process be optimized; this could include switching from a camshaft to a crankshaft, as purchasing large bearings for eccentric cams may be prohibitively expensive. Also, the team strongly recommends testing the fin in a flow tank where full submersion, without significant boundary layer effects or standing waves, can be consistently maintained; if such a location cannot be found and WPI MQP teams are limited to the facilities available on campus, future teams may need to resort to using the pool in WPI's Sports and Recreation Center as a tow tank.

Still, the current prototype performed well enough for the team to conclude that more flexible, in this case thinner, fins are more effective than more rigid ones. They calculated the fin's power output for an array of flow velocities for each fin; from this, the team was able to derive a cumulative efficiency for each of the three fins tested. The power vs. torque plots shown above illustrate strong linear correlation between the peak powers for each velocity. Furthermore, certain identical "critical points" exist on all of the efficiency plots produced.

These results allow the team to generalize the effect of fin rigidity on the entire device's performance and say that more flexible fins are superior to more rigid ones.

The team calculated that the highest power output was approximately 3 W and the highest efficiency was approximately 4.5%. Again, these results both correspond to the acrylic-hybrid fin as it was the most flexible and thus produced the best results. However, both of these results are too low for industrial power generation. While the team could argue that the fin was not fully submerged in the WPI's rowing tank, and the power and efficiency could perhaps scale by a factor of two or three to 6 to 9 W and 10 to 15% respectively, this is still well below industrial power generation levels. Drastic enhancements to the device, perhaps most readily by increasing its size, would be needed to conclude whether fin-based power generation is feasible. In order to handle the stresses exerted by a larger scale fin, the team recommends the use of thicker rods to prevent the device from failing. This prediction is based off the team's stress calculations for the small fin in 2 m/s water which showed significant deflection in the masts for even just the small prototype discussed in this report.

Additionally, fin shape has a profound impact on the force exerted on each region of the fin. Computational fluid dynamic simulations involving different fin shapes proved a variable fin height was most effective in correlating the frequency of wave propagation to the forces of the water. The net forces exerted on Test Fin 2 (3" leading edge, 6" center, 9" trailing edge) directed the oscillation of each mast with the best correspondence to the natural propagation of the sine wave; physical testing is required to verify this result. Fin shape does affect device performance and remains to be optimized. Overall, the team recommends continuing CFD analysis both with single phase laminar flow and fluid structure interaction models because it

allows for many fin iterations to be analyzed relatively quickly.

Finally the team concluded that the kinematic relationship of the rocker/eccentric cam subassembly is very complex and lacks sufficient benefit, compared to a crankshaft, to continue use. However, further research into the transmission angle of the rocker and drive shaft subassembly may reveal the ability to increase overall efficiency. Further work may also include the involvement of a generator and analysis of the proper gear ratios to optimize power generation.

Overall the team believes that at small scales, the fin is too inefficient to be a viable means of power production. However, further analyses, both physical and computational, can be conducted to improve this device, and stress analyses show that, theoretically, it can be safely scaled to increase power output. The potential for future improvements, taken with the necessity of clean, reliable power generation, means that fin-based power generation is an idea worth pursuing.

11. References

- [1] USGS, "Hydroelectric Power Water Use", 2016 [Online]. Available
<http://water.usgs.gov/edu/wuhy.html>. Accessed: Oct. 14, 2016
- [2] "Ocean Wave Energy", *Bureau of Ocean Energy Management*, 2016. [Online]. Available:
<http://www.boem.gov/Ocean-Wave-Energy/>. [Accessed: 14- Sep- 2016].
- [3] "Wave & Tidal Energy Technology | Renewable Northwest", *Rnp.org*, 2016. [Online].
Available: <http://www.rnp.org/node/wave-tidal-energy-technology>. [Accessed: 14- Sep- 2016].
- [4] "EIA's energy in brief: What are the major sources and users of energy in the United States?," 2015. [Online]. Available: http://www.eia.gov/energy_in_brief/article/major_energy_sources_and_users.cfm. Accessed: Sep. 19, 2016.
- [5] "Biomass - energy explained, your guide to understanding energy - energy information administration," 2016. [Online]. Available:
http://www.eia.gov/energyexplained/index.cfm?page=biomass_home. Accessed: Sep. 19, 2016.
- [6] "Geothermal - energy explained, your guide to understanding energy - energy information administration," 2015. [Online]. Available:
http://www.eia.gov/energyexplained/index.cfm?page=geothermal_home. Accessed: Sep. 19, 2016.

- [7] Institute for Energy Research, "Hydroelectric," in *Institute for Energy Research*, Institute for Energy Research, 2016. [Online]. Available:
<http://instituteforenergyresearch.org/topics/encyclopedia/hydroelectric/>. Accessed: Sep. 17, 2016.
- [8] "Hydropower - energy explained, your guide to understanding energy - energy information administration," 2016. [Online]. Available:
http://www.eia.gov/energyexplained/index.cfm?page=hydropower_home. Accessed: Sep. 19, 2016.
- [9] D. Manney, "Breaking down the difference between AC and DC generators," in *Generators*, L&S Electric, 2015. [Online]. Available:
<http://www.lselectric.com/breaking-down-the-difference-between-ac-and-dc-generators/>. Accessed: Sep. 19, 2016.
- [10] "U.S. Energy information administration (EIA) - source," 2013. [Online]. Available:
<http://www.eia.gov/forecasts/capitalcost/>. Accessed: Sep. 19, 2016.
- [11] "How Hydroelectric Energy Works", *Union of Concerned Scientists*, 2016. [Online]. Available:
http://www.ucsusa.org/clean_energy/our-energy-choices/renewable-energy/how-hydroelectric-energy.html#.V9Vrn5MrKCQ. [Accessed: 14- Sep- 2016].
- [12] P. Castro and M. Huber, *Marine biology*. New York: McGraw-Hill Higher Education, 2007.

- [13] US Department of Energy Office of Energy Efficiency and Renewable Energy, "History of Hydropower," in *Energy.Gov*. [Online]. Available:
<http://energy.gov/eere/water/history-hydropower>. Accessed: Sep. 16, 2016.
- [14] J. W. Tester, E. M. Drake, M. J. Driscoll, M. W. Golay, and W. A. Peters, *Sustainable Energy: Choosing Among Options*, 2nd. Cambridge, MA: MIT Press, 2005.
- [15] European Marine Energy Centre, "Tidal Devices," in *The European Marine Energy Centre*, 2016. [Online]. Available:
<http://www.emec.org.uk/marine-energy/tidal-developers/>.
Accessed: Sep. 16, 2016.
- [16] Aqua-RET, "Download Images and Illustrations," in *Aqua-RET*, 2012. [Online]. Available:
http://www.aquaret.com/indexea3d.html?option=com_content&view=article&id=203&Itemid=344&lang=en. Accessed: Sep. 16, 2016.
- [17] Bluewater, "BlueTEC Philosophy," in *Bluewater*, 2016. [Online]. Available:
<http://www.bluewater.com/new-energy/bluetec-phil/>. Accessed: Sep. 16, 2016.
- [18] BlueEnergy, "Vertical Axis Hydro Turbine," in *Blue Energy*. [Online]. Available:
http://www.bluenergy.com/technology_method_vaht.html. Accessed: Sep. 16, 2016.
- [19] BioPower Systems, "BioSTREAM," in *BioSTREAM*, 2013. [Online]. Available:
<http://www.biopowersystems.com/biostream.html>. Accessed: Sep. 16, 2016.

- [20] Tech-FAQ, "The Venturi Effect," in *Tech-FAQ*, 2015. [Online]. Available:
<http://www.tech-faq.com/venturi-effect.html>. Accessed: Sep. 16, 2016.
- [21] S. Moon, "Technology: Open-Centre Turbine," in *OpenHydro*, 2015. [Online]. Available:
<http://www.openhydro.com/techOCT.html>. Accessed: Sep. 16, 2016.
- [22] Encyclopædia Britannica, "Archimedes Screw," in *Encyclopædia Britannica*, 2016.
[Online].
Available: <https://www.britannica.com/technology/Archimedes-screw>. Sep. 18, 2016.
- [23] Rehart Power, "Hydropower Screws," in *Rehart Power*. [Online]. Available:
<http://www.rehart-power.com/en/hydropower-screws/mode-of-operation.html>. Accessed:
Sep. 17, 2016.
- [24] Minesto, "Deep Green" in *Minesto*, 2016. [Online]. Available:
<http://minesto.com/deep-green/>. Accessed: Sep. 17, 2016.
- [25] US Department of Energy Office of Energy Efficiency and Renewable Energy, "How
Hydropower Works," in *Energy.Gov*. [Online]. Available:
<http://energy.gov/eere/water/history-hydropower>. Accessed: Sep. 16, 2016.
- [26] R. H. Charlier and C. W. Finkl, *Ocean energy: Tide and Tidal Power*. Berlin:
Springer-Verlag Berlin and Heidelberg GmbH & Co. K, 2008.
- [27] Bay of Fundy Tourism Partnership, "World's Highest Tides," in *Bay of Fundy*, 2014.
[Online]. Available: <http://bayoffundytourism.com/worlds-highest-tides/>. Accessed: Sep.
17, 2016.

- [28] Vortex Hydro Energy, "Technology," in *Vortex Hydro Energy*, 2013. [Online]. Available: <http://www.vortexhydroenergy.com/>. Accessed: Sep. 17, 2016.
- [29] D. Pierce, "How VIVACE Works," in *Detroit Free Press*, 2013. [Online]. Available: <http://www.vortexhydroenergy.com/technology/>. Accessed: Sep. 17, 2016.
- [30] "Learning from Humpback Whales How to Create Efficient Wind Power," in *Biomimicry* 3.8, 2014. [Online]. Available: <http://biomimicry.net/about/biomimicry/case-examples/energy/>. Accessed: Sep. 15, 2016.
- [31] T. B. Institute, "Flippers provide lift, reduce drag: Humpback whale," in *The Biomimicry Institute*, AskNature, 2008. [Online]. Available: <http://www.asknature.org/strategy/3f2fb504a0cd000eae85d5dcc4915dd4>. Accessed: Sep. 15, 2016.
- [32] "Amazon black ghost knifefish teaches robots a thing or two about underwater locomotion," in *Tech Times*, Tech Times, 2014. [Online]. Available: <http://www.techtimes.com/articles/3512/20140219/amazon-black-ghost-knifefish-teaches-robots-a-thing-or-two-about-underwater-locomotion.htm>. Accessed: Sep. 16, 2016.
- [33] A. A. Shirgaonkar, O. M. Curet, N. A. Patankar, and M. A. MacIver, "The hydrodynamics of ribbon-fin propulsion during impulsive motion," *Journal of Experimental Biology*, vol. 211, no. 21, pp. 3490–3503, Nov. 2008. [Online]. Available: <http://jeb.biologists.org/content/211/21/3490>. Accessed: Sep. 16, 2016.

- [34] HDT, [Online] Available:
<http://www.hdtglobal.com/product/ghostbot/> Accessed: Sep. 18, 2016.
- [35] Youtube, [Online]. Available: <https://i.ytimg.com/vi/ehp39x1QaPg/hqdefault.jpg>.
Accessed: Sep. 18, 2016.
- [36] Ryan Ulbrich, [Online] Available:
<http://therearenoroads.com/wp-content/uploads/2013/10/strandbeest.jpg>. Accessed: Sep. 16,
2016.
- [38] I. Costanzo, A. Kelsey, F. Ogren, and D. Wians, "Design of a Novel Concept for
Harnessing Tidal Stream Power," Mar. 26, 2015. [Online]. Available:
[http://gordonlibrary.wpi.edu/vwebv/holdingsInfo?searchId=367&recCount=](http://gordonlibrary.wpi.edu/vwebv/holdingsInfo?searchId=367&recCount=10&recPointer=2&bibId=2864710)
[10&recPointer=2&bibId=2864710](http://gordonlibrary.wpi.edu/vwebv/holdingsInfo?searchId=367&recCount=10&recPointer=2&bibId=2864710). Accessed: Feb. 25, 2017.
- [39] S. Bailey, K. Bradley, A. Chan, N. Curtis, and L. Richard, "Design of a Novel Concept
for Harnessing Tidal Stream Power: A Continuation," Apr. 28, 2016. [Online]. Available:
[http://gordonlibrary.wpi.edu/vwebv/holdingsInfo?searchId=371&recCount=10&recPoint](http://gordonlibrary.wpi.edu/vwebv/holdingsInfo?searchId=371&recCount=10&recPointer=2&bibId=3059435)
[er=2&bibId=3059435](http://gordonlibrary.wpi.edu/vwebv/holdingsInfo?searchId=371&recCount=10&recPointer=2&bibId=3059435). Accessed: Feb. 25, 2017.
- [40] ME Mechanical Team, "Dynamometer: Introduction and Types," in ME Mechanical, ME
Mechanical, 2016. [Online]. Available:
<https://me-mechanicalengineering.com/dynamometer-introduction-types/>. Accessed: Feb.
26, 2017.
- [41] Civil Engineering Worldwide Community, "Structural and Stress Analysis," in *Civil*

Engineering Worldwide Community, Civil Engineering Worldwide Community. [Online].

Available:

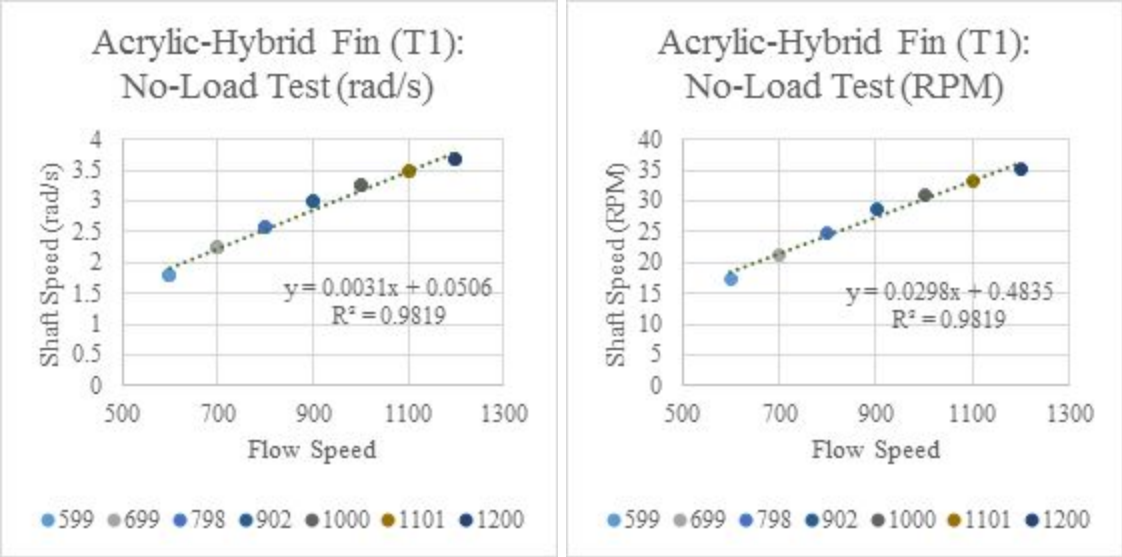
<https://cewcivil.wordpress.com/%E2%80%A2design/%E2%80%A2-structural-and-stress-analysis/>. Accessed: Feb. 28, 2017.

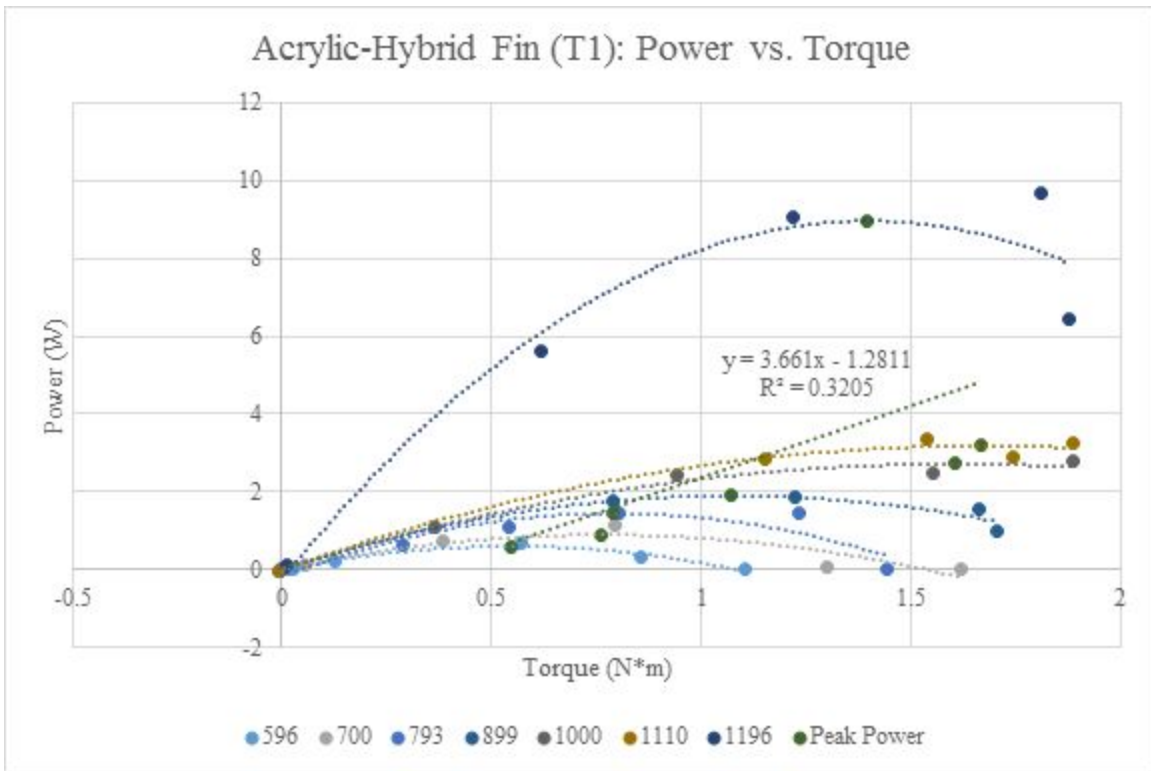
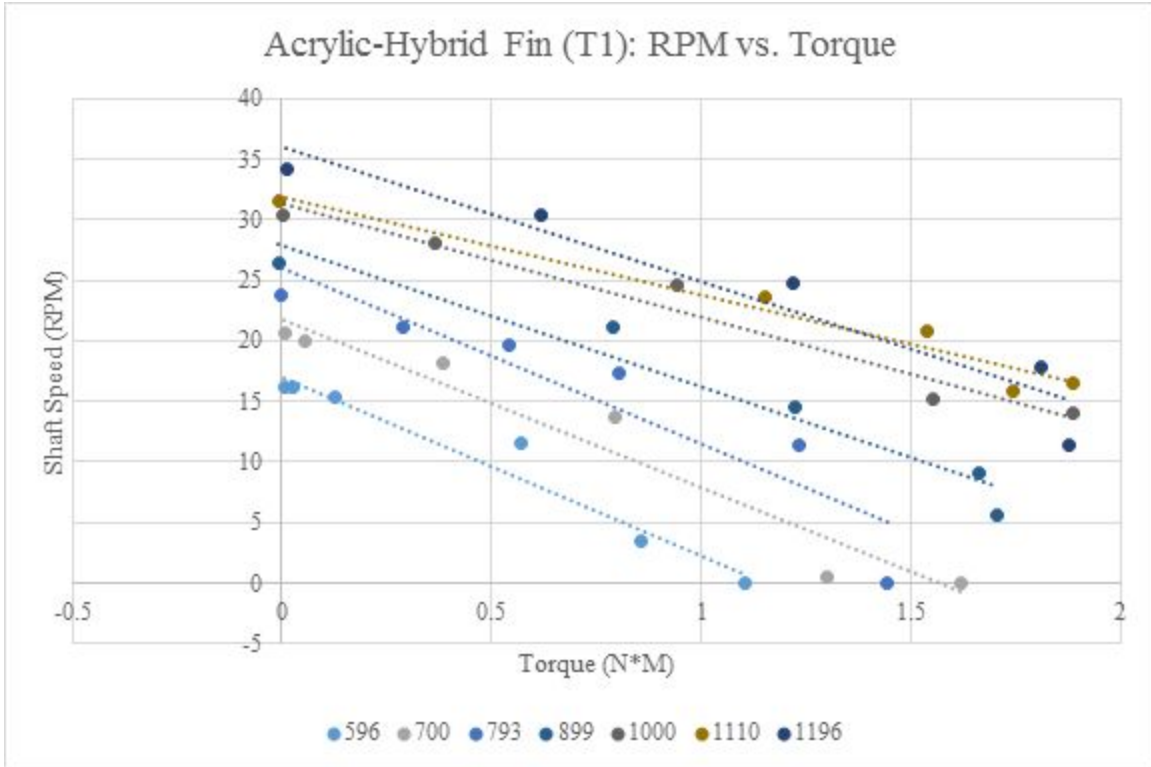
[42] "Stress and Deflections in Beams", *Engineeringtoolbox.com*, 2017. [Online]. Available:

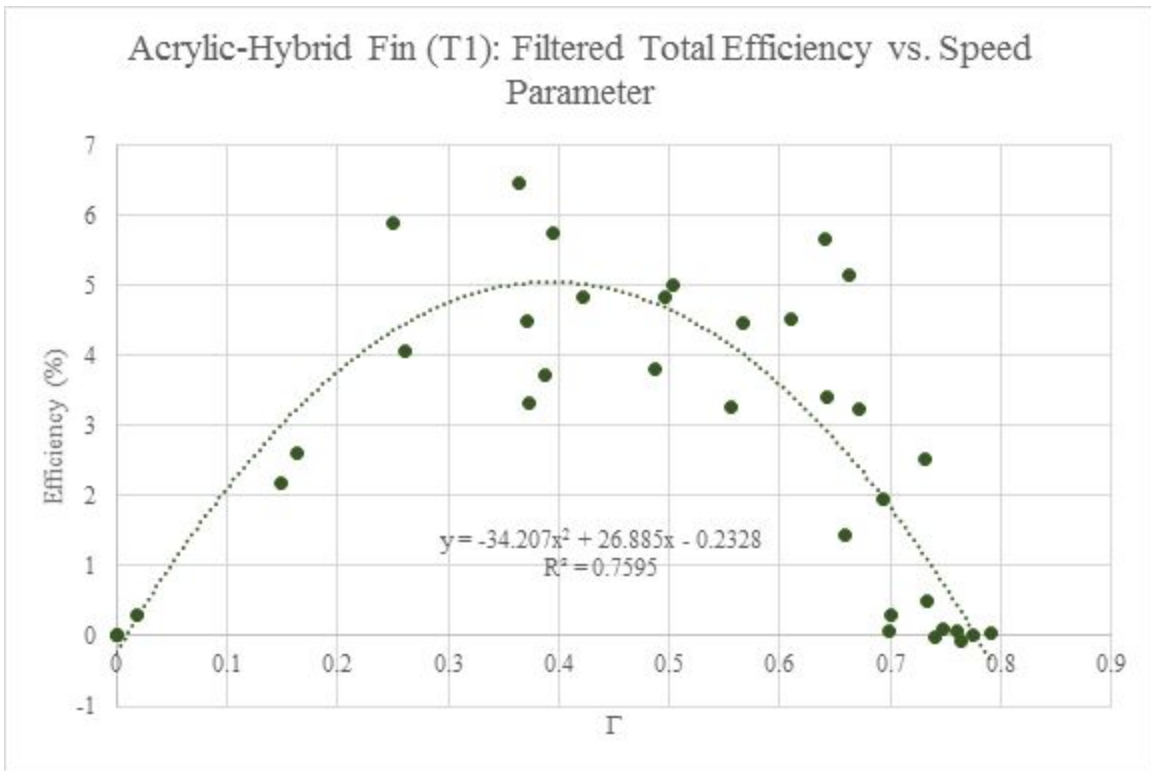
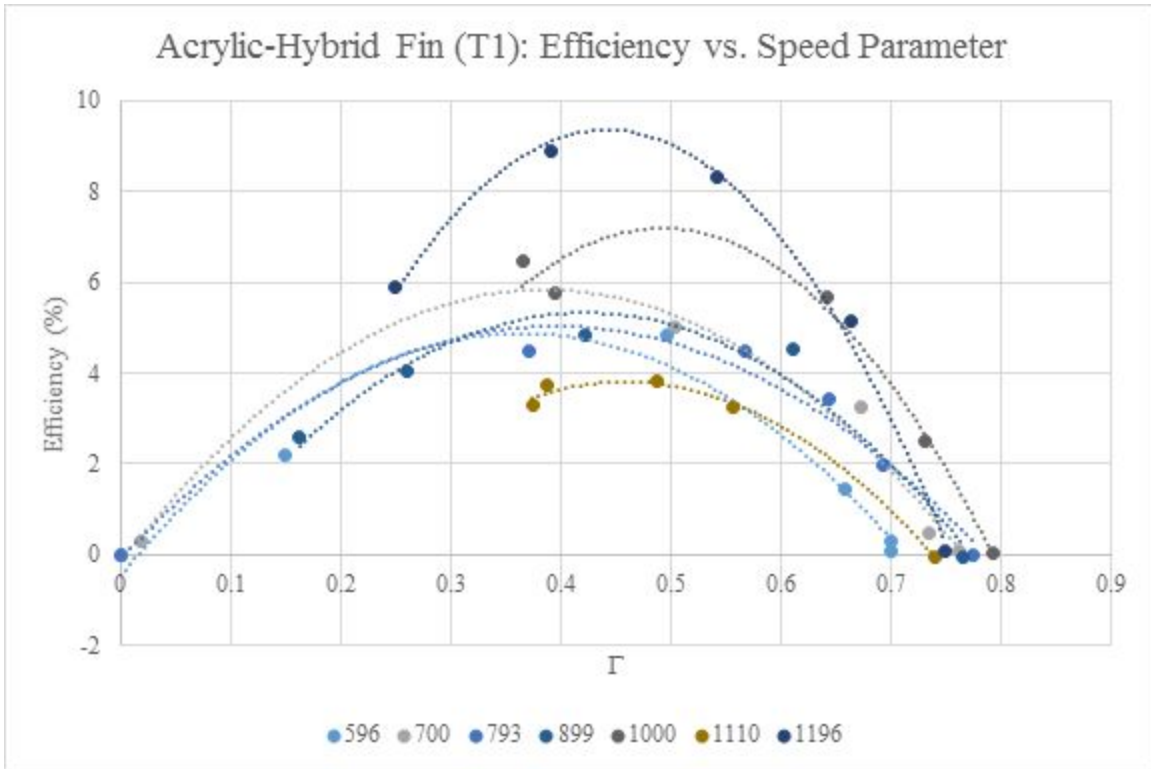
http://www.engineeringtoolbox.com/beam-stress-deflection-d_1312.html. Accessed: 12-Feb- 2017.

12. Appendix

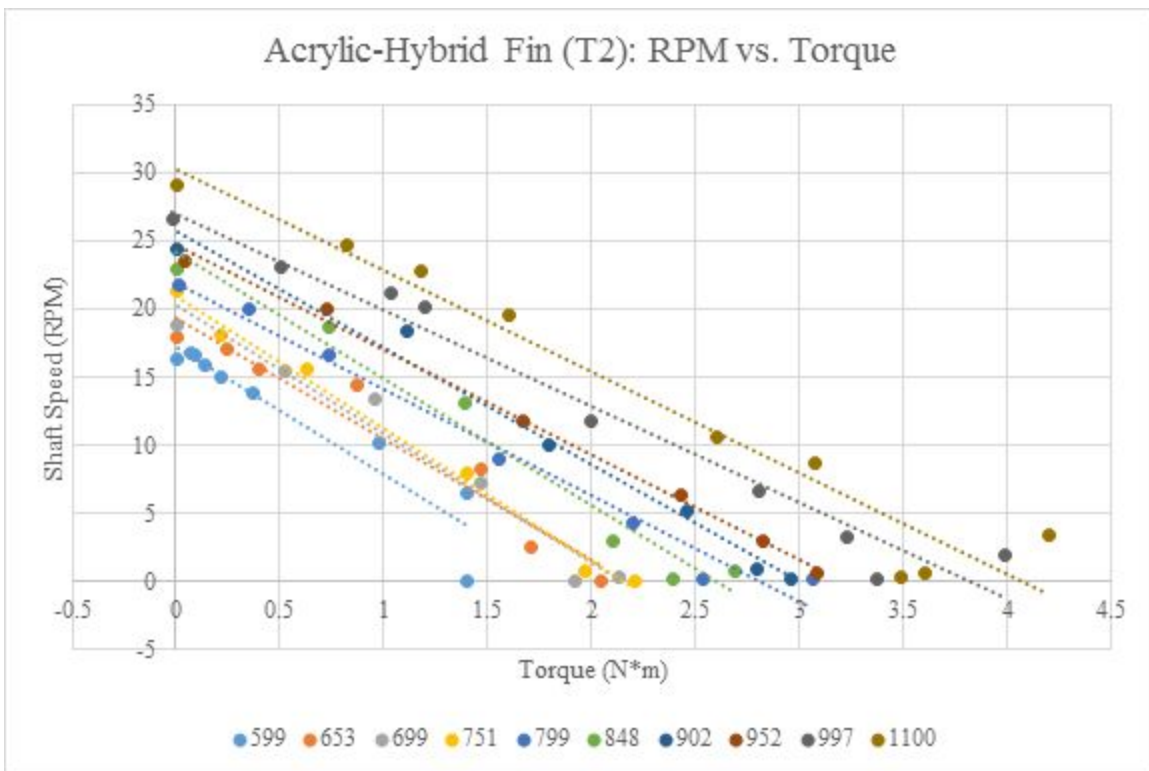
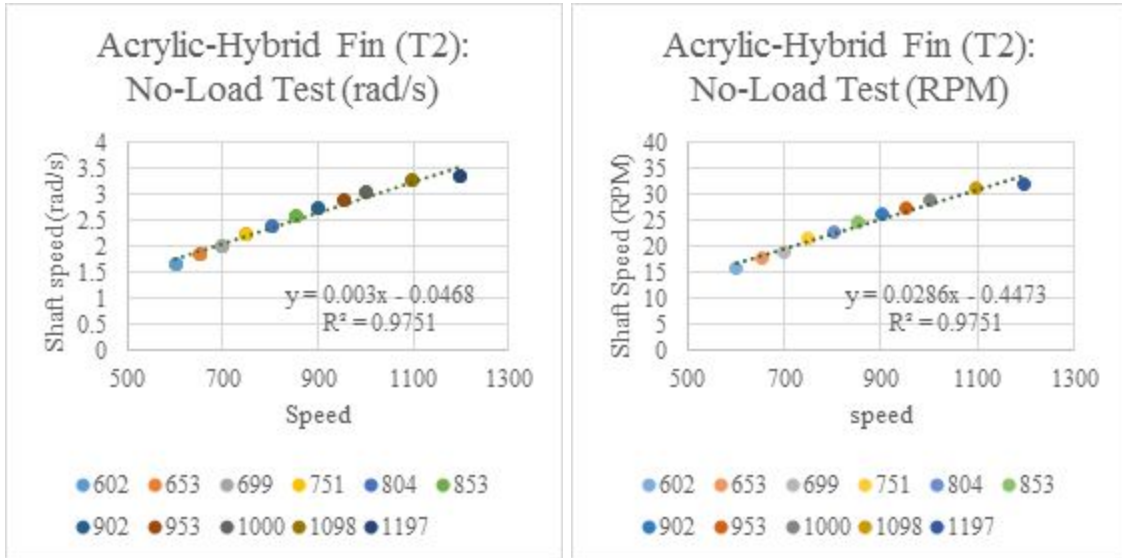
Appendix A: Acrylic-hybrid Fin (T1) Plots



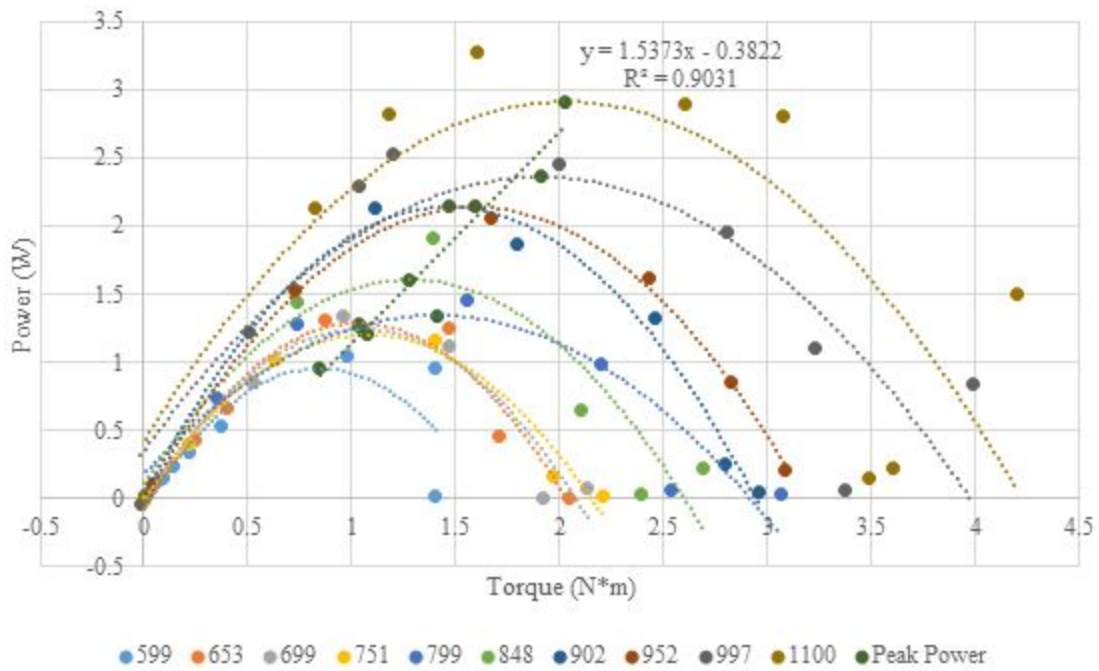




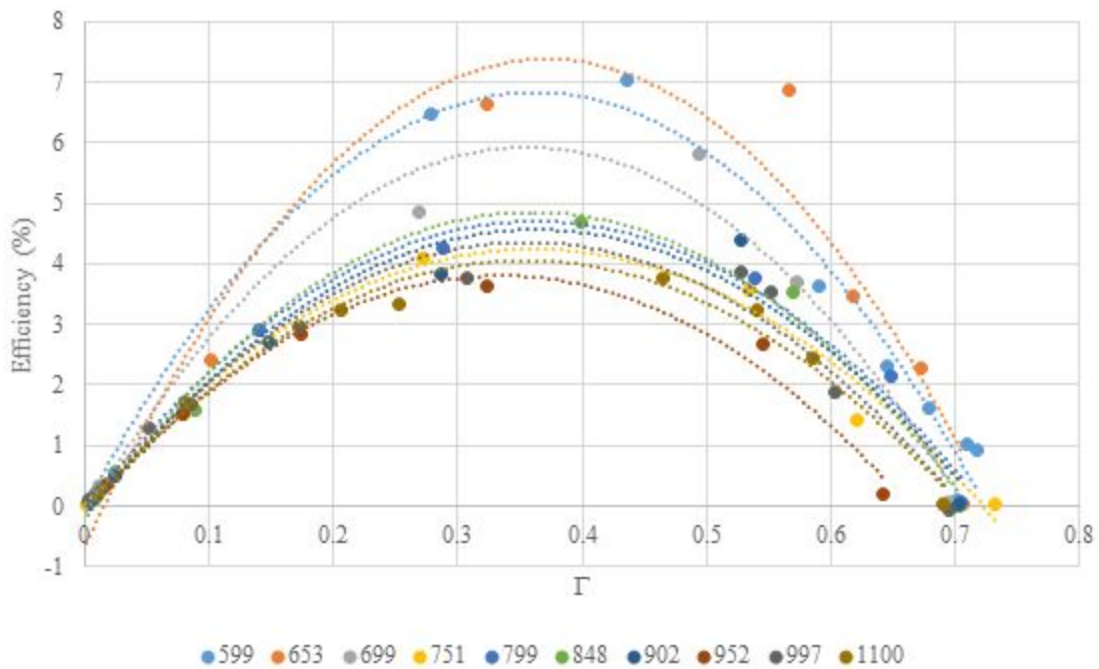
Appendix B: Acrylic-hybrid Fin (T2) Plots



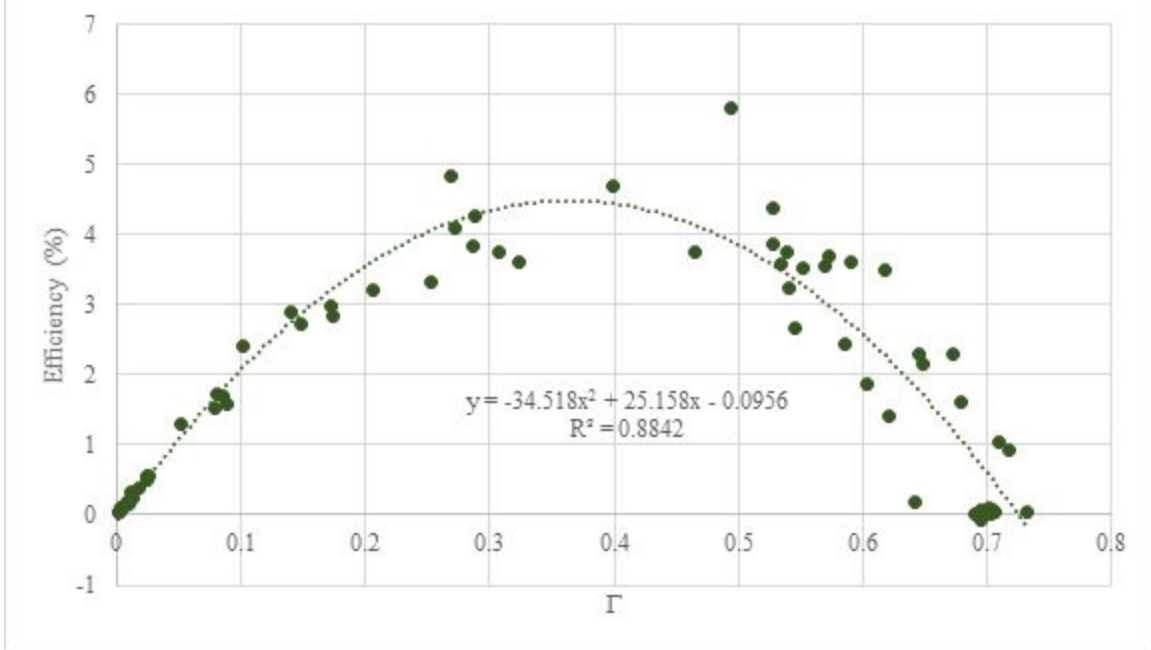
Acrylic-Hybrid Fin (T2): Power vs. Torque



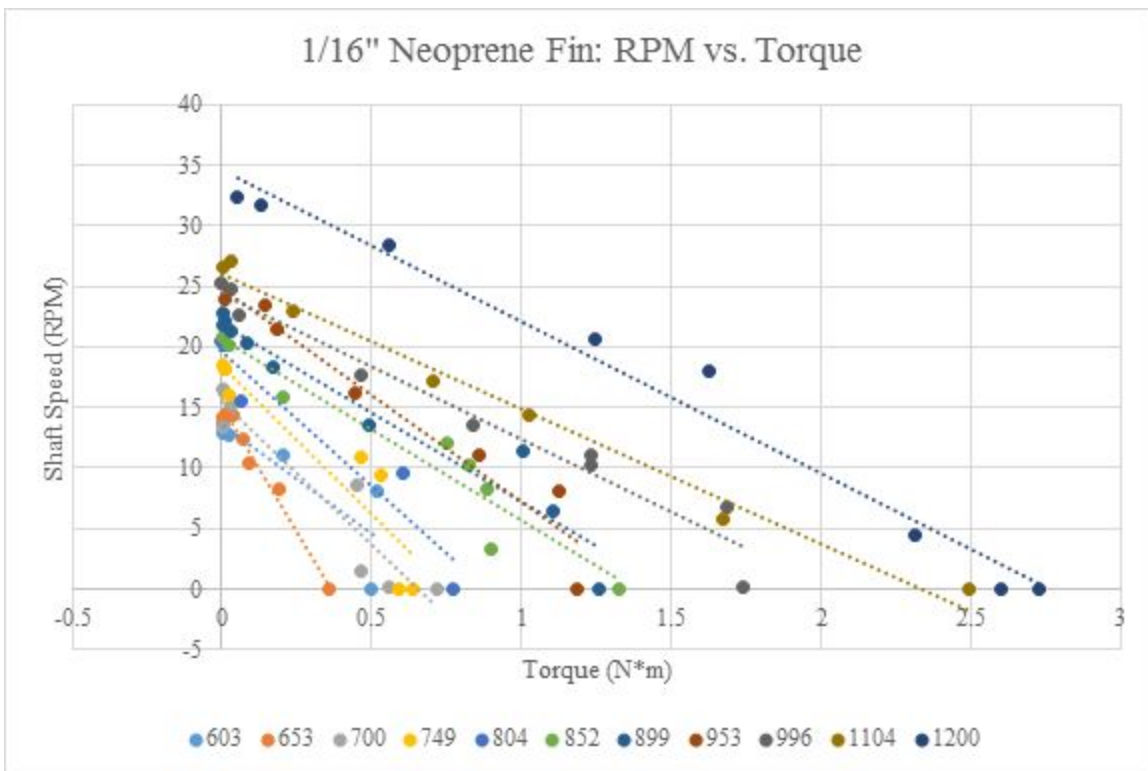
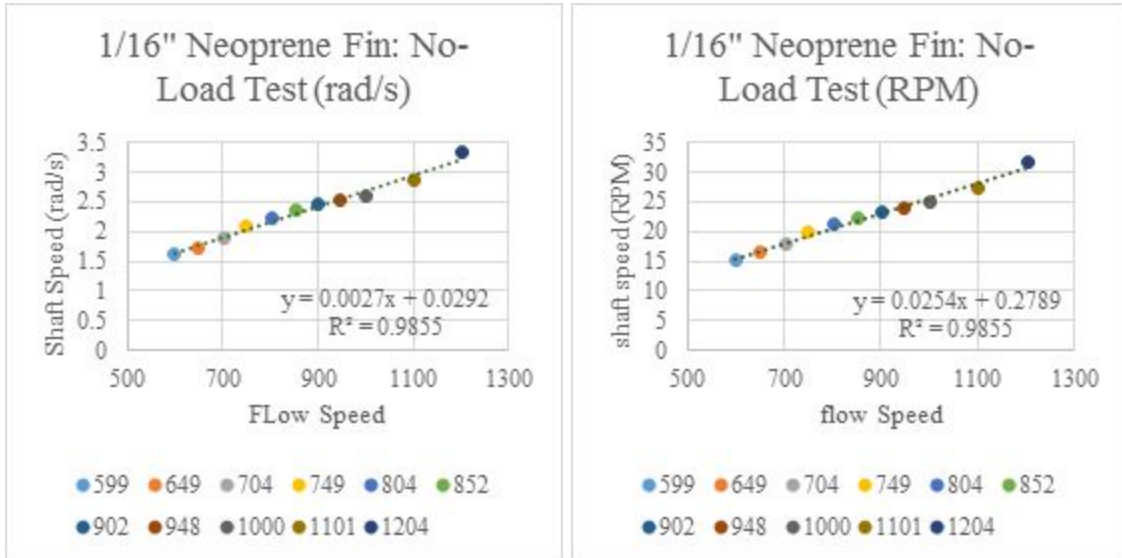
Acrylic-Hybrid Fin (T2): Efficiency vs. Speed Parameter



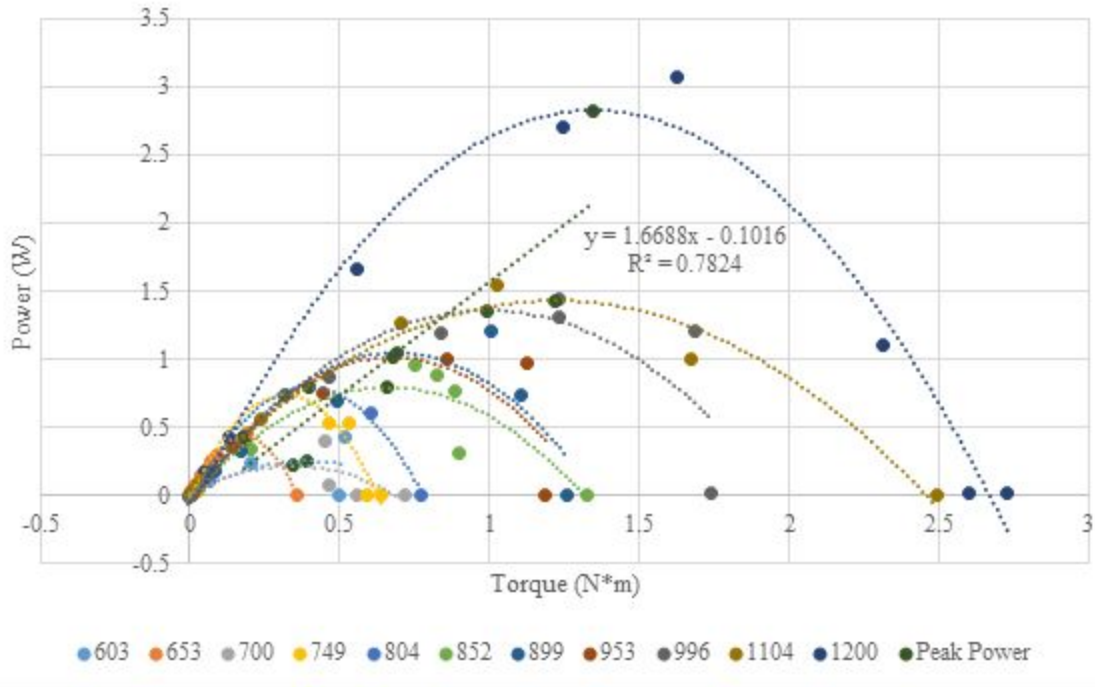
Acrylic-Hybrid Fin (T2): Filtered Total Efficiency vs. Speed Parameter



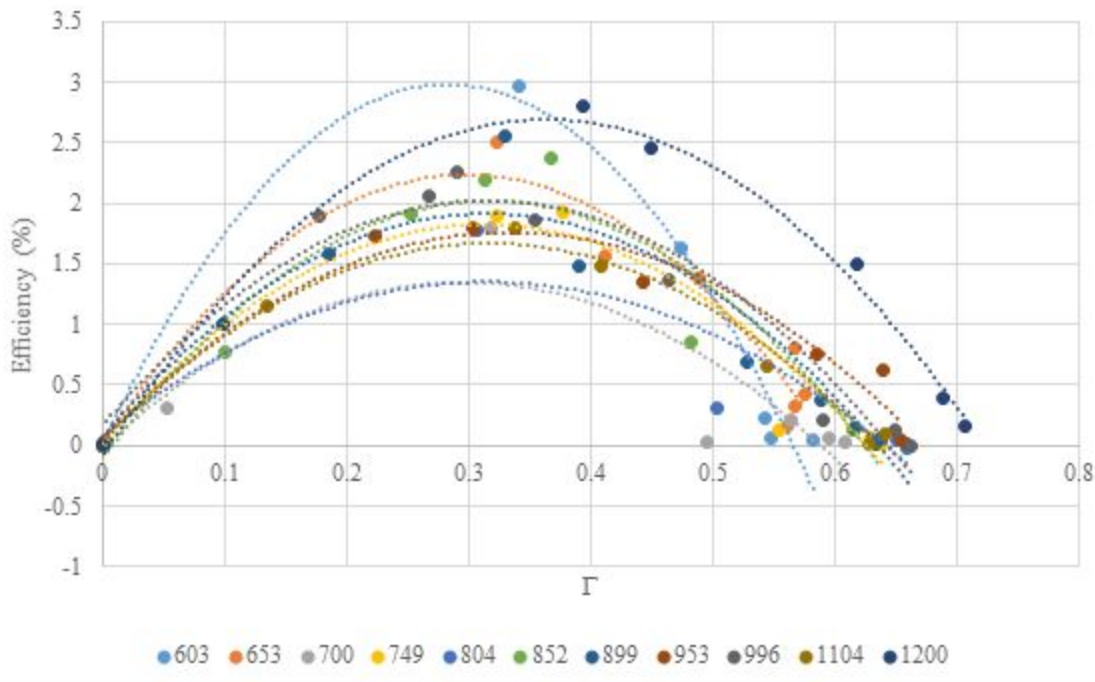
Appendix C: 1/16" Neoprene Fin Plots



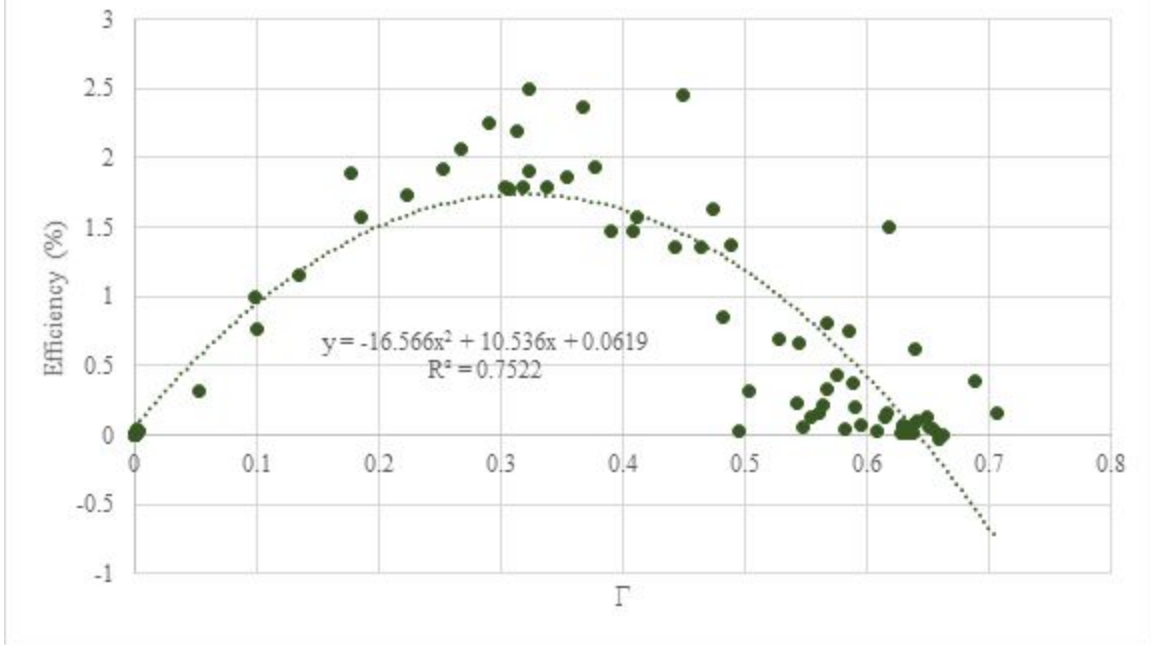
1/16" Neoprene Fin: Power vs. Torque



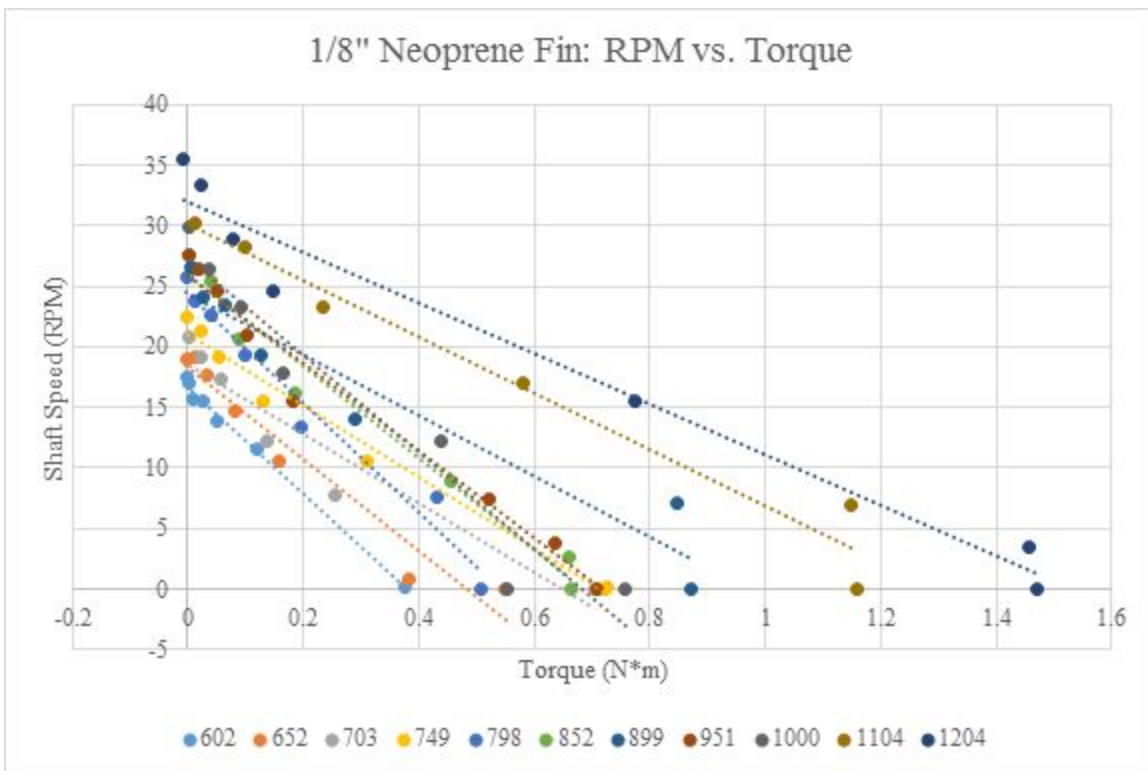
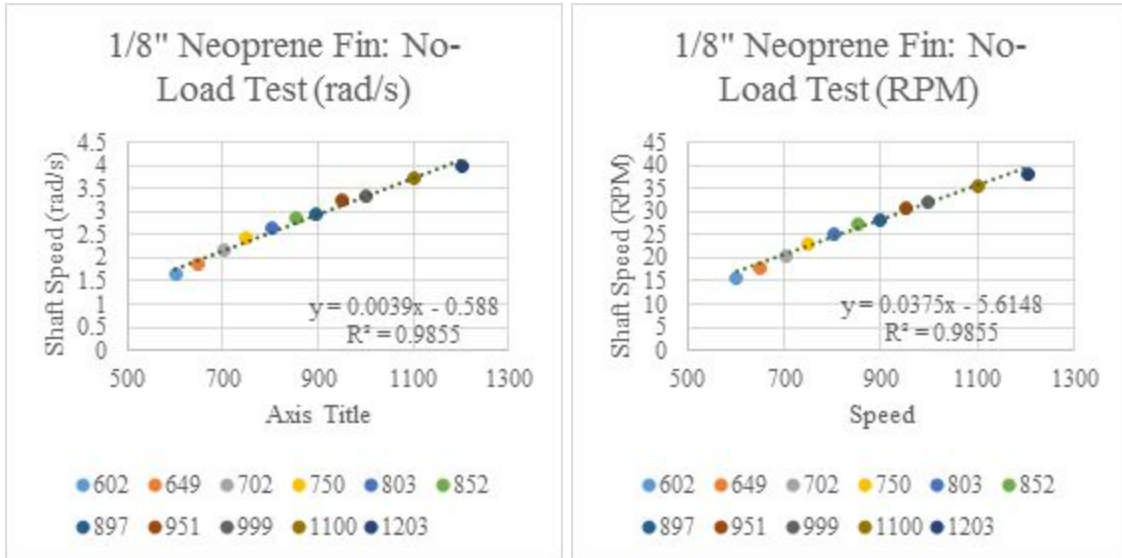
1/16" Neoprene Fin: Efficiency vs. Speed Parameter

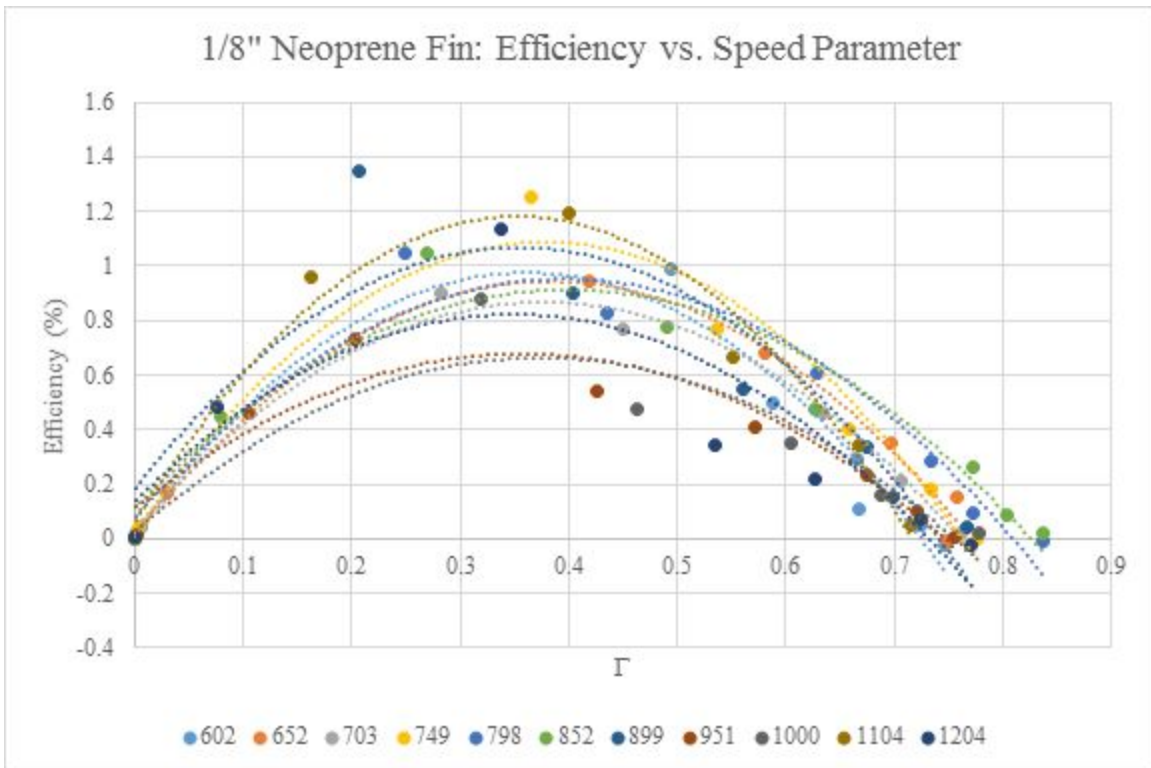
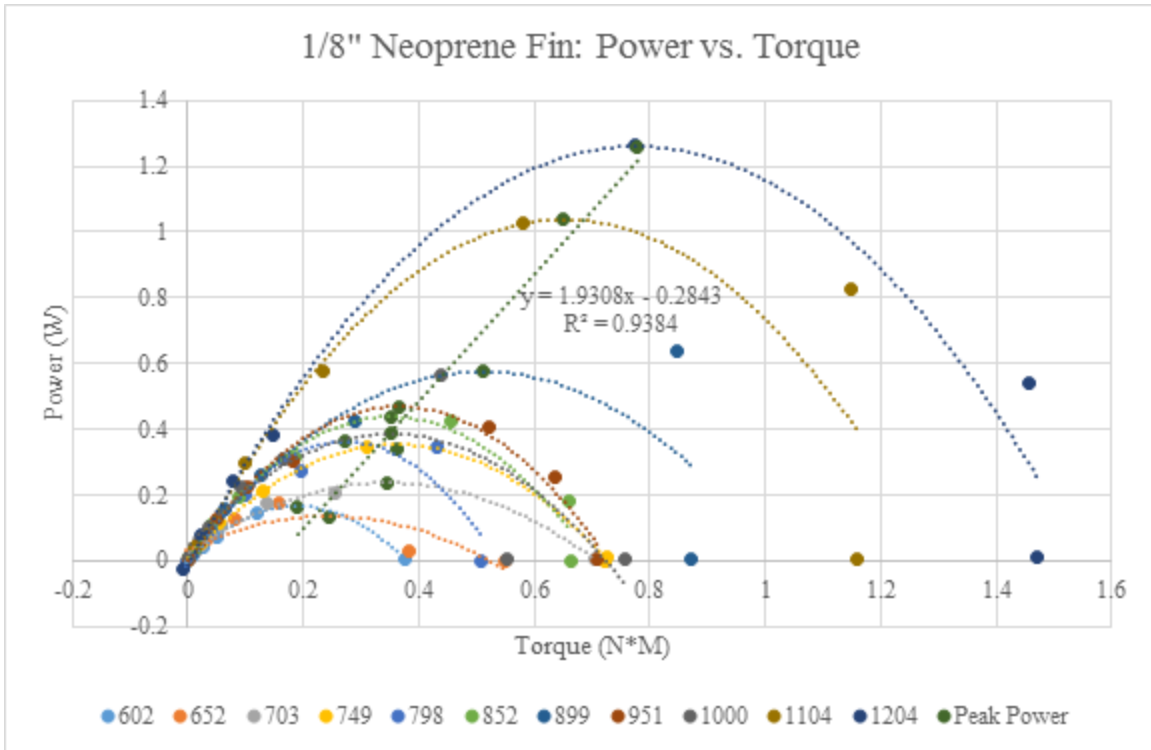


1/16" Neoprene Fin: Filtered Total Efficiency vs. Speed Parameter

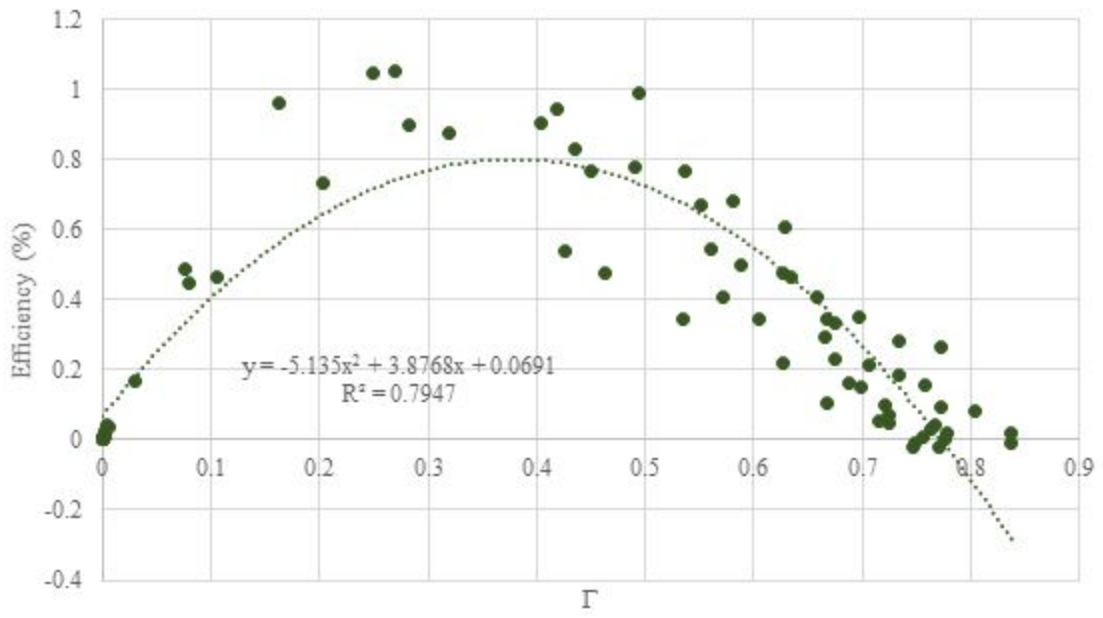


Appendix D: 1/8" Neoprene Fin Plots

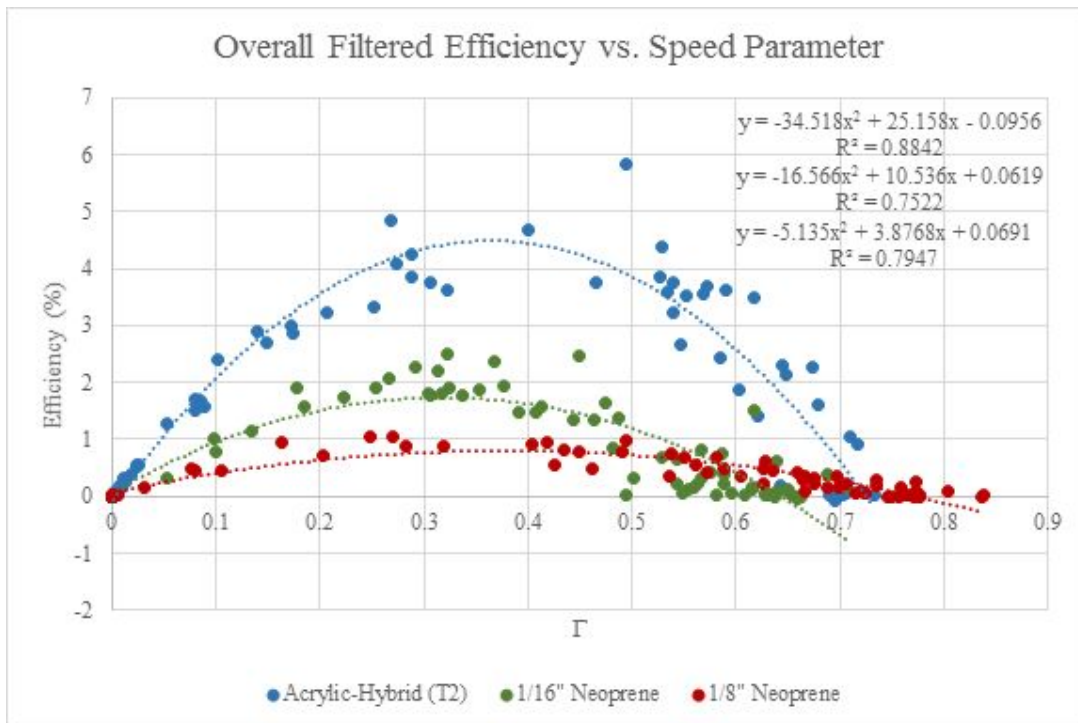
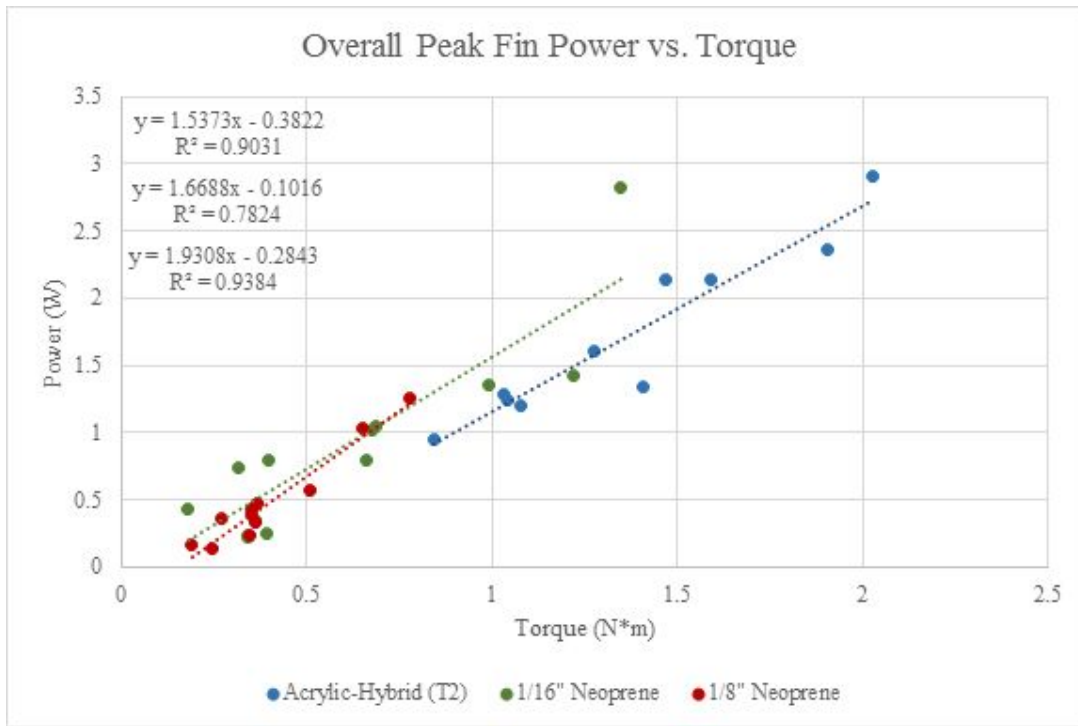




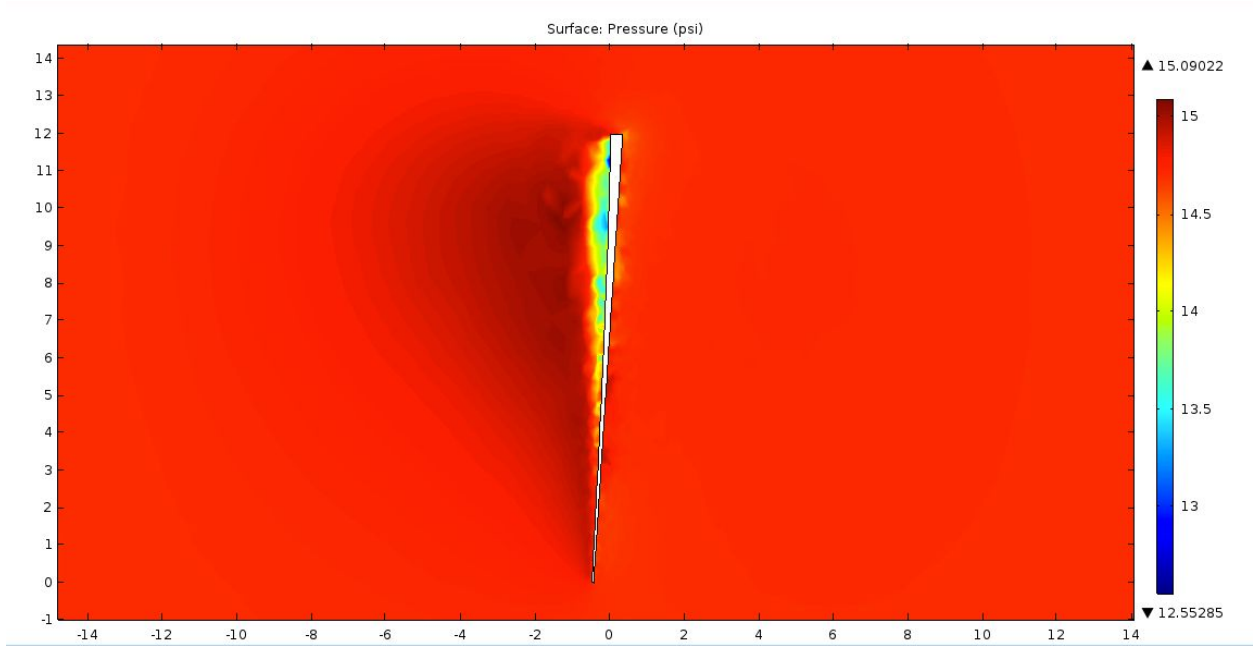
1/8" Neoprene Fin: Filtered Total Efficiency vs. Speed Parameter



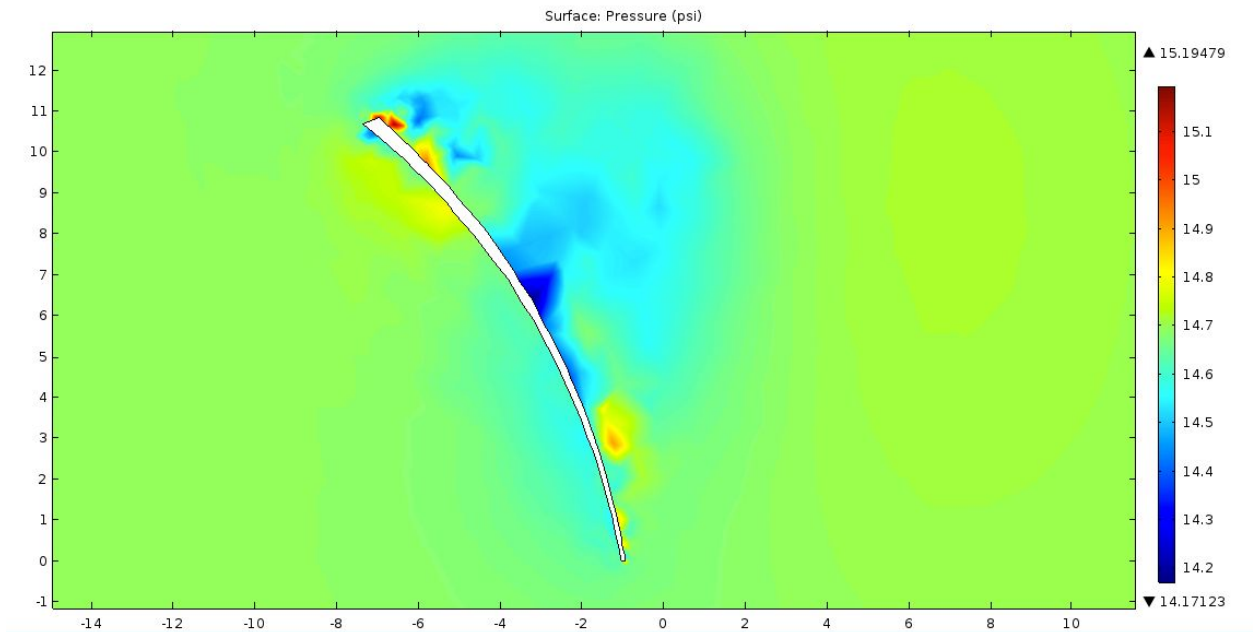
Appendix E: Overall Plots



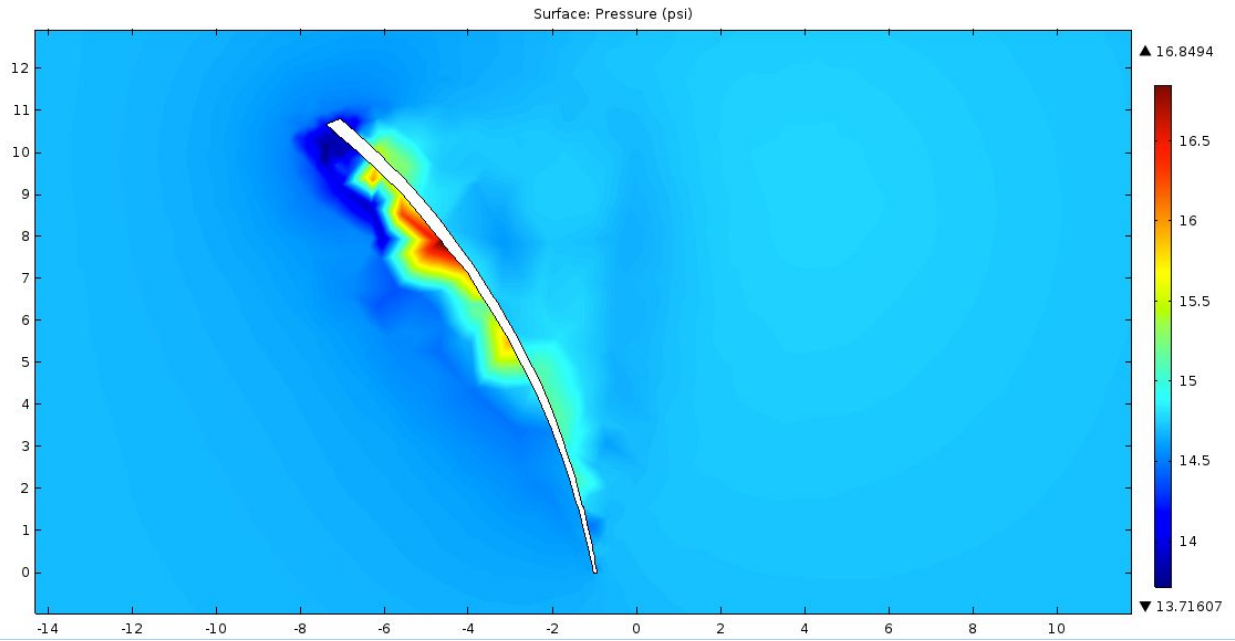
Appendix F: COMSOL Cross Section Views for FEA



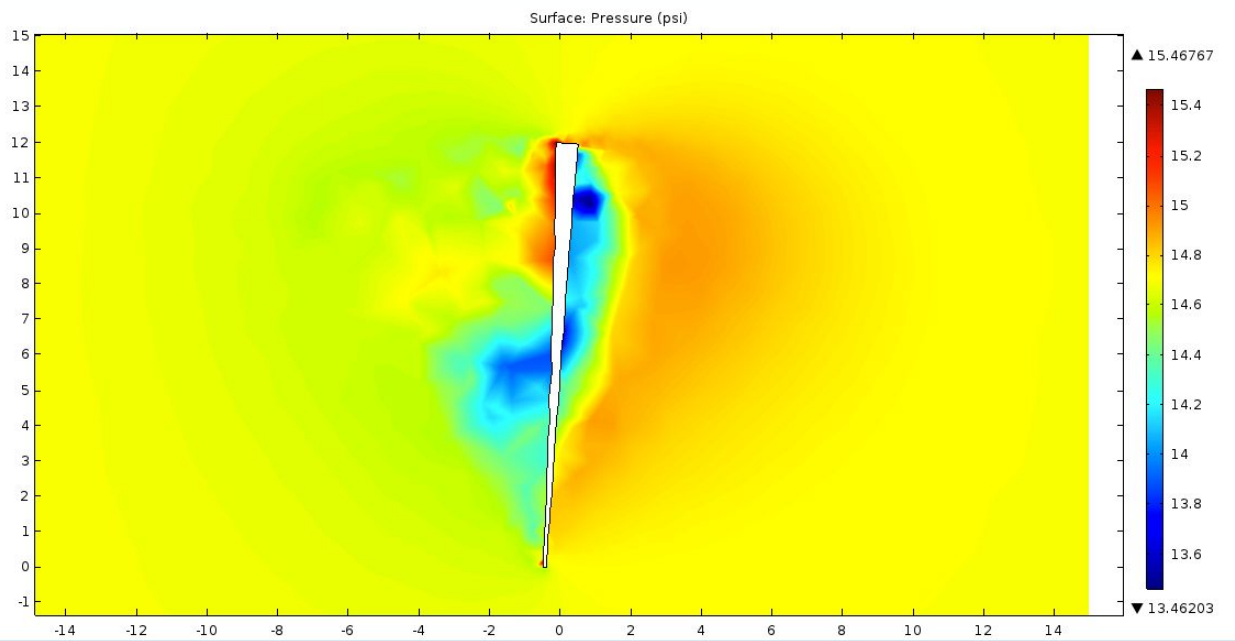
COMSOL View at 0



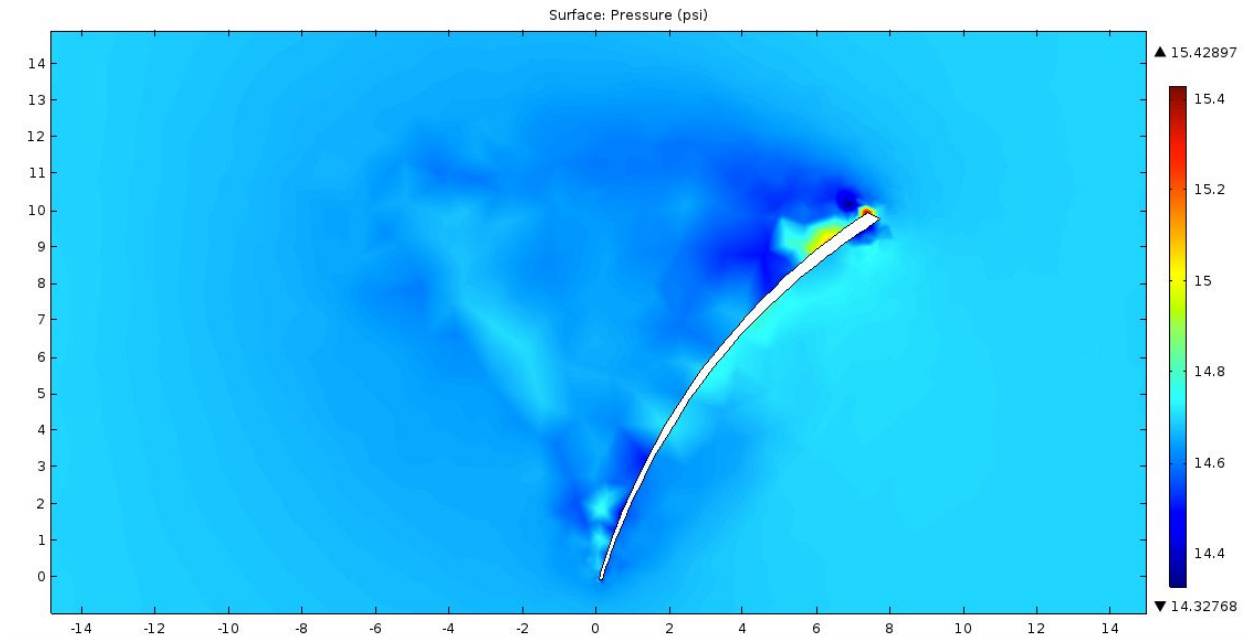
COMSOL View at 60



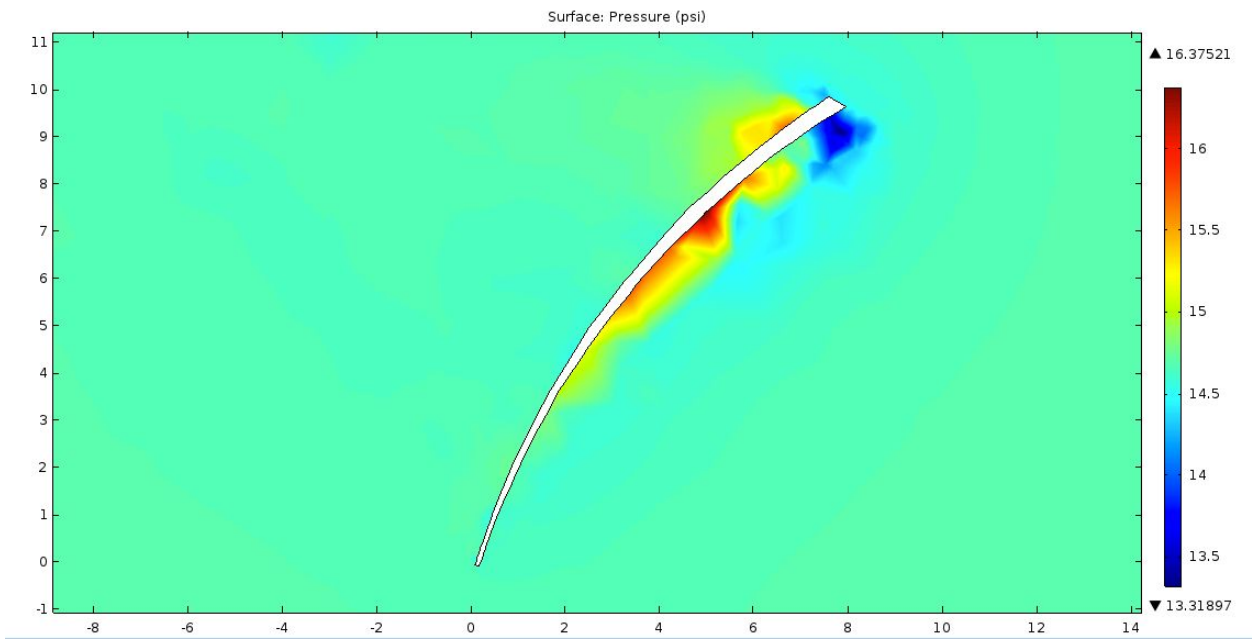
COMSOL View at 120



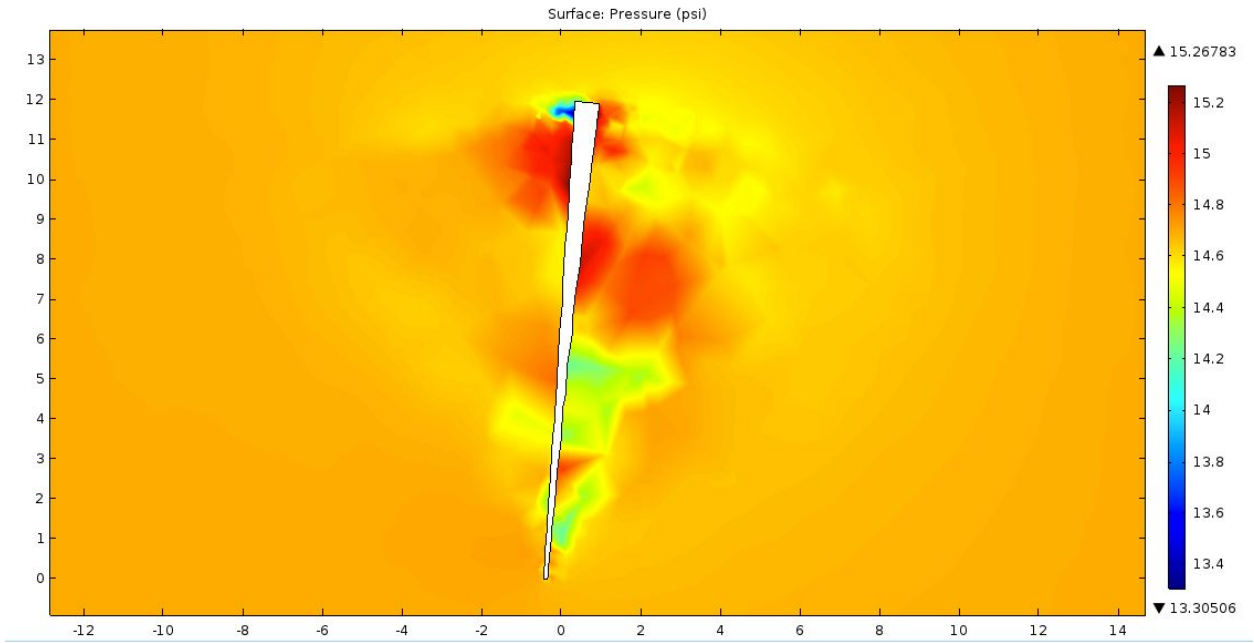
COMSOL View at 180



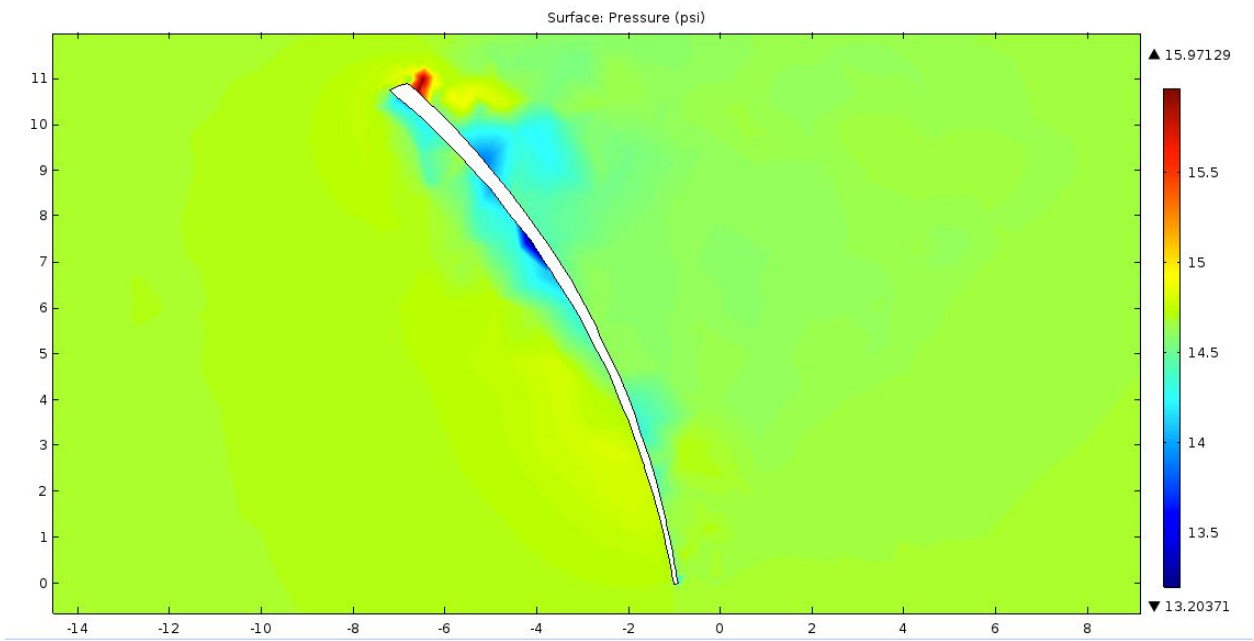
COMSOL View at 240



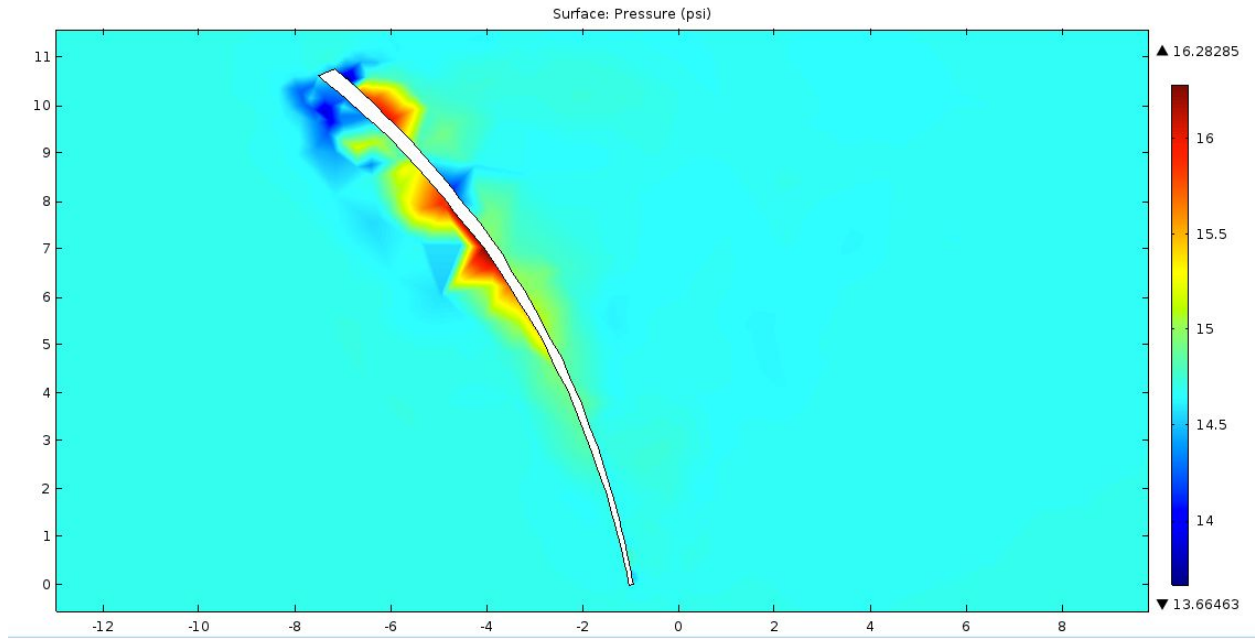
COMSOL View at 300



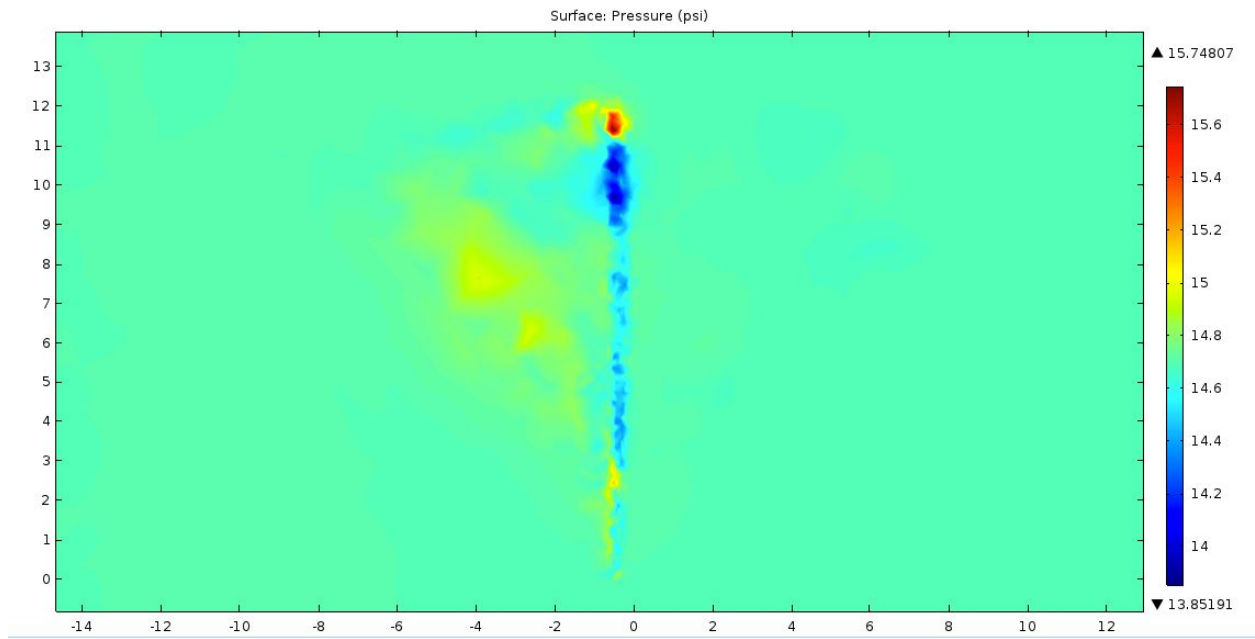
COMSOL View at 360



COMSOL View at 420

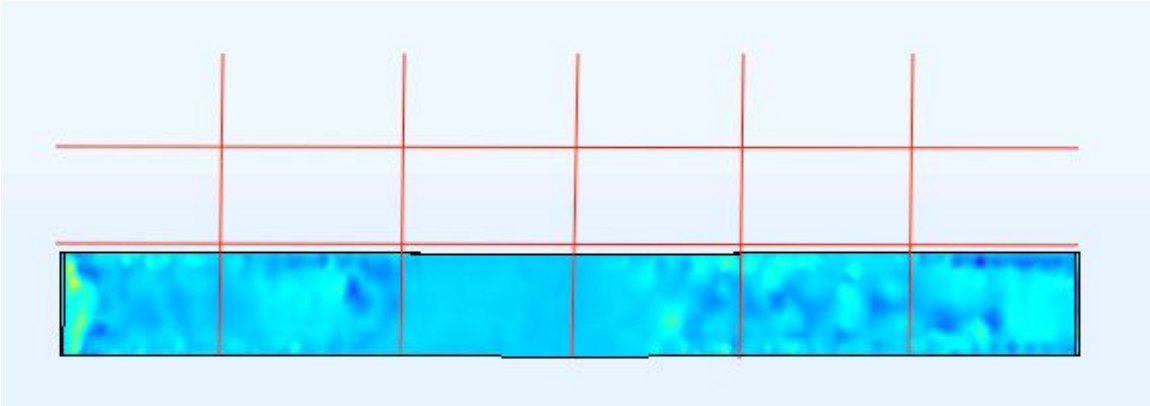


COMSOL View at 480

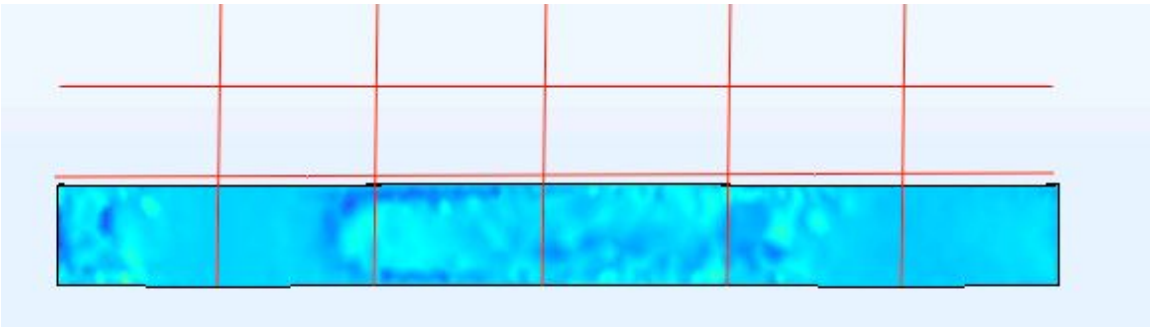


COMSOL View at 540

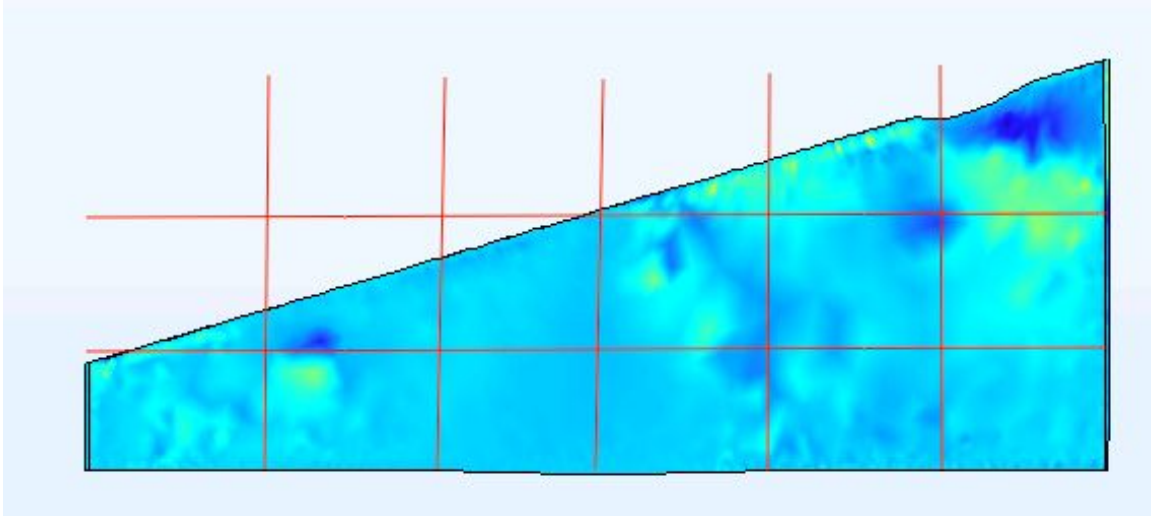
Appendix G: COMSOL Analysis of Test Fins



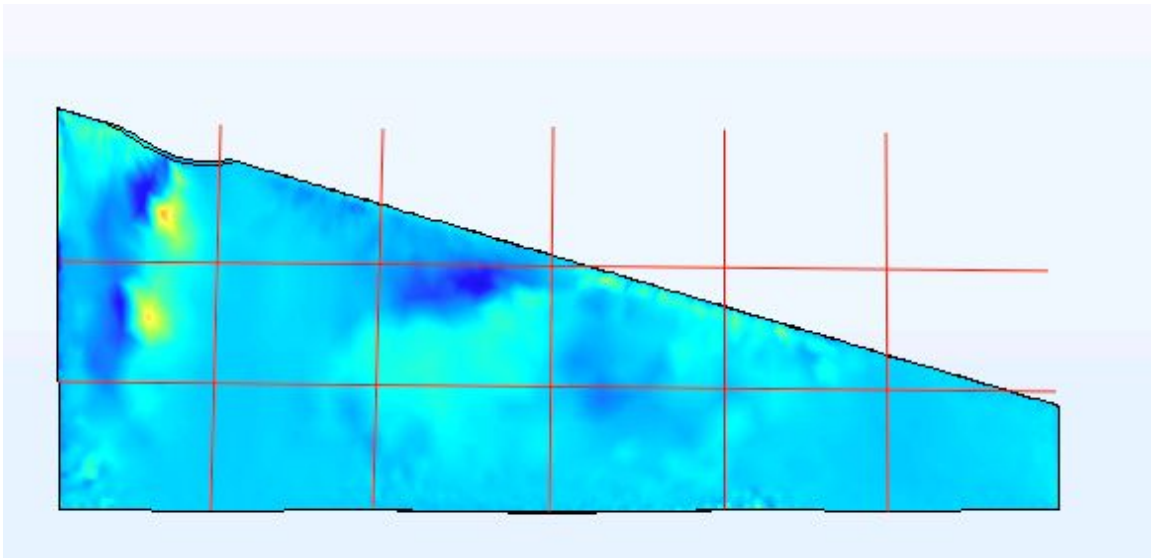
Left side of Test Fin 1



Right side of Test Fin 1



Left side of Test Fin 3



Right side of Test Fin 3